NTNU
Norwegian University of
Science and Technology

Modelling of window glasses exposed to blast loading

Ola Sesseng Bratsberg
Mathias Richter Kolsaker

Civil and Environmental Engineering
Submission date: June 2017
Supervisor: Tore Børvik, KT
Co-supervisor: Karoline Osnes, IBM
Odd Sture Hopperstad, IBM

Norwegian University of Science and Technology
Department of Structural Engineering

Department of Structural Engineering
Faculty of Engineering Science and Technology
NTNU- Norwegian University of Science and Technology

ACCESSIBILITY

OPEN

MASTER THESIS 2017

SUBJECT AREA:	DATE:	NO. OF PAGES:
Computational mechanics	June 10th, 2017	10 + 129 + 25

TITLE:

Modelling of window glasses exposed to blast loading

Modellering av sikkerhetsglass utsatt for eksplosjonslast

BY:

Ola Sesseng Bratsberg
Mathias Richter Kolsaker

SUMMARY:
Glass are one of the main causes of casualties and injuries during terror attacks with explosives, due to high-velocity fragments shooting through the air. A common way to increase the blast security in windows is to add a laminate or an interlayer between two or more glass panes creating laminated glass. One of the goals of the interlayer is to prevent the fragmentation through adhesive properties in the laminate glass connection. In the construction of the new governmental complex in Oslo, Norway, laminated glass windows are to be used as a measure to increase blast security.

The numerical modelling of laminated glass has proven to be challenging. This thesis aims to better understand the composite laminated glass and the response during quasistatic and blast loading. A study of the possibilities and limitations of numerical modelling of laminated glass in quasi-static and blast loading simulations was also conducted in the thesis. Point tracking DIC analysis was used to capture the response in the specimens subjected to blast load

Experiments were conducted in the SIMLab research facilities at NTNU. Four-point bending tests were carried out on laminated glass specimens to study the fracture strength during quasi-static loading, and blast tests were conducted on both regular float glass and laminated glass in the SIMLab shock tube to study the response during blast loading. The data recorded during the experiments were interpreted, and the results were used in the development of numerical models of the experiments. The tests were modelled with an explicit non-linear FEM code in IMPETUS Afea Solver, with node splitting used to describe fracture. Parameter studies were conducted to examine the effect of e.g. mesh size, element type and properties of interaction between PVB and glass.

From the quasi-static bending tests, it was found that the fracture stresses in the glass varied due to stochastic material properties in float glass. It was found a higher fracture strength in larger samples than the small samples. In the blast tests, the fragment size was smaller in the laminated glass than in the float glass. In the numerical modelling of the glass panes, it was found that node splitting and pentahedron elements gave good results describing crack propagation. Material modelling of the PVB in IMPETUS and interaction between glass and PVB proved challenging and needs further research.

RESPONSIBLE TEACHER: Professor Tore Børvik

SUPERVISOR(S): PhDc Karoline Osnes, Professor Odd-Sture Hopperstad, Professor Tore Børvik

CARRIED OUT AT: Deparment of Structural Engineering, NTNU

Institutt for konstruksjonsteknikk
Fakultet for ingeniørvitenskap og teknologi
NTNU- Norges teknisk- naturvitenskapelige universitet

TILGJENGELIGHET

ÅPEN

MASTEROPPGAVE 2017

FAGOMRÅDE:	DATO:	ANTALL SIDER:
Beregningsmekanikk	10.juni 2017	10 + 129 + 25

TITTEL:

Modellering av sikkerhetsglass utsatt for eksplosjonslast

Modelling of window glasses exposed to blast loading

UTFØRT AV:

Ola Sesseng Bratsberg
Mathias Richter Kolsaker

SAMMENDRAG:
Glassfragmenter i høy hastighet som følge av knuste glassruter er en av hovedårsakene til dødsfall og skader under terrorangrep gjennomført med eksplosiver. En vanlig måte å øke sikkerheten til vinduene mot trykkbølger er å legge inn et laminat mellom to eller flere glassruter. En av hovedformålene med et slikt laminat er å forhindre glasset i å fragmentere ved hjelp av heft mellom glassflatene og laminatet. I utviklingen og byggingen av det nye regjeringskvartalet i Oslo er det tenkt brukt laminerte vinduer for å øke sikkerheten mot eksplosjoner.

Numerisk modellering av laminert glass har vist seg å være utfordrende. Denne oppgaven sikter seg inn mot en bedre forståelse av komposittmaterialet laminert glass og hvordan det oppfører seg under påføring av kvasi-statiske laster og påført trykklast. DIC-analyse ble brukt til å studere oppførselen i testobjektene under testingen. Oppgaven tar også for seg numerisk modellering av laminert glass påført av nevnte laster og søker å avdekke muligheter og begrensninger i numeriske verktøy.

Eksperimenter ble gjennomført i SIMLabs lokaler på NTNU. Fire-punkts bøyetester ble gjennomført på eksemplarer av laminert glass i ulike dimensjoner for å undersøke bruddkriteriet i komponentene. Forsøk ble gjennomført i SIMLabs shock tube på prøver av vanlig glass og på prøver av laminert glass for å studere responsen under sprenglast. Dataene samlet inn under forsøkene ble analysert og brukt i utarbeidelsen av numeriske modeller av forsøkene. Forsøkene ble modellert i den eksplisitte FEM koden IMPETUS Afea Solver, med node splitting som teknikk for å beskrive brudd. Parameterstudier ble gjennomført for å undersøke effekten av f.eks. mesh størrelse, elementtype og samvirke mellom PVB og glass.

Grunnet stokastiske materialegenskaper i glasset ble det funnet at bruddspenningen og maks last varierte i fire-punkts bøyetestene. De store prøvestykkene tålte mer enn de små. I sprenglasttesene ble fragmentstørrelsen funnet større for de vanlige glassene enn de laminerte glassene. Den numeriske modelleringen av glassrutene viste at node splitting og pentahedronelementer gir gode resultater ved sammenligning av sprekkpropagering. Materialmodellering av PVB i IMPETUS og samvirke viste seg vanskelig og krever mer forskning.

FAGLÆRER: Professor Tore Børvik

VEILEDER(E): PhD kandidat Karoline Osnes, Professor Odd-Sture Hopperstad, Professor Tore Børvik

UTFØRT VED: Institutt for kontruksjonsteknikk, NTNU

Department of Structural Engineering
FACULTY OF ENGINEERING SCIENCE AND TECHNOLOGY
NTNU – Norwegian University of Science and Technology

MASTER'S THESIS 2017

for

Ola Sesseng Bratsberg and Mathias Kolsaker

Modelling of window glasses exposed to blast loading

1. INTRODUCTION

Annealed floating glass is often used in standard window glasses, but is a brittle material that offers little resistance to the intense blast waves produced by explosions. When a window fails, it breaks into a number of sharp fragments that can travel at high velocities. Laminated glass has been found to mitigate the risk of free-flying glass fragments by retaining them on a polymer interlayer upon fracture. It is, however, important to fully understand the conditions for and the types of failure mechanisms in both annealed glass and laminated glass to be able to optimise the design of facades against blast loading. Due to existing microscopic flaws in the glass surface, the strength will have a large scatter. It is therefore important to consider this when including a failure model for the glass. The modelling of blast-exposed structural components, including glass, has received considerable attention in recent years. In regards to the new government building complex in Oslo, safely glasses and facades are of major concern in the case of a possible new blast event, and the research on the behaviour of glass is therefore of great interest.

2. OBJECTIVES

The main objective of this research project is to determine how annealed and laminated glass will behave under blast and quasi-static loading. Numerical models will be made to examine the response of annealed and laminated glass exposed to blast and quasi-static loading. Blast experiments from the literature or own experiments will be used to validate the numerical models and to examine to which extent they can predict the response of the glasses.

3. A SHORT DESCRIPTION OF THE RESEARCH PROJECT

The main topics in the research project will be as follows;

1. A comprehensive literature review should be conducted to understand the blast load phenomenon, blast load design and shock tube test facilities. In addition, failure modeling of glass and the polymer materials exposed to extreme loadings must be reviewed in some detail.
2. The SIMLab Shock Tube Facility will be used to expose some glasses to blast loading, as an alternative to explosive detonations. The shock tube experiments will, together with data from the literature and SIMLab, be used to investigate typical dynamic responses and failure modes of the glasses exposed to blast loading.
3. Digital Image Correlation (DIC) will be used to measure the 3D transverse displacement fields of the glass panes in the shock tube experiments. DIC can also be used to study the fracture patterns in the glasses.
4. Non-linear FE numerical simulations of the experiments using IMPETUS Afea solver will be performed, and the numerical results shall be compared and discussed based on the experimental findings.

Supervisors: Tore Børvik (NTNU), Karoline Osnes (NTNU) and Odd Sture Hopperstad (NTNU).

The thesis must be written according to current requirements and submitted to the Department of Structural Engineering, NTNU, no later than June 11th, 2017.

NTNU, January 15th, 2017.

Tore Børvik
Professor

Abstract

Flying glass fragments are one of the main causes of casualties and injuries during terror attacks with explosives, due to fragments shooting through the air. A common way to increase the blast security in windows is to add a laminate or an interlayer between two or more glass panes creating laminated glass. One of the goals of the interlayer is to prevent fragments from loosening, through adhesive properties in the laminate glass connection. In the construction of the new governmental complex in Oslo, Norway, laminated glass windows are to be used as a measure to increase blast security. [1]

The numerical modelling of laminated glass has proven to be challenging. This thesis aims to increase the understanding of laminated glass properties and the response during quasi-static and blast loading. A study of the possibilities and limitations of numerical modelling of laminated glass in quasi-static and blast loading simulations was also conducted in the thesis. Point tracking DIC analysis was used to capture the response in the specimens subjected to blast load

Experiments were conducted in the SIMLab research facilities at NTNU. Four-point bending tests were carried out on laminated glass specimens to study the fracture strength during quasi-static loading, and blast tests were conducted on both regular float glass and laminated glass in the SIMLab shock tube to study the response during blast loading. The data recorded during the experiments were interpreted, and the results were used in the development of numerical models of the experiments. The tests were modelled with an explicit non-linear FEM code in IMPETUS Afea Solver, with node splitting used to describe fracture. Parameter studies were conducted to examine the effect of e.g. mesh size, element type and properties of interaction between PVB and glass.

From the quasi-static bending tests, it was found that the fracture stresses in the glass varied due to stochastic material properties in float glass. It was found a higher fracture strength in larger samples than the small samples. In the blast tests, the fragment size was smaller in the laminated glass than in the float glass. In the numerical modelling of the glass panes, it was found that node splitting and pentahedron elements gave good results describing crack propagation. Material modelling of the PVB in IMPETUS and interaction between glass and PVB proved challenging and needs further research.

Acknowledgements

This thesis was for the research group Structural Impact Laboratory (SIMLab) at the Department of Structural Engineering at the Norwegian University of Science and technology (NTNU) during the time period January 15th to June 10th 2017. The thesis was initiated by the Centre for Advanced Analysis (CASA).

We would like to express a special thanks to our supervisors for their guidance and support during the work on our thesis. The weekly meetings and ”open door” policy were invaluable. Thank you Professor Tore Børvik, PhDc Karoline Osnes and Professor Odd Sture Hopperstad.

Additionally we would like to thank Mr. Trond Auestad for his contributions and assistance during the experimental work in the shock tube and bending tests and Tore Kristensen at SINTEF for his assistance during bending tests.

Our sincere thanks go to Lars Olovsson for his truly invaluable help with modelling in IMPETUS. Thank you for the presentation given February 23 in Trondheim and thank you for taking your time to answer our emails. A special thanks to Postdoc Jens Krisitan Holmen for his help with IMPETUS modelling and his management of the IMPETUS server at NTNU.

Finally we would like to thank our fellow students at NTNU for an amazing time and a great learning environment.

Trondheim, 10th of June 2017

Ola Sesseng Bratsberg
Mathias Kolsaker

Ola Sesseng Bratsberg
Mathias Richter Kolsaker

Table of Contents

Nomenclature

Abbreviations

BB	Bergström Boyce
CPU	Central Processing Unit
DIC	Digital Image Correlation
DOF	Degree of Freedom
FEM	Finite Element Method
FG	Float glass
fps	Frames per second
GPU	Graphics Processing Unit
LEFM	Linear elastic fracture mechanics
LG	Laminated glass
NOE	Number of Elements
PVB	Polyvinyl butyral
SIMLab	Structural Impact Laboratory

Latin symbols

A	Cross sectional area
a	Half the crack length
B	Plate thickness
b	Half the crack width / Exponential decay coefficient
E	Young's modulus / Total energy
G	Energy release rate
I	Second moment of area
i_{r+}	Specific impulse of the positive phase
K_c	Critical stress intensity factor
M	Moment
m	Weibull modulus
P	Force / Pressure as a function of time
P_c	Cohesive force
P_a	Ambient pressure
P_r	Peak reflected pressure
P_{so}	Peak incident pressure
q	Applied load
t_+	Duration of positive phase
t_-	Duration of negative phase
t_a	Arrival time of shock wave
V	Volume
w	Deflection
w_f	Fracture energy
W_s	Work required to create a new surface
x_0	Equilibrium distance

Greek symbols

α	Weibull scale parameter / Angle of impact for a shock wave
β	Weibull shape parameter
δ_c	Critical mid-point deflection
ε	Strain
$\dot{\varepsilon}$	Strain rate
λ	Half the sin wave
κ	Curvature of beam subjected to bending
ν	Poisson Ratio
Π	Potential energy
ρ	Density / Radius of the curvature to a crack
σ	Stress
σ_c	Critical Stress / Cohesive stress
σ_f	Failure stress
γ_s	Surface energy of crack side

Chapter 1

Introduction

1.1 Motivation

Oslo government building was in 2011 exposed by a terror attack in the form of a car bomb. The blast pressure pulverized nearly all glass windows in the building. Shattered glass fragments with high velocities were ascertained to be the primary reason for injuries, with a total of 209 out of 325 injuries associated with glass lacerations [2]. The government building after the blast event can be seen in Figure 1.1. In the aftermath of this event, the demand and interest around safety glass have increased significantly. To be able to design safety glasses properly, a thorough understanding of both the blast load and the material properties are needed. These aspects will be studied in this thesis.

Figure 1.1: The government building in Oslo after the terror attack the 22nd July 2011 [1]

The conventional safety glass used in these days is laminated glass, which normally consists of two glass panes with an interlayer in between. The most commonly interlayer used is polyvinyl butyral (PVB). This is a highly strain rate dependent rubbery material, which has its purpose of preventing glass fragments and the actual blast pressure to enter the building when exposed to a blast loading [3].

In this thesis, there was conducted quasi-static four point bending tests of laminated glass specimens to estimate the fracture strength during quasi-static loading. Blast tests carried out on both single float glass, and laminated glass panes were conducted to study the response during blast loading. The tests were conducted respectively in the laboratory at the Department of Structural Engineering and the SIMLab shock tube facility at NTNU.

Numerical simulations were carried out of the four point bending tests, a PVB tensile test conducted by Hopper et al. [3] and the blast experiments to see if the experiments could be recreated numerically. IMPETUS Afea Solver was used as the numerical tool in all simulations, and node splitting was applied for the blast simulations. MATLAB were used for processing of all experimental data.

The thesis is divided into 9 chapters, briefly described under:

Chapter 2 - Theory. In this chapter, the theoretical background of different mathematical and mechanical theorems are presented.

Chapter 3 - Materials and material modelling. This chapter presents the different materials used in the experiments. It also covers how some of them are modelled in IMPETUS.

Chapter 4 - Experiments. In this chapter the experimental part of the thesis are presented. Both experimental setup and results of both the four point bending tests and blast experiments are presented.

Chapter 5 - Numerical modelling - Four point bending test. This chapter covers the numerical modelling of the four point bending test.

Chapter 6 - Numerical modelling - PVB tensile test. Inverse numerical modelling in IMPETUS of the PVB tensile test conducted by Hooper et al. [3] is presented. A best-fit curve by using the Bergström-Boyce material model is shown.

Chapter 7 - Numerical modelling - Blast Tests. Numerical modelling of both float glass and laminated glass in IMPETUS is presented. Results from the simulations are compared to the results of the experiments, and a best-fit model for both glass types is shown.

Chapter 8 - Conclusion. The most important observations and findings from the experimental and numerical work in the thesis are presented in this chapter.

Chapter 9 - Further work. Suggested further work based on the author's experiences in the work of this thesis is presented.

1.2 Background

After the increase of terror attacks and the attack in Oslo, there has been an increase in research on modelling of laminated glass and an increase in the modelling of laminated glass[2; 4]. Laminated glass consists as mentioned, usually by two glass panes with a PVB interlayer. The composition of the different materials and the interaction between them results in several challenges when modelling laminated glass. Some aspects that need consideration are the glass material model, the PVB material model and the modelling of the connection between the layers. A literature study was conducted to find a background past simulations. This section covers the findings.

Material modelling

There are several ways of modelling float glass. Early fracture mechanics as developed by, e.g Griffith [5], predicts that fracture in brittle materials to be caused by the propagation of a microcrack leading to failure. Since then, different material models have been developed and tried. Until recently, a linear elastic material model was used for glass with a fracture criterion [6; 7; 8]. With the increase of the understanding of glass, new material models were developed. Material models with dynamic material parameters were introduced, and dynamic material models were developed. Grujicic et. al [9] and Johnson and Holmquist [10] developed so-called macro-level models which are popular choices in modelling today [2].

In their Master thesis, Brekken and Ingier [11] tested a number of material models in the glass including Johnson-Holmquist 2 material model, SIMLab Metal Model and SIMLab Brittle Materials Model, with varying results. The Johnson-Holmquist Ceramic model includes the strain rate effects, material damage and the confinement effect [2]. To the authors' knowledge, LS-DYNA has been the most common codes used in the simulations. A variation of shell elements and solid elements was used by the different researchers. Good results have been produced with shell elements when compared to non-failing glass panes by Larcher [6]. Yankelevsky [12] presented in his paper a new model to account for the stochastic properties of glass based on statistical distributions of microcracks.

In their study of the fracture mechanics in laminated glass subjected to blast load, Wei and Dharani [7] used linear solid glass elements in their model. As a material model for the glass panes, they used a linear elastic model with a failure criterion based on energy balance. Wei and Dharani conclude that for short duration blast tests, an elastic model with a fracture criteria is sufficient [8].

The material modelling of PVB has been proven to be complicated [2] due to high strain rate sensitivity and viscoelastic material bheaviour. A viscoelastic model with a generalised Maxwell series is often introduced to include the time-dependent shear modulus [3; 13]. The temperature effects are considered with the Williams-Landel-Ferry [14] equation as a way to update the shear modulus at different temperatures [3]. In the cases studied, solid elements were used in the PVB interlayer with either one or two elements in the thickness. Other material models used were rate-dependent plastic [2], elastoplastic [6; 15], hyperelastic [16], Mooney-Rivlin [17] and a Prony series spring with finite deformation viscoelasticity [18].

Delamination, adhesion and damage

An important feature of the laminated glass panes is the interaction between the glass and the PVB. The delamination properties of the laminated glass are accentuated by [19] as an important feature of energy absorption during a blast. The cohesive bond has in previous works been modelled in LS-DYNA with a contact tiebreak feature [20]. The feature enables the glass to loosen from the PVB when the stress reaches a critical level. The most used technique used to facilitate crack propagation in finite element method modelling is element erosion. With this failure modelling technique, the element is eroded when the damage in the element reaches the critical value. Failure modelling with element erosion causes a percentage of the elements to erode and affect mass and energy conservation in the simulation. As pointed out by Brekken and Ingier [11], the eroded mass is highly mesh size dependent, and the eroded mass in their simulations increased with the element size. An alternative approach is to model the failure with node splitting as presented by Olovsson et al. [21]. This technique was tested by Ilseng [22] in his master's thesis with success in the IMPETUS Afea Solver. Ilseng modelled float glass panes and laminated glass windows. With node splitting as failure model, no elements will erode, and thus the mass balance remains intact.

1.3 Scope

Laminated glass panes subjected to blast load is a complex event with numerous important aspects that need consideration. Some of the aspects are

- Glass material model
- PVB material model
- Contact modelling between the layers
- Boundary conditions
- Inclusion of the stochastic properties of the glass
- Modelling of the blast load
- Delamination during the response
- Damage criteria and fracturing in numerical simulations
- Dynamic effects

Due the limited time and the limitations of a Masters thesis, a scope was defined.

One of the key areas of focus in this thesis was the PVB material properties and the interaction between PVB and glass. This includes, the delamination properties and the effect of delamination was studied. The authors chose IMPETUS Afea Solver as the numerical modelling tool for the simulations, and the possibilities and limitations with this code in the modelling of float glass and laminated glass panes were of great interest to the authors. Node splitting is a relatively new way of modelling fracture, and the authors were interested in which ways the new technique affected crack propagation and fracture in float glass. Float glass is a brittle material with stochastic material properties. An area of focus in the thesis was to study how reliable a numerical tool is to recreate the response recorded in an experiment and investigate the limitations of IMPETUS in describing a realistic crack propagation, PVB and glass interaction and the fragmentation of the glass.

Chapter 2

Theory

2.1 Beam Theory

In this section, a brief introduction to Euler-Bernoulli Beam Theory will be given. The analytical solution will be used as a comparison with the results obtained in the experiments. The material in this section is mainly adapted from [23].

2.1.1 Euler-Bernoulli Beam Theory

Euler-Bernoulli beam theory stems from the Euler-Bernoulli equation which describes the relationship between deflection and applied load for a static beam. The differential equation is derived from looking at an infinitesimal of the beam and finding the equilibrium of forces and moments. The equation is as follows

$$\frac{d^2}{dx^2}\left(EI\frac{d^2w}{dx^2}\right) = q \tag{2.1}$$

w is the deflection as a function of the load q, flexural rigidity EI and the position x in the beam. E is the elastic modulus of the material, and I is the moment of inertia given by equation:

$$I = \iint z^2 dydx \tag{2.2}$$

where z is the distance from the neutral axis. For a composite material like laminated glass the moment of inertia will lie between an upper, I_{upper}, and a lower limit, I_{lower}. The upper limit assumes small strains in the PVB. The lower limit implies transfer of shear forces between the layers, and thus beam theory is applicable for each glass layer separately. For the case of the upper limit, the neutral axis will lie in the middle of the laminate and for the lower limit, the PVB will only separate the plies of glass, and there will exist a neutral axis in each layer. Figure 2.1 shows the bending deformations and stress distributions for the different cases.

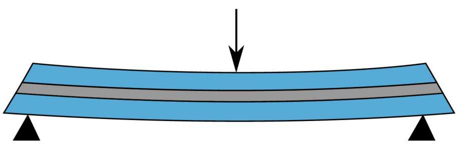

(a) Upper limit deformation **(b)** Lower limit deformation

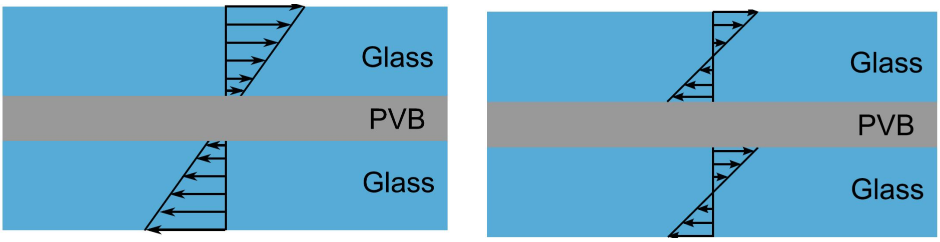

(c) Upper limit stress distribution **(d)** Lower limit stress distribution

Figure 2.1: Figures showing the deformations and the associated stress distributions for the upper and lower limit assumptions. Figure adapted from [22]

The stress distributions in Figures 2.1c and 2.1d necessitates two different expressions to calculate the moment of inertia as shown:

$$I_{upper} = \frac{b}{12}\left(d_{tot}^3 - d_{PVB}^3\right) \tag{2.3}$$

$$I_{lower} = 2 \times \frac{1}{12} b d_{glass}^3 \tag{2.4}$$

d in the equations denotes the different thicknesses described in the subscripts, and b is the width of the sample. The behaviour of laminated glass exposed to bending is found to be close to the lower boundary [24] and [25].

By differentiating the deflection of the beam with respect to x, the angle between the beam and the horizontal axis may be found. The curvature κ is obtained by differentiating the angle with respect to x, as shown:

$$\kappa = \frac{d^2 w}{dx^2} \tag{2.5}$$

For small strains the relation between curvature and strain ε is given by:

$$\varepsilon = -\kappa z \tag{2.6}$$

with z being the distance from the center of inertia. For linear elastic materials, the relationship between stress σ and strain is given by Hookes Law

$$\sigma = E\varepsilon \tag{2.7}$$

E is the Youngs' modulus of the material. By inserting Equation (2.6) into Equation (2.7) an expression for the stress in the horizontal direction (x-direction) for a monolithic specimen may be found as a function of curvature:

$$\sigma_x = -E\kappa z \tag{2.8}$$

The relationship between the bending moment and the curvature is given by the following expression:

$$\kappa = \frac{M}{EI} \tag{2.9}$$

where M is the bending moment. By combining the Equations (2.8) and (2.9) the stress in x-direction may be written as a function of the applied bending moment:

$$\sigma_x = \frac{M}{I} z \tag{2.10}$$

It is known that the maximum bending moment acting in a four-point bending test as shown in Figure 2.2, is given by the following expression [26]:

$$M_{max} = \frac{PL}{8} \tag{2.11}$$

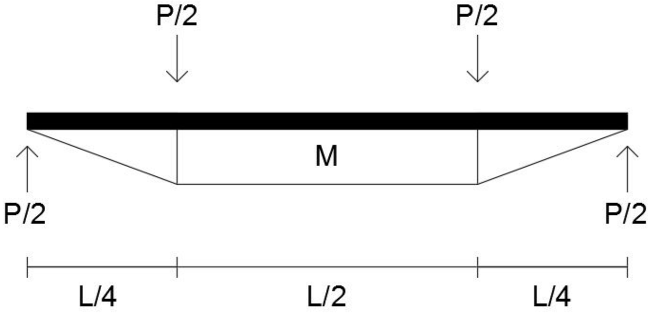

Figure 2.2: Moment diagram for a beam subject to two point loads

For a uniform beam with height h and thus $z_{max} = -\frac{h}{2}$ the expressions for ε_{max} and σ_{max} may be found by inserting Equations (2.7) and (2.10) to Equation 2.11. The expressions may be written as:

$$\varepsilon_{max} = \frac{PLh}{16EI} \tag{2.12}$$

and

$$\sigma_{max} = \frac{PLh}{16I} \tag{2.13}$$

The midpoint deflection δ_c of the beam shown in Figure 2.2 is given by the following expression:

$$\delta_c = \frac{11PL^3}{768EI} \tag{2.14}$$

From Equation 2.14 it can then be showed that Young's modulus can be calculated with the following formula:

$$E = \frac{11\Delta PL^3}{768\Delta\delta I} \tag{2.15}$$

2.2 Blast Mechanics

In this chapter, an introduction to blast loading will be presented. The contents of this section is mainly an adaptation from [27].

Blast loading is usually characterised by a rapid chemical reaction and release of energy via supersonic shock waves. The surrounding area of the explosion experiences temperatures up to 3000-4000 °C. The air around the blast is highly compressed compared to the undisturbed air in front of it. Because of this disequilibrium, the compressed air will propagate outwards from the detonation point to the surroundings in a spherical manner. The blast pressure will decrease in intensity with the cube of the distance due to the spherical blast distribution and is shown in Figure 2.3 [27].

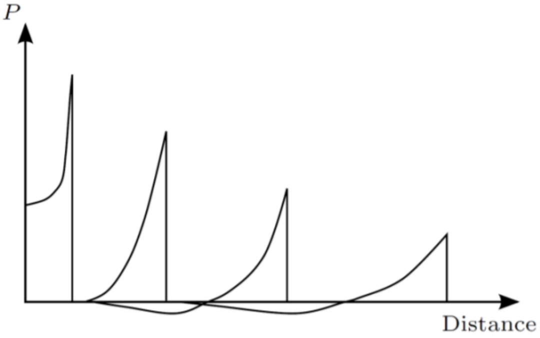

Figure 2.3: Pressure distance graph [27]

The explosion creates an incident blast wave that almost instantly arises from an ambient pressure (P_a) to a peak incident pressure (P_{so}). The pressure intensity decays fast and returns to the ambient pressure after some milliseconds. This phase is called the positive phase. After reaching the ambient pressure, a longer negative phase follows. In this phase, the pressure is below the ambient pressure thus creating a suction into the detonation centre.

When the shock wave hits a structure that is not parallel to the direction of the wave, the wave is reflected from the structure and is reinforced. The reflected peak wave pressure (P_r) is always bigger than the incident peak wave pressure at the same distance from the detonation point and is therefore also used as the design load when designing structures. The reflected pressure-time curve from the blast is commonly described with the Friedlander equation:

$$P(t) = P_a + P_r\left(1 - \frac{t}{t_+}\right)exp\left(\frac{-bt}{t_+}\right) \tag{2.16}$$

where b represent the exponential decay coefficient, t_+ and t_- the positive and negative phase respectively and t_a the reference time. Both the reflected pressure and the peak over pressure curves calculated with the Friedlander equation are presented in Figure 2.4.

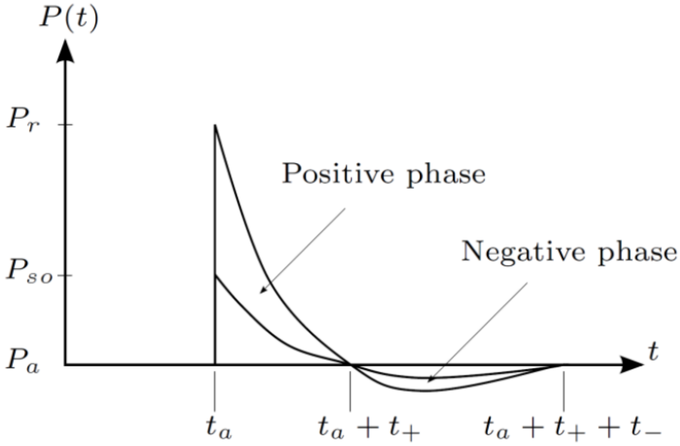

Figure 2.4: Pressure-time history for the reflected and incident pressure wave [27]

The area under the curve shown in Figure 2.4 is defined as the specific impulse i which is a measure of the total energy transferred to the structure from the explosion. In the calculation of i, both the positive and negative phase are contributing. Since the reflected pressure is defined as the actual load on the structure, the positive specific impulse may be written as

$$i_{r+} = \int_{t_a}^{t_a+t_+} P_r(t)dt \tag{2.17}$$

which can be solved analytically by inserting Equation (2.16)

$$i_{r+} = \frac{P_r t_+}{b^2}[b - 1 + exp(-b)] \tag{2.18}$$

An important remark is that the reflected wave varies with the angle of impact, α, shown in Figure 2.5. However, in this thesis experiments will only be conducted with perpendicular shock waves. Hence no further work will be done on this part [27].

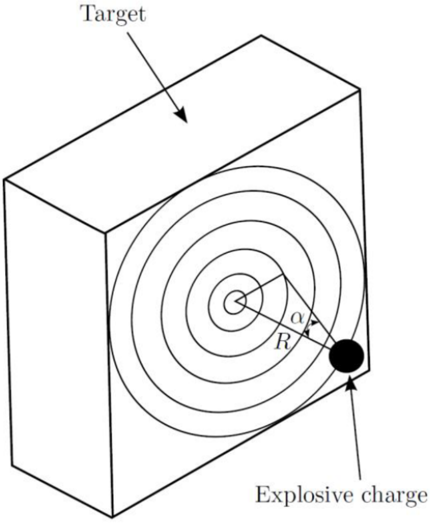

Figure 2.5: Blast load angle [27]

2.3 Ideal shock tube theory

In this section, a brief introduction to ideal shock tube theory is presented. The content is mainly adapted from [28].

Blast experiments are commonly conducted by the use of a shock tube. The tube consists of two separated chambers, one high-pressure chamber called *Driver* with pressure p_4 and one low-pressure chamber called *Driven* with pressure p_1. The two chambers are separated by a diaphragm where $p_4 > p_1$. This is illustrated in Figure 2.6.

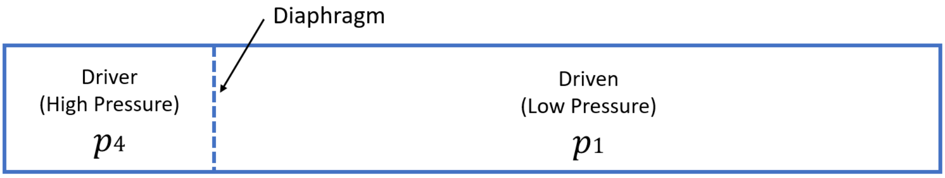

Figure 2.6: Schematic representation of the two separated chambers in a shock tube

By increasing the pressure in the Driver to the point where the diaphragm ruptures, a sudden shock wave is generated, and rarefaction waves are produced in the opposite direction. The different phases linked to the propagation of the waves is illustrated in Figure 2.7. From the initial position (Figure 2.7(a)), the high-pressure gas acts as a piston propagation into the low-pressure chamber with a velocity of u_s, which is larger than the sonic velocity of the low-pressure undisturbed Driven gas. By heating, compressing and acceleration of the driven gas, the shock wave induces a mass motion right behind the shock wave with a velocity of u_2 with pressure p_2. In the Driver, the rarefaction waves (E) propagates into the high-pressure pressure wave p_4 and increases in strength (Figure 2.7(b)). The rarefaction waves are then reflected at the back of the Driver and push in the same direction as the shock wave (Figure 2.7(c)). Because of the small ratio between the Driver-length and the Driven-length in the setup, the rarefaction waves catch up with the shock wave. This leads to a shock wave with lower strength, longer duration and with a lower velocity, similar to an explosion. (Figure 2.7(d)). When reaching the end of the shock tube where the test specimen is located (5), the incoming shock wave is reflected backwards (Figure 2.7(e)). This leads to an overpressure p_5 behind the wave that is higher than the incoming wave. The positive pressure-time curve corresponding to the wave can be fitted to the Friedlander curve as presented in Section 2.2. [28]

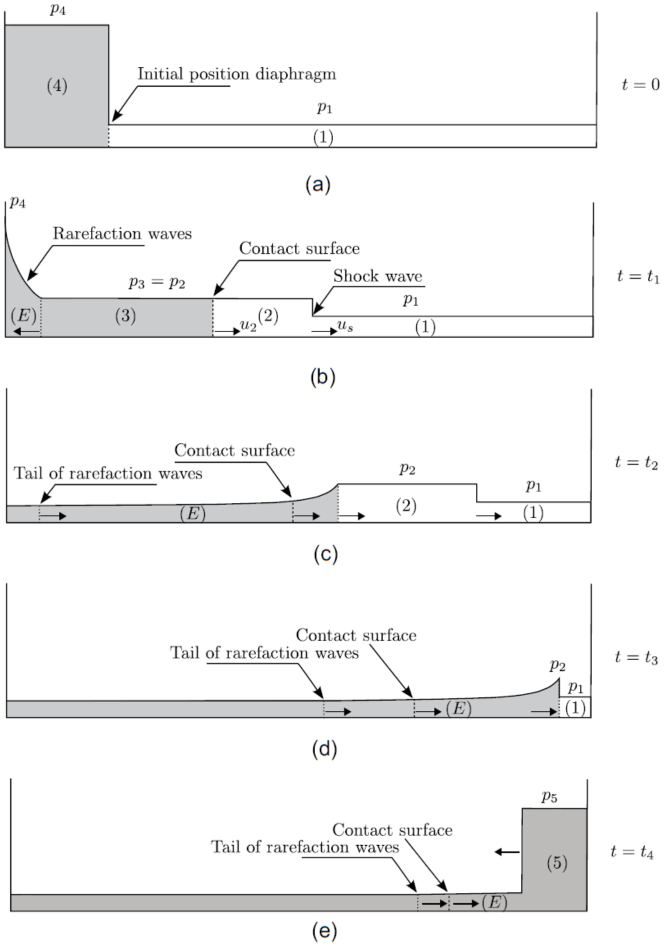

Figure 2.7: Schematic representation of the different phases when a shock wave is generated in the compressed gas gun. The figure is taken from [28]

2.4 Fracture Mechanics

To be able to understand how a brittle material like glass behaves during failure, knowledge about fracture mechanics are necessary. In this section, there will be given a brief introduction to fracture mechanics with emphasis on linear elastic fracture mechanics (LEFM). The material discussed in this section is gathered mainly from [5].

2.4.1 Fracture on an atomic scale

Fracture on an atomic scale happens when the bonds between the atoms are broken as a result of sufficient stress levels, or amount of work applied. The bonds behave as springs with a stiffness determined by the attractive forces between the atoms. The equilibrium between the atoms is defined as when the attractive and repulsive forces are equal, and the equilibrium distance is denoted x_0. When forces are applied to the system, the potential energy E_b increases according to the following expression: where P is the applied force

$$E_b = \int_{x_0}^{\infty} P dx \tag{2.19}$$

where P is the applied force The cohesive strength of the bonds may be estimated by using half a sine wave as shown in Equation (2.20). λ is the length of half the sine wave and P_c is the cohesive force.

$$P = P_c sin\left(\frac{\pi x}{\lambda}\right) \tag{2.20}$$

By assuming small displacements, $sin(x) \approx x$, the bond stiffness may be written as:

$$k = P_c\left(\frac{\pi}{\lambda}\right) \tag{2.21}$$

By multiplying both sides of Equation (2.21) with bonds per area and the length, the equation may be written with respect to Young's modulus and the cohesive strength. Solved with respect to the cohesive stress σ_c:

$$\sigma_c = \frac{E\lambda}{\pi x_0} \tag{2.22}$$

At fracture, two surfaces are created. The energy at each surface is equal to one half of the total fracture energy and is estimated by the following equation:

$$\gamma_s = \frac{1}{2}\int_0^{\lambda} \sigma_c sin\left(\frac{\pi x}{\lambda}\right) dx = \sigma_c \frac{\lambda}{\pi} \tag{2.23}$$

Solved for σ_c and by substituting Equation (2.22) into the Equation (2.23), the estimate of the cohesive stress may be written as:

$$\sigma_c = \sqrt{\frac{E\gamma_s}{x_0}} \tag{2.24}$$

In theory, the fracture in a material occurs when sufficient energy from stress or work is applied to break the intermolecular bonds, the experimental strengths of brittle materials have been found experimentally to be four orders of magnitude below the calculated fracture strength. The reasons for the discrepancies were studied by, among others, Inglis in 1913 [29].

The main reason for the gap between the experimental and the theoretical strength of brittle materials was found to be discontinuities, i.e. flaws and cracks, in the material causing a concentration of stresses at the edges of the defects. Inglis studied an elliptical hole with length $2a$ and width $2b$ in a flat plate subjected to uniaxial tension stress perpendicular to the crack and compared the stresses acting on the tip of the crack, with the loading stress in the plate, see Figure 2.8.

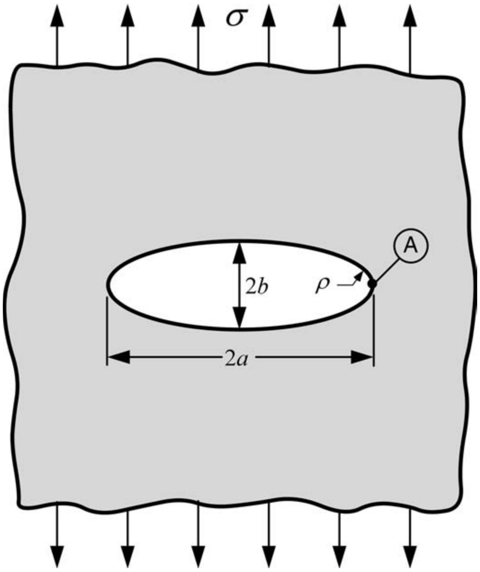

Figure 2.8: Inglis model using an eliptical hole, from [5]

The stress is point A is given by Equation (2.25).

$$\sigma_a = \sigma \left(1 + \frac{2a}{b}\right) \tag{2.25}$$

For thin cracks, when a increases relatively to b, a more convenient way to write the equation is by expressing the crack stress as a function of the radius of the curvature $\rho = \frac{b^2}{a}$.

$$\sigma_a = \sigma \left(1 + 2\sqrt{\frac{a}{\rho}} \right) \tag{2.26}$$

A problem occurs when the curvature goes toward zero or when $a >> b$. For an infinitely sharp crack, with a width close to zero, the stress in the tip goes towards infinity, which in other words means that the material will fail due to an infinitesimal stress, which is of course physically impossible. For metals, the initiation of an infinitely sharp crack is prevented by the plastic deformation of the metal and thus a blunting of the crack which slows down the crack propagation. For ceramic materials like glass, the atom size stops the propagation. By substituting the curvature with the inter-atomic distance x_0, Equation (2.26) estimates the tip stress of an atomically sharp crack and may be written as:

$$\sigma_a = \sigma \left(1 + 2\sqrt{\frac{a}{x_0}} \right) \tag{2.27}$$

When $\sigma_a = \sigma_c$, the material fractures as a result of torn atomic bonds. By setting Equation (2.27) equal to Equation (2.24) the failure stress may be estimated to be the following

$$\sigma_f = \sqrt{\frac{E\gamma_s}{4a}} \tag{2.28}$$

Equation (2.28) is only a rough estimate of the remote failure stress in the material, considering the assumptions made by Inglis are not valid on an atomic scale.

2.4.2 The Griffith Energy Balance

Based on the work of Inglis [29], Griffith [30] formed a crack theory based on potential energy in 1920. From the first law of thermodynamics, it is known that a system which goes from a state of non-equilibrium to equilibrium will decrease in energy. Transferred into the world of fracture mechanics the equivalent is that a crack can form or grow only if the formation of the crack causes a decrease in energy or if the energy remains constant. Hence a definition, based on energy conservation, of the critical condition is when crack growth occurs in equilibrium with no change in total energy.

The propagation of a crack necessitates sufficient potential energy available to surpass the surface energy. In Figure 2.9 a plate with thickness B, crack length $2a$ and crack width $b << a$ is shown. The plate is loaded with stress σ and the crack area is denoted A. For an incremental increase of the crack area, the equilibrium condition may be written as:

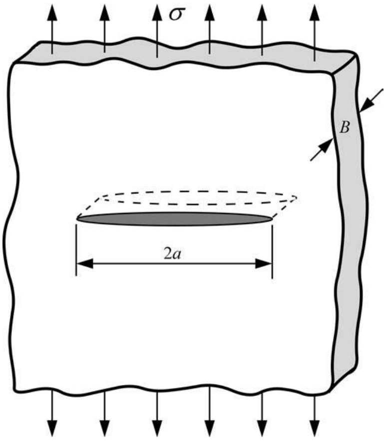

Figure 2.9: Infinitely wide plate subjected to tensile stress perpendicular to crack [5]

$$\frac{dE}{dA} = \frac{d\Pi}{dA} + \frac{dW_s}{dA} = 0 \Rightarrow \frac{dW_s}{dA} = -\frac{d\Pi}{dA} \tag{2.29}$$

where E is the total energy, Π is the supplied potential energy and W_s is the work required to create the new surfaces of the crack. By using the expression for crack stresses derived by Inglis, Griffith showed that:

$$\Pi = \Pi_0 - \frac{\pi\sigma^2 a^2 B}{E} \tag{2.30}$$

where Π_0 is the total potential energy in the un-cracked plate, and σ is the remote tensile stress applied on the plate. a and B are geometrical quantities from Figure 2.9. During the formation of a crack, two new surfaces are created, which implies that the work done is given by:

$$W_s = 4aB\gamma_s \tag{2.31}$$

With γ_s being the surface energy from Equation (2.23). Hence the two parts of Equation (2.23) may be written as:

$$-\frac{d\Pi}{dA} = \frac{\pi\sigma^2 a}{E} \tag{2.32}$$

and

$$\frac{dW_s}{dA} = 2\gamma_s \tag{2.33}$$

By merging Equation (2.32) and (2.33) the failure stress σ_f is found by:

$$\sigma_f = \sqrt{\frac{2E\gamma_s}{\pi a}} \tag{2.34}$$

This is the fracture stress applied remotely on the plate which causes cracks to open and propagate.

As a way to make the work of Griffith more convenient for use in engineering, Irwin [31] defined an energy release rate, denoted G. G denotes the available energy in an increment of a crack propagation. Note that G does not refer to the time derivative of the energy, but to the rate of change in energy with respect to change in the area. G is defined by Equation (2.35).

$$G = -\frac{d\Pi}{dA} \tag{2.35}$$

When G reaches a critical value G_c is given by:

$$G_c = \frac{dW_s}{dSA} = 2w_f \tag{2.36}$$

With W_s as defined in Equation 2.31. w_f is the fracture energy and G is a material property fracture toughness

2.4.3 Stress Analysis of Cracks

A crack may be subjected to three different types of loading, or a combination of the three. As seen in Figure 2.10 mode I is a crack subjected to a load perpendicular to the crack, mode II is in-plane shear loading and mode III describes out-of-plane shear loading. As an alternative to the Griffith energy balance method with fracture toughness from Irwin, a way to analyse stress during crack propagation is to examine the stress concentration in a micro-crack under loading. Mode I cracks requires the least amount of energy to develop.

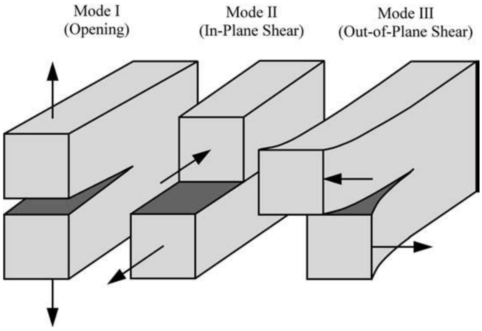

Figure 2.10: The three loading modes applicable to a crack [5]

By introducing a stress intensity factor K, the stress concentration in the crack is described using the subscripts I, II and III to describe stress concentrations related to the different modes of fracture. For the stress intensity factor to be useful, a relation between the applied remote stress, σ, and the stress in the tip is needed. For a crack in a plate described in Figure 2.9, K_I is derived and found to be:

$$K_I = \sigma\sqrt{\pi a} \tag{2.37}$$

For linear elastic materials the parameters K and G are related by the following equation:

$$G = \frac{K_I^2}{E'} \tag{2.38}$$

For plane stress $E' = E$ and for plane strain $E' = \frac{E}{1-v^2}$. When the stress intensity factor reaches the critical value K_c, the material fractures due to crack propagation. The material parameters G_c and K_c may be found by experimental testing done in accordance with e.g., ASTM C1421 [32].

2.5 Statistical Treatment of Strength in Brittle Materials

Glass is a brittle material with stochastic material parameters. It may therefore be necessary to describe the strength of glass with statistical parameters from different distributions. This section will briefly cover Weibull distribution and Weakest Link Theory. The theory presented in this section is mainly an adaptation from [33] and [34].

2.5.1 Weibull Distribution

Weibull distribution is a statistical distribution presented by Weibull in 1939 [35]. After the publication Weibull distribution has become one of the most commonly used distribution when describing strength in brittle materials [12]. Of the Weibull distributions used, the variants with two and three parameters are the most frequently used. In this section, the variant with two parameters will be covered. The probability density function of the two-parameter Weibull distribution with a random continuous variable x is defined as follows:

$$f(x;\alpha,\beta) = \begin{cases} \alpha\beta x^{\beta-1}e^{-\alpha x^{\beta}}, & x > 0 \\ 0, & \text{elsewhere} \end{cases} \tag{2.39}$$

β is called the shape parameter and is larger than 0, α is a scale parameter. The corresponding cumulative probability density function is given by:

$$F(x) = \int_{-\infty}^{x} f(t;\alpha,\beta)dt = 1 - e^{-\alpha x^{\beta}} \tag{2.40}$$

Figure 2.11 shows a qualitative description of some Weibull distributions with varying β-vaules and α=1.

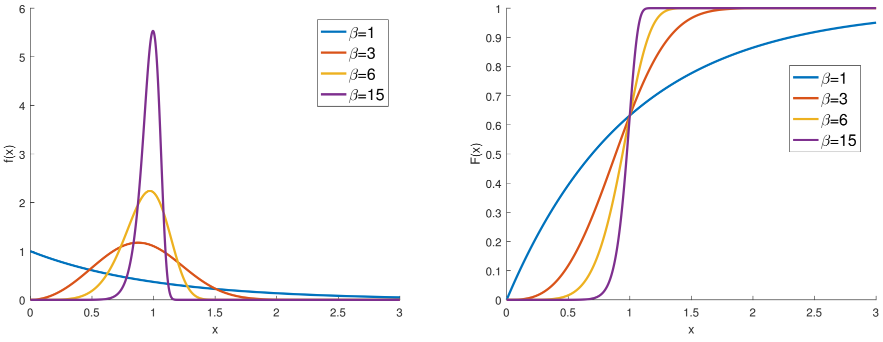

(a) Density function **(b)** Cumulative probability distribution

Figure 2.11: A qualitative description of Weibull distribution with varying α and β

As seen in the Figure, for β=1 the distribution is reduced to an exponential distribution while for β¿1 the distributions resembles a skewed normal distribution. The width of the skew bell curves are decided by the inverse of β, the higher the value the narrower is the curve.

For engineering purposes, and especially for interpreting strength testing data, a commonly used representation of the Weibull distribution is

$$f(\sigma) = \frac{m}{\sigma_0}\left(\frac{\sigma}{\sigma_0}\right)^{m-1} exp\left(-\left(\frac{\sigma}{\sigma_0}\right)^{m}\right) \tag{2.41}$$

with the corresponding cumulative density function

$$F(\sigma) = 1 - exp\left(-\left(\frac{\sigma}{\sigma_0}\right)^{m}\right) \tag{2.42}$$

For this case β has been replaced by the Weibull modulus, m. m is used to describe the dispersion of measured critical stress, σ_{cr}, for a test series. The characteristic strength of the material, σ_0, has in Euquation 2.41 replaced m.

2.5.2 Weakest Link Theory

The following section is adapted mainly from [34].

Weakest link theory and Weibull analysis are often used interchangeably, and some have stated that Weibull analysis is based directly on or derived from weakest link theory[34]. Zok [34] argues in his paper that the two theories are different and not based on one another. Weakest link theory states that the survival probability of a brittle material is dependent of the survival probabilities of each of the volume elements in the solid according to the following formula:

$$S = \prod_{i=1}^{N} S_i(\sigma) \tag{2.43}$$

Where S is the total survival probability and S_i is the survival probability of element with the corresponding stress σ. N is the number of elements. With a total volume V in the solid, each element has volume V_i and thus N may be written as $N = V/V_i$. By taking logarithms on both sides, Equation (2.43) may be written as:

$$ln(S) = \sum_{n=1}^{N} ln(S_i(\sigma)) \tag{2.44}$$

Given that S_i is a continuous function and by using the relationship between V and N, Equation (2.44) may be rewritten to:

$$ln(S) = \frac{1}{V_i} \int_V ln(S_i(\sigma))dV \tag{2.45}$$

and thus the failure probability $F = 1 - S$ is written as:

$$F = 1 - [exp(ln(S_i(\sigma)))]^{V/V_i} \tag{2.46}$$

Equation 2.46 is a statement of weakest link theory.

2.6 Digital Image Correlation (DIC)

An efficient way of recording data on deformations and strains during experiments is with the use of *Digital Image Correlation* or DIC-analysis. Especially for blast tests DIC is crucial to be able to record information during the experiments, due to e.g. the high velocities and the fast fracture of a glass pane. In this section, a brief introduction of DIC and an introduction to eCorr, the in-house DIC program used, will be given. The material in this section is mainly adapted from [36] and [37].

DIC analysis is a non-contact measuring technique based on comparisons between images taken at different times during an event or experiment. It works by comparing the pictures and tracking the movement of blocks of pixels or selected subsets from image to image. From the pixel or subset movement, 2D and 3D vector fields and strain maps may be generated using DIC software, and the displacement of each pixel or subset is tracked. For the DIC analysis to work effectively, the specimen or object in focus should have a random pattern of high contrast and intensity level, often solved with a black and white dotted spray paint or with black and white stickers. For subset tracking, this is solved with markers painted on the specimen. With DIC analysis, traditional measuring devices like extensometers and strain gauges may become excessive. As opposed to an extensometer and strain gauge, the DIC analysis can record large strains over a big area which is beneficial when dealing with non-linear analysis and biaxial strains. For glass fragmentation due to blast loading, DIC analysis is can be a useful tool, as other measuring equipment,like extensometers or gauges, would most likely be destroyed by the blast or by glass fragments.DIC analysis is easy to use and, in contrast to a single laser, DIC is able to track several points during experiments.

To easier enable the study of crack propagation in the glass, subset tracking is the preferable choice when tracking blast experiments. The program used for the analysis in this thesis is a program called *eCorr*, developed by Dr Egil Fagerholt [36]. In eCorr, subsets are added and customised to the sample in the reference image. Then a global finite element formulation is used to track the displacement of the subsets from picture to picture. After the analysis of the pictures taken during the experiment, displacements may be exported as .txt files or plotted directly in the program. In Figure 2.12 the interface of eCorr is shown with the use of subset tracking on a laminated glass pane during a blast experiment. For a 3D DIC analysis two cameras are needed, and the cameras need to be calibrated. The calibration process must be done before the tests and may be done with a checked pattern on a cylinder which is placed at different locations in the focus area of the cameras. For a more thorough description of DIC, eCorr and the calibration process, the interested reader is directed to [28].

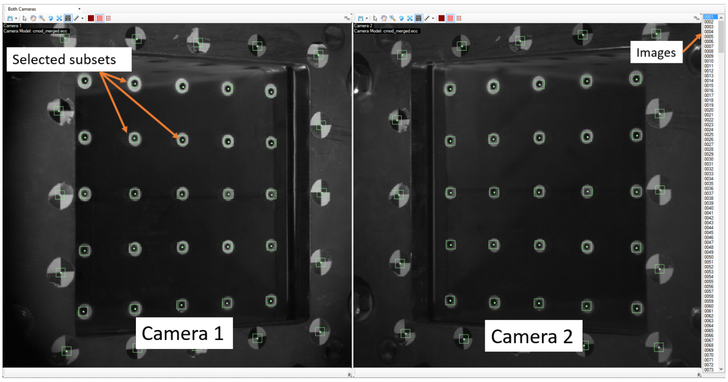

(a) Interface prior to analysis with two cameras and subsets marked with green

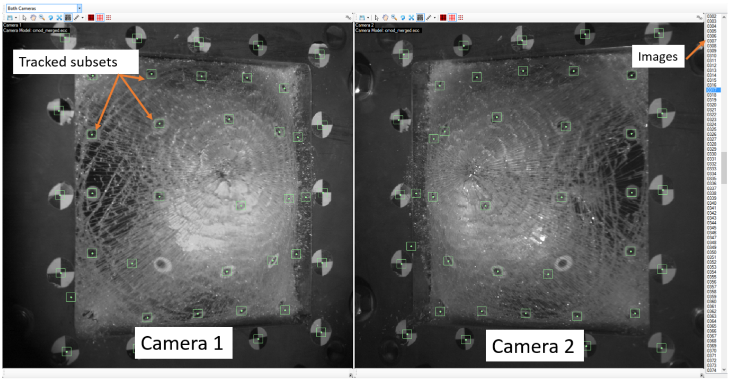

(b) Interface during analysis with tracked subsets marked in green

Figure 2.12: DIC interface

2.7 Explicit vs. Implicit FEM

The numerical analyses done in this thesis are done with the finite element method (FEM) solvers. The concepts of FEM will not be presented or discussed in this thesis, and the interested reader is directed to [38]. In this section, a brief introduction to the *explicit* and *implicit* solution methods will be given, and a comparison with pros and cons will be presented. The material in this section is mainly adapted from [38] and [39].

The mathematical formulation for a structural problem is given by:

$$M\ddot{D} + C\dot{D} + R^{int} = R^{ext} \tag{2.47}$$

which for FEM has to be on discrete form. The resulting equation is:

$$[M][\ddot{D}]_n + [C][\dot{D}]_n + [R^{int}]_n = [R^{ext}]_n \tag{2.48}$$

In this section, the notation [] signifies a matrix. $[M]$ is the mass matrix of the structure, $[C]$ is the damping matrix and $[R^{int}]_n$ is the internal forces in the system. $[R^{int}]_n$ is often denoted $[K][D]$ with $[K]$ being the stiffness matrix of the system. $[D]_n$ is the displacement matrix and $[\dot{D}]_n$ and $[\ddot{D}]_n$ are the velocity matrix and acceleration matrix respectively at time $t = n$. All information before and including time step n is assumed known.

2.7.1 Explicit method

The explicit method solves the equation of motion directly for each step without equilibrium check. The displacement at each time step is obtained directly from the equilibrium conditions at one or more preceding time steps. This makes it fast and computationally efficient. A common way to solve Equation (2.48) is with the use of the Central Difference Method with half steps.

By assuming a $[M]$ that is constant in time, the acceleration matrix of an increment may be found with the following equation:

$$[\ddot{D}]_n = [M]^{-1}\left([R^{ext}]_n - [R^{dmp}]_{n-1/2} - [R^{int}]_n\right) \tag{2.49}$$

$[R^{dmp}]$ are the damping forces. With the acceleration at time n known, the velocity may be found at time $n+1/2$. By assuming a fixed time step Δt, the velocity may be calculated with the following equation:

$$[\dot{D}]_{n+1/2} = [\dot{D}]_{n-1/2} + \Delta t[\ddot{D}]_n \tag{2.50}$$

With the velocity known at time $n + 1/2$ the displacement may be derived at time step $n + 1$:

$$[D]_{n+1} = [D]_n + \Delta t[\dot{D}]_{n+1/2} \tag{2.51}$$

After finding the displacements at time step $n + 1$, the internal forces may be calculated:

$$[R^{int}]_{n+1} = [K][D]_{n+1} \tag{2.52}$$

With Equation (2.52), the algorithm for a time step is finished and the calculations for the next time step may begin.

As seen in the scheme for the half-step method, no iterations are done in each step, and there are no checks for convergence. There is no equation solving at each step, and this makes each step relatively inexpensive. The biggest obstacle of the half step method is that the method is only *conditionally stable*. For the solution not to ”blow up” the time step Δt must be:

$$\Delta t \leq \Delta t_{cr} = \frac{2}{\omega_{max}} \left(\sqrt{1 - \xi^2} - \xi \right) \tag{2.53}$$

In Equation (2.53), ω_{max} is the highest natural frequency for any element in the model and ξ is the corresponding damping ratio in the ω_{max} mode. Due to the maximum time step criterion, explicit algorithms may be unfit for quasi-static simulations with a long running time. Measures to reduce the running time without introducing dynamic effect are time scaling or mass scaling. For a more thorough introduction to explicit methods, the reader is directed to [40].

2.7.2 Implicit Method

In the implicit methods, a series of equations are solved at each step of the time integration, making it computationally expensive relatively to the explicit methods. Both convergence checks and iterations are done at each step. The displacement $[D]_{n+1}$ is found indirectly (implicitly) from the equilibrium equations in the corresponding time step, resulting in non-linear algebraic equation solving at each time step. The most commonly used implicit methods are unconditionally stable, but the accuracy of the results increase with the decrease of Δt. In general, an implicit method requires several orders of magnitude fewer steps than an explicit method.

A commonly used implicit method is the HHT-α method. When using this method the following equation has to be solved for each time step:

$$\begin{split}[M][\ddot{D}]_{n+1} + (1 + \alpha_H)[C][\dot{D}]_{n+1} - \alpha_H[C][\dot{D}]_n + (1 + \alpha_H)[K][D]_{n+1} - \\ \alpha_H[K][D]_n = [R^{ext}]_\alpha\end{split} \tag{2.54}$$

In Equation (2.54) the notations are the same as in Equation (2.48). For a load varying linearly over a time step $[R^{ext}]_\alpha$ is given by the following equation:

$$[R^{ext}]_\alpha = (1 + \alpha_H)[R^{ext}]_{n+1} - \alpha_H[R^{ext}]_n \tag{2.55}$$

In the two previous equations, α_H is a constant used to implement algorithmic damping in the system. For $\alpha_H = 0$ the method reduces to the so-called Newmark method [40] while for $\alpha_H < 0$ algorithmic damping is introduced. The HHT-α method is unconditionally stable for:

$$-\frac{1}{3} \leq \alpha_H \leq 0 \tag{2.56}$$

Decreasing α_H increases the numerical dissipation while maintaining second order accuracy, which makes the HHT-α method more efficient at suppressing high-frequency noise than the standard Newmark-methods. The interested reader is directed to [40] for a more thorough description.

2.7.3 Pros and Cons

As a summary of the two methods the following presents some of the pros and cons of the two different methods

Table 2.1: Table showing some of the pros and cons of the two discussed methods.

	Pros	Cons
Explicit	Equation solving not necessary. Equilibrium iterations not necessary. Computationally inexpensive. Ideal for high-speed dynamic simulations, such as blast loading. Usually reliable for problems involving discontinuous non-linearities.	Conditionally stable. Requires small steps.
Implcit	Unconditionally stable. Fewer increments needed. Time increment size not limited. Ideal for quasi-static loading where response period is long.	Non-linear equations needs solving at every step. Each step computationally expensive. Convergence must be obtained for each increment.

2.8 Impetus Afea Solver

IMPETUS Afea Solver is an explicit non-linear finite element program, which is designed for high precision, robustness and user friendliness. The program is based on as few user defined parameters as possible. As an example, the analyses are restricted to the use of explicit time integration and fully integrated solid elements. This will in many cases give a more accurate solution but comes at a price of higher computational cost.

As a measure to reduce the running time of the simulations, IMPETUS Afea Solver supports GPU acceleration in the simulations. The graphics processing unit (GPU) have thousands of cores to process parallel workloads efficiently. The GPU offloads compute-intensive portions of the simulation for itself, while the remaining of the simulation is carried out in the central processing unit (CPU). This is illustrated in Figure 2.13. [41]

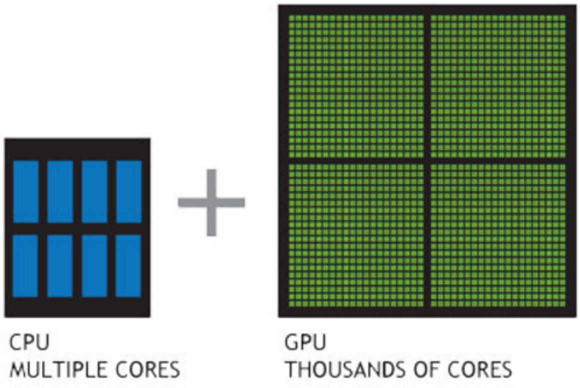

Figure 2.13: GPU have thousands of cores to process parallel workloads efficiently, taken from [41]

In addition to element erosion, node splitting is implemented as a technique to describe fracturing in IMPETUS Afea Solver. With the element erosion technique, the element is eroded when the damage reaches a given damage criterion. For brittle materials like glass or ceramics, the failure of the material is caused by crack propagation. With element erosion, the model will normally experience an unphysical response where a portion of the glass elements is removed. This violates the conservation of energy and conservation of mass. With node splitting, nodes are instead separated when the fracture criteria is reached, and the elements are not eroded. A downside with node splitting is that it require higher computational power than element erosion.

IMPETUS supports nine different types of solid elements:

1. Tetrahedrons (linear/ quadratic/ cubic)
2. Pentahedrons (linear/ quadratic/ cubic)
3. Hexahedrons (linear/ quadratic/ cubic)

where the cubic 64-node hexahedron element is illustrated in Figure 2.14.

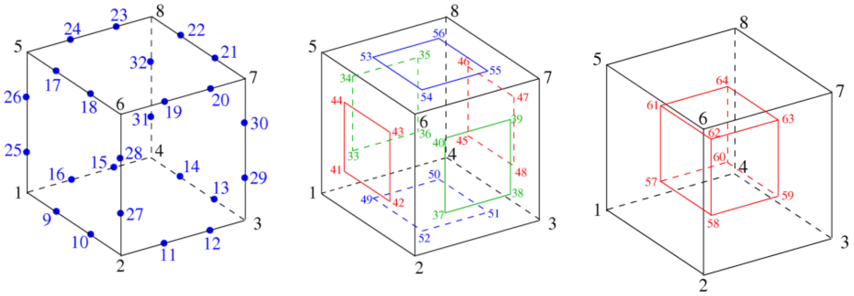

Figure 2.14: Cubic hexahedron element used in IMPETUS. Taken from [42]

The interface of IMPETUS Afea Solver contains four different section modes; Assemble, Solve, Post and Editor mode. In the Editor mode, the user defines everything in the model like the geometry, load and boundary conditions. This is done by using predefined commands for the different parts. To see how the model looks before simulating it, assemble mode can be utilised. Solver mode is used to run simulations and control the progress of the simulations. The post-processing mode gives the user a graphical representation of the completed simulations.

Chapter 3

Materials and material modelling

3.1 Materials

In this section, a brief introduction to the different materials studied in this thesis will be given.

3.1.1 Float glass

Window glasses are usually made out of soda-lime glass, also called soda-lime-silica glass.. These glasses mainly consists of three constituents, $SiO_2(70-75\%)$, $Na_2O(12-16\%)$ and $CaO(10-15\%)$[33]. In molten condition, the atoms are in continuous motion and randomly structured, but at the cooling point the atoms stabilise and form a structured network, a crystal. If the cooling process is done rapidly in a suitable manner, the substance will not have time to rearrange into the crystalline state, and only a portion of the atoms will move. This prevents the formation of crystals, and the elastic solid that is created is called glass. Glasses are amorphous solids.

Float glass is a brittle material, and a set of glass specimens with identical geometry and loading may differ significantly from each other. This is due to microcracks that are randomly distributed on the surface. Fracture is initiated when the one of the first microcracks opens due to the stress acting on it, ans is defined as the critical microcrack. Because of these microscopic flaws, the critical microcrack does not necessarily occur at the place with the highest stress [12]. The strength of float glass has also been proven to be strain rate dependent, but the Young's Modulus is shown to be rather insensitive to strain rate [43].

3.1.2 Polyvinyl Butyral (PVB)

Polyvinyl Butyral (PVB) is an organic polymer with the chemical formula $C_8H_{14}O_2$. PVB is the most used interlayer in the production of laminated glass due to good adhesive properties [3]. When utilised in a lamination process under the right temperature and pressure, the PVB becomes optically clear and binds the two glass plates together. The material behaviour of PVB is highly non-linear, time dependent and PVB can be extended to several times its length without fracturing [3]. Several articles have been written on PVB and its mechanical properties [3; 44; 45]. Tensile tests of PVB have been conducted over a range of loading speeds, and it has been found that PVB is a highly strain rate sensitive material. This is shown in Figure 3.1, taken from [3]. As seen, both the magnitudes of stress and the shape of the stress-strain curve varies significantly with the difference in strain rates. For this reason, a material model which includes the strain rate may be necessary to describe the PVB response correctly [44]. The most common material test conducted on PVB is a uniaxial tension test of a dog-bone specimen before the lamination process [3; 44], but there is little research on PVB material properties after the lamination. In his Masters Thesis, Ilseng [22] conducted tensile tests on pre-cracked laminated glass specimens at different strain rates to determine material properties after lamination, but due to high delamination during the experiments, no material properties could be extracted.

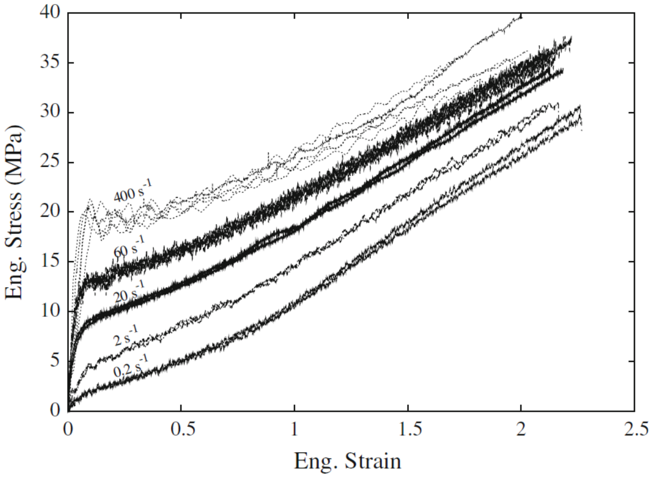

Figure 3.1: Stress-strain curve for PVB at different strain rates taken from [3]

3.1.3 Laminated glass

In this section, the behaviour of the composite laminated glass will be presented. The information is mainly an adaption of [6], [22] and [46].

Laminated glass is a form of composite material that is widely used for blast resisting windows. Laminated glass windows are made out of two or more glass panes laminated together with one or more polymer interlayers. In the components studied in this thesis, polyvinyl butyral (PVB) is used as interlayer together with two annealed glass panes as seen in Figure 3.2).

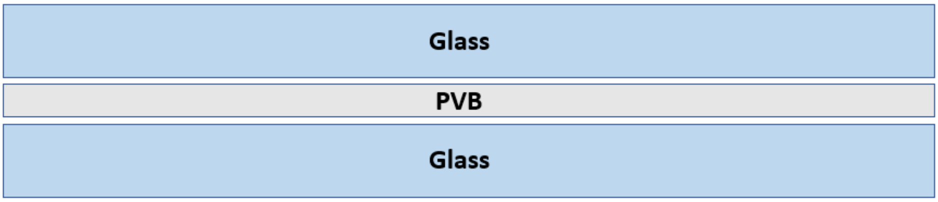

Figure 3.2: A general setup of laminated glass

There are two main reasons for using laminated glass instead of single layered glass when designing blast resisting windows. Firstly, the adherent material properties of PVB prevents shattered glass to fly freely after being subjected to a blast wave . High-speed glass fragments can cause major damage or can even be deadly, thus holding the glass together is important. Secondly, the ductile behaviour of PVB gives the window strength even after glass breakage, preventing high energy blast waves from entering the structure. Additionally the PVB can dissipate the imposed energy due to large deformations [22].

The adhesion between the PVB and the glasses is of great importance for the laminated glass when it comes to performance and ductility under blast loads. For the adhesion to be sufficient, a well performed laminating process is essential. Before the process can begin, the glasses needs to be purified properly, and the condition of the PVB must be proved to be at a certain level. The laminating process is carried out in an autoclave under high pressure and temperatures, and the maximum adhesion level will safely be achieved if the process is done properly. The adhesion is formed by the combination of chemical and mechanical bonds between the glass and the PVB. The PVB can be classified as a copolymer because it is structured up of one non-polar butyral group and one highly polar vinyl alcohol group, which is highly compatible with water. The glass is dominated by polar silanol groups ($Si - OH$) that are formed on the surface of the glass when exposed to water. When the PVB and the glass are compressed together under high pressure and temperatures in the autoclave, a dense network of weak hydrogen bonds are formed. This network is eventually structured to some extent true chemical bonds. [46]

The breakage of a laminated glass pane can be divided into five different phases described under. This is also illustrated in Figure 3.3.[6]

1. Elastic behaviour of the glass panes
2. The backside glass pane in tension break - the one in compression is still intact
3. The second glass pane break and the PVB interlayer behaves elastically
4. The PVB interlayer behaves plastically, and the shattered glass is kept together with the PVB
5. The interlayer fails by reaching its limit strength or rupture caused by glass shards

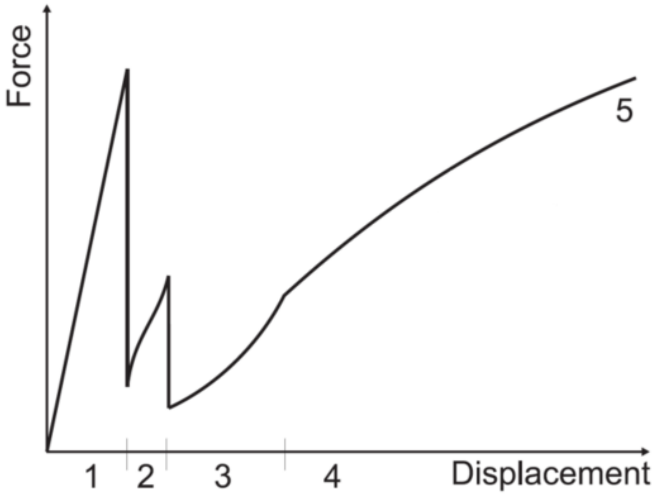

Figure 3.3: Phase diagram for laminated glass breakage. Adapted from [6]

3.1.4 Effects of Delamination in Laminated glass

In this section, the effects of delamination of laminated glass are briefly described. Delamination of laminated glass panes affects the properties of the laminated glass and is therefore of importance when designing. The contents of this section is mainly adapted from [19; 4].

The interaction between the PVB and the two glass layers affects the strength and durability of the laminated glass. Delamination may be defined as a reduction or a total loss of the adhesion between glass and the laminate. Delamination may be due to e.g. a non-proper manufacturing process or careless treatment of the glass, and delamination is also an important feature during failure of laminated glass. Del Linz et. al [19; 4] found in their blast load experiments that the delamination in the glass resulted in a plateau in the force-displacement curve, which resembled a material with plastic properties at large strains. By studying the reaction forces in the supports during the blast load and the mid-point deflection of the glass, Del Linz et al. [4] plotted the force displacement curve for their blast experiment. As seen in Figure 3.4 the glass behaves with an elastic response until the glass breaks. In the post crack curves, Del Linz et al. argues that the plateau is a result of a combination of the elastic behaviour of the PVB and the progressive delamination of the glass. The interested reader is referred to [4] for a more thorough description of the experiment.

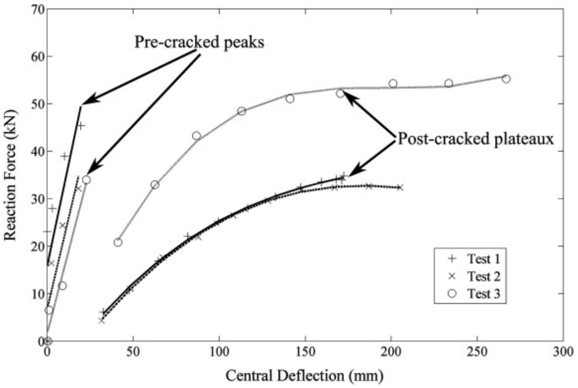

Figure 3.4: Results showing the different behaviours of laminated glass subjected to blast load, adapted from [4]

In [19] the delamination properties of laminated glass with PVB and PVB strength were tried tested by cracking the glass before performing a tensile test. Pre-cracked laminated glass specimens were subjected to tensile stress in a uniaxial tension test. With the glass cracked on both sides of the PVB, the glass did not contribute to the strength in uniaxial tension. On the other hand, the glass will contribute indirectly to energy absorption when the bonds between the glass and the PVB are broken. A diagram showing the delamination is presented in Figure 3.5. As seen, an area close to the crack will delaminate as a result of the relative elongation between the glass and PVB. The ”delaminated areas” shown in Figure 3.5 are areas where the cohesive bond between the glass and PVB have torn. No further analysis will be conducted on the results in this thesis, and the interested reader is directed to [19].

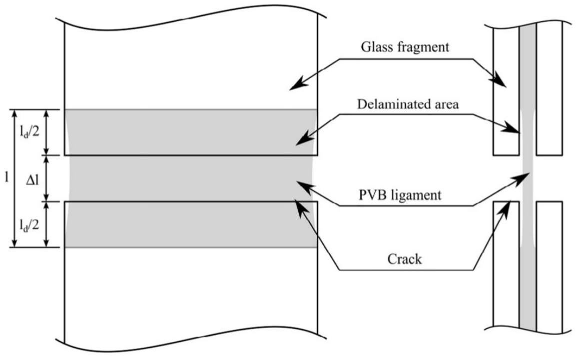

Figure 3.5: Diagram describing the delamination process, adapted from [19]

3.1.5 Rubber

In the SIMLab shock tube rubber strips are used in the clamping of the glass specimens. The rubber clamping is affecting the boundary conditions in the shock tube and thus the results and numerical modelling. A basic understanding of rubber is of importance.

The term rubber is a team applied to any material behaving the mechanical properties similar to the ones found in natural rubber [47]. The most important physical characteristic of the materials is the high degree of deformability when loaded with comparatively low stresses. Due to the non-linear behaviour, Hooke's law does not apply, and a definite Young's modulus may therefore not be defined explicitly for small strains [47]. It has been found that rubbers are highly strain rate sensitive, and Roland et al.[48] tested rubbers at strain rates as high as $1620m/s$ and found that the initial stiffness varies significantly. The rubber used in the clamping of the glass in the SIMLab Shock Tube is a neoprene rubber. Neoprene is known for its chemical stability and its ability to maintain flexible in a wide range of temperatures[47]. In civil engineering, neoprene is often used in bridge supports. The behaviour of neoprene rubber was studied by Salisbury [49], and the behaviour is described as hyper-viscoelastic with a significant strain rate dependency when tested at strain rates ranging from $0.001m/s$ to $2700m/s$.

3.2 Material modelling

3.2.1 Glass material modelling

The glass was in thesis modelled with elastic material properties and a fracture criterion. The elastic material parameters of interest was Youngs' moduls, Poissons number, the material density, fracture strength and the stress intesity factor. As presented in Section 1.2, elastic properties with a fracture may be sufficient when modelling glass [6; 7].

3.2.2 Rubber material modelling

The rubber was in this thesis modelled with elastic material properties. As argued, the rubber is highly strain rate sensitive, but a simplification with elastic properties only may be sufficient for small strains. Additionally the elastic material model drastically decreases the running time of the simulations compared to a more advance model.

3.2.3 Bergström-Boyce

The Bergström-Boyce (BB) model is an advanced material model for describing elastomer-like materials which are non-linear, time-dependent and with a significant strain behaviour. In this thesis the BB-model will be used to describe the PVB when modelled in a tensile test in IMPETUS Afea Solver [42]. The model implemented in IMPETUS consists of two parallel networks, A and B, with different abilities. Network A is a non-linear hyperelastic network which describes the equilibrium response, while network B is purely non-linear viscoelastic which is sensitive to the strain rate. The network used in IMPETUS is illustrated in Figure 3.6 [50].

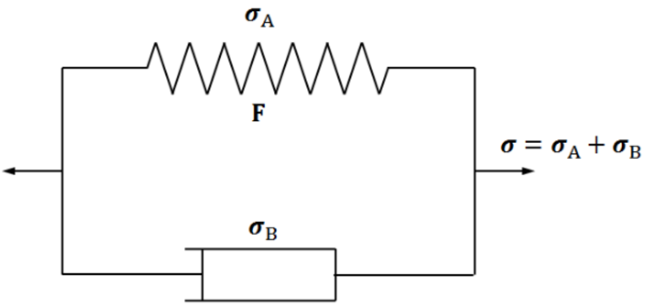

Figure 3.6: Bergström-Boyce model network used in IMPETUS. Figure taken from [42]

The total stress is defined as the sum of the stress in network A and B:

$$\sigma = \sigma_A + \sigma_B \tag{3.1}$$

Network A

The hyperelastic network A is set up with stress and damage parameters as shown:

$$\sigma_A = (1-\eta)\cdot \frac{\mu}{J\overline{\lambda}}\cdot \frac{L^{-1}(\overline{\lambda}/\lambda_L)}{L^{-1}(1/\lambda_L)}\cdot \overline{C}_{dev} + K\cdot ln(J)I \tag{3.2}$$

where μ is the initial shear stiffness, λ_L the locking stretch and K the bulk modulus. L^{-1} is the inverse of of the Langevin function, $J = detF$, $\overline{C} = J^{-2/3}F^tF$ and $\overline{\lambda}$ is defined as the network stretch. The network stretch is calculated as:

$$\overline{\lambda} = \sqrt{\frac{tr\overline{C}}{3}} \tag{3.3}$$

η is a measure of the network damage and grows according to:

$$\dot{\eta} = a_0\cdot\,(\eta_{max} - \eta)\cdot \left(\frac{\overline{\lambda}}{\lambda_L}\right)^{a_1}\cdot \dot{\overline{\lambda}} \tag{3.4}$$

where a_0 and a_1 are a parameter and a exponent for the Mullins damage. η_{max} is the maximum damage.[42]

Network B

For network B, IMPETUS offers two different ways to calculate the relation between the viscous stress and the deviatoric strain rate. Alternative 1 is calculating the effective viscous stress, σ_B^{eff}, by using the relation:

$$\dot{\varepsilon}_{dev} = \dot{\gamma}_0(\overline{\lambda}^v - 1 + \xi)^B\cdot \left(\frac{\sigma_B^{eff}}{\sigma_0 + Q\cdot\,(1 - exp(-C\varepsilon^{eff})}\right)^m\cdot \frac{\sigma_B}{\sqrt{\sigma_B : \sigma_B}} \tag{3.5}$$

where $\dot{\bar{\varepsilon}}_{dev}$ is a time average deviatoric strain rate :

$$\dot{\bar{\varepsilon}}_{dev} = \frac{1}{c_{dec}} \int_0^t \dot{\varepsilon}_{dev} e^{(\tau - t)/c_{dec}} d\tau \tag{3.6}$$

Alternative 2 using the relation [42]:

$$\sigma_B^{eff} = b_0(\overline{\lambda} - 1)^{b_1} \cdot \left(\frac{\dot{\bar{\varepsilon}}_{dev}^{eff}}{\dot{\gamma}_0} \right)^{b_2} \tag{3.7}$$

3.2.4 Modelling of adhesion and delamination

An important feature of laminated glass is as mentioned the adhesive bonding between the glass and PVB. When laminated glass plates are exposed to e.g. a blast load, the bonding strength affects when the glass starts to delaminate and glass fragments lose contact with the interlayer. To model this adhesive bonding layer between glass and PVB, the feature called *MERGE_FAILURE_COHESIVE may be used. During the work of this thesis, the feature was modified to enable a better representation of the delamination phenomenon. To use this command, the surfaces need to be merged by the command *MERGE. With the *MERGE feature, the materials are bonded. As described in the IMPETUS manual [42], the failure is initiated when:

$$\left(\frac{\xi \sigma}{\sigma_{fail}} \right)^2 + \left(\frac{\xi \tau}{\tau_{fail}} \right)^2 \geq 1 \tag{3.8}$$

where ξ is a scale factor accounting the inability to resolve stress concentrations at coarse element grids:

$$\xi = max(1, \sqrt{\Delta / \Delta_{ref}}) \tag{3.9}$$

Δ is the local characteristic element size of the merge interface. The stress unloading from failure is a linear function of the crack opening distance. It is defined such that the consumed energy per unit area of cracking G is:

$$G = \sqrt{\left(\frac{\sigma}{\sigma_{fail}} G_I \right)^2 + \left(\frac{\tau}{\tau_{fail}} G_{II} \right)^2} \tag{3.10}$$

which is calculated by using the relations presented in Section 2.4.3. The main purpose of the *MERGE_FAILURE_COHESIVE feature is to allow for local stretching in the PVB layer after failure in the glass at the crack tip. For this to happen, the connected nodes between the glass and PVB need to be separated, but without splitting the nodes in the PVB layer. This is illustrated in Figure 3.7. It is important that the PVB is modelled with a finer mesh than the glass so that the PVB-elements between the glass elements remains merged

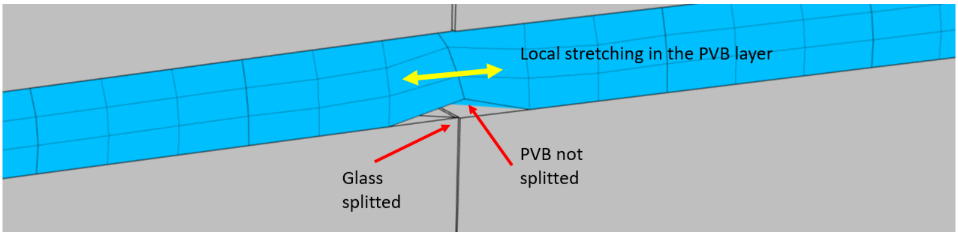

Figure 3.7: Local stretching in the PVB layer when the glass reach its failure criteria. Adapted from [51]

Froli and Lani [45] conducted shear and compression tests of laminated glass plates, and found that the adhesive shear strength is around $\tau_{fail} = 10\text{MPa}$ and the tensile strength lies a place between $\sigma_{fail} = 5 - 10\text{MPa}$.

Chapter 4

Experiments

4.1 Four point bending test

To study the fracture strength and the static behaviour of laminated glass, a four point bending test was conducted on laminated glass specimens. The experiments were done and supervised by the authors, Tore Kristensen from Sintef and PhDc Karoline Osnes in the laboratory at the Department of Structural Engineering at NTNU.

4.1.1 Setup

Three different specimen sizes were tested, large (300×60 mm), medium (200×40 mm) and small (100×20 mm). All three sizes had the same layering, i.e 3.8mm glass - 1.52mm PVB - 3.8mm glass. For each size, 25 specimens were loaded until fracture in both glasses occurred, resulting in total 75 tests.

The test setup is based on the ASTM International standard C1161 for flexural strength on ceramics [52]. The test setup consisted of a support and loading member made of steel, four cylindrical bearings made of steel, a laser measuring the midpoint displacement of the underside of the test specimens. The tests was performed in an Instron 8985 testing machine with a 5 kN load cell. The bearings were located at each quarter point of the test length and were fastened with elastic rubber bands. Though the test standard suggests the thickness of the steel bearings to be 1.5 times the thickness of the glass specimen, the diameter of the bearings used in this experiment was 6 mm. The general setup is illustrated in Figure 4.1. As the lengths of the specimens changed from 100 mm to 300 mm, the dimensions of the setup varied as well, while maintaining the same ratios as shown. An issue with four point bending tests performed on glass specimens is to apply the same load to both loading cylinders. To make sure that the loading cylinders hit the glass horizontally, a fixture securing free rotation was placed together with the loading members on the glass specimen before the loading started. The fixture and loading members had caused deflection before loading. The weight was added to the results measured by the load cell and the laser making the deflection at the start of the tests, non-zero.

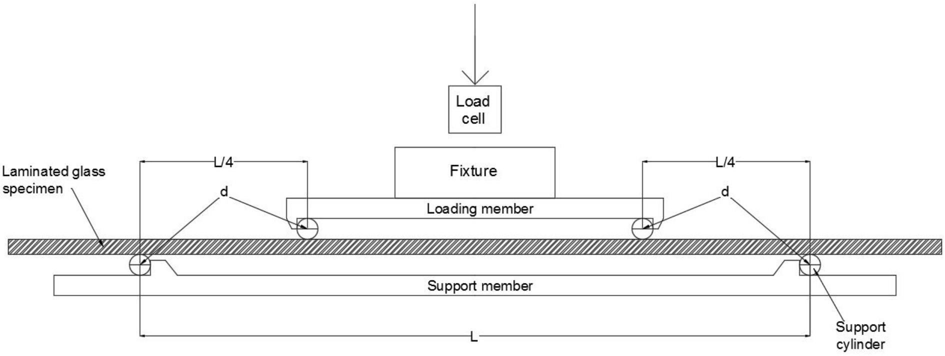

Figure 4.1: Setup of the four point bending test

The weight of the fixture and loading members were measured and calculated as forces acting on the glass additionally to the load cell. The force from the fixture and loading member is denoted F_0, and the setup data for the different sizes are presented in Table 4.1

Table 4.1: Data for the different setups in the experiments

Large			Medium			Small		
$L[mm]$	$d[mm]$	$F_0[N]$	$L[mm]$	$d[mm]$	$F_0[N]$	$L[mm]$	$d[mm]$	$F_0[N]$
280	6	60.31	180	6	35.63	80	6	20.87

The measured initial deformation caused by the weight of the fixture was small and thus neglected in the results. As mentioned in Section 3.1.1, tensile and compression strength of glass has proven to be strain rate sensitive [43]. The different glass sizes was therefore tested at the same strain rate, and different loading speeds should was applied. According to ATSM C1161, the strain rate should be of order $1.0 \times 10^{-4} s^{-1}$. Loading speeds were calculated for the three specimens by using the following equation [52]:

$$\dot{\varepsilon} = \frac{48hs}{11L^2} \tag{4.1}$$

Where $\dot{\varepsilon}$ is the strain rate, h is the specimen thickness, s is the loading speed, and L is the testing span. The ASTM C1161 standard [52] is made for monolithic specimens, and not for composites. However, the standard was used as a guideline for calculating the loading speeds for the different sizes. With the assumption that moment of inertia of laminated glass lies close to the lower limit presented in Section 2.1.1, the thickness h becomes the thickness of one of the glass layers and not the specimen. The different loading speeds are presented in Table 4.2

Table 4.2: Table showing loading speeds for the different specimens

	Large	Medium	Small
s [mm/min]	8.6	3.5	0.7

To validate the dimensions given by the manufacturer, the tested glass specimens were measured with a micrometre. The key results for the measurements are presented in Table 4.3 and the raw measurement data are found in Tables A.1, A.2 and A.3 in Appendix A. The specimens were also checked for cracks and flaws visible to the naked eye. Of the 75 specimens tested only 8 had minor imperfections, and the overall quality of the glass was deemed adequate. The specimens was cut from a glass plate and then the edges were treated with a rough polish.

Table 4.3: Key dimensions of the specimens tested in the four-point bending test.

	Large		Medium		Small	
[mm]	d	w	d	w	d	w
Max	9,180	59,66	9,180	39,67	9,186	19,96
Min	9,047	59,14	9,007	39,39	9,094	19,60
Mean	9,131	59,50	9,125	39,52	9,139	19,70

4.1.2 Results

Force Displacement

The loading force and the displacement at mid point were recorded during the tests. The raw data was imported to MatLab, and the force was plotted as a function of the deflection. As described in the previous section, a total of 75 datasets were imported, 25 of each sample size.The resulting curves are shown in Figure 4.2. As seen in the figure the loading capacities vary significantly within the same sizes, showing the stochastic nature of the fracture strength of glass. As pointed out, the fixture and the loading member were placed on the glass prior to the loading causing the load to start at F_0 in the plot. For visual reasons, a point $[0, 0]$ was added to the graph sets for the curves to start in origin. The contribution from the PVB layer to the stiffness of the beam is assumed to be close to negligible in comparison to the stiffness of the glass, as the initial stiffness of PVB at low strain rates is expected to be several orders of magnitude lower than for glass. Additionally, the PVB layer is placed in the neutral axis of the specimen making the contribution to the moment of inertia, Equation 2.2, small. Thus, it may be assumed that the fracture of the laminated glass beams occurs approximately when the fracture strength of the glass is reached.

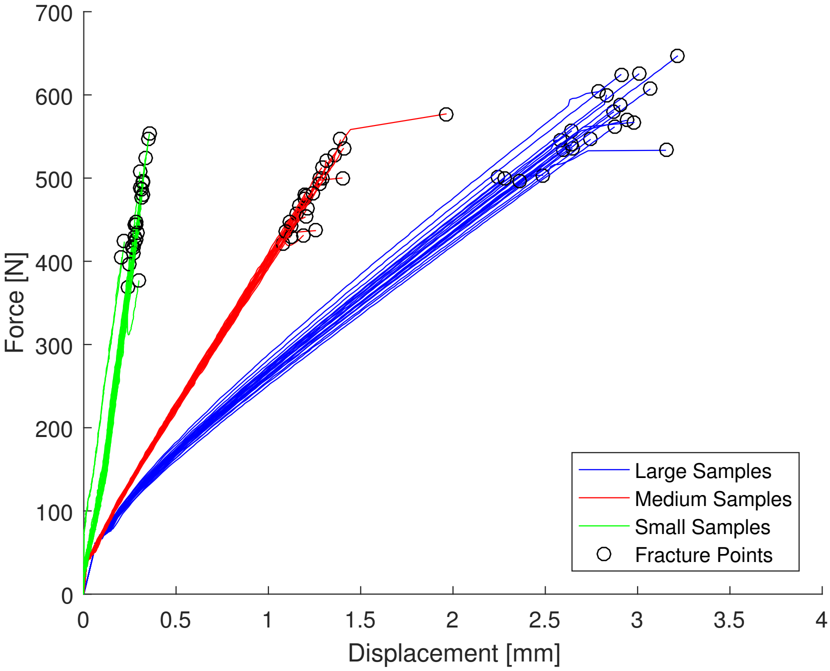

Figure 4.2: Raw data from the four-point bending experiments

As seen in Figure 4.2, the laminated glass responds linearly elastic. This is because the glass dominates the behaviour before fracture. As seen in at the start of the force-displacement curves, the initial behaviour differs from the response after the fixture have stabilised. Most of the data showed similar behaviour when subjected to loading, except a medium and a large sample. The reasons for the mentioned inconsistencies of the two samples was most likely caused by the laser missing the target as the glass fractures and thus increasing the displacement without a corresponding increase of load. Pictures of the fractured specimens are shown in Figures A.1, A.2 and A.3 in Appendix A

Moment of Inertia, Young's Modulus and Fracture Strength

Based on the recorded data from the experiments, the fracture strength of the samples was calculated. Beam theory was assumed valid and the I_{upper} and I_{lower} were determined with Equations (2.3) and (2.4). From the calculated moments of inertia, beam theory presented in Equation (2.13) was used to find the fracture stress in the glass for each specimen. The moments of inertia for the different samples are listed in Table 4.4

Table 4.4: Calculated lower and upper boundaries of the moment of inertia for the different glass samples, all values in mm^4

Large		Medium		Small	
I_{upper}	I_{lower}	I_{upper}	I_{lower}	I_{upper}	I_{lower}
3.757e+03	5.441+02	2.490e+03	3.614e+02	1.247e+03	1.801e+02

The upper-limit moments of inertia are found to be seven times higher than the lower limit, making the glass seven times stiffer and resulting in an unrealistically low critical strength for the upper limit. With the calculated inertia, the mean value, the maximum and the minimum fracture stress values were estimated. The results are listed in Table 4.5.

Table 4.5: Table showing the fracture strengths calculated with the different stiffnesses based on the results from the experiment. Values in MPa

	Large		Medium		Small	
	σ_{upper}	σ_{lower}	σ_{upper}	σ_{lower}	σ_{upper}	σ_{lower}
Mean	23.66	163.34	19.82	136.59	16.58	114.76
Max	27.52	190.00	23.81	164.06	20.26	140.24
Min	20.74	143.21	17.37	119.71	13.52	93.57

As seen in Table 4.5 the difference between the lower and the upper boundary limit of the fracture strength is significant. As argued before, the behaviour of laminated glass is expected to be somewhere in between the limits, closest to the lower boundary [24; 25]. The fracture strength used for the modelling of float glass is varying. From a Monte Carlo simulation of 5000 plates, Yankelevsky [12] found the average tensile stress at fracture to be 47.47MPa, while Larcher [6] and Hooper [53] argues that the fracture strength is 84MPa and 80MPa respectively. It is emphasised that the strength of glass is expected to increase with the decrease in sample size due to the effect of microcracks. As presented in Section 3.1.1, the failure of glass is dependent on the locations and sizes of the micro cracks. A smaller test specimen will naturally have fewer microcracks than a larger sample, and thus the probability of finding cracks of critical size is reduced. Due to the strong correlation of specimen size and fracture strength, a direct comparison between the results found in the experiments and the values found in [12; 6; 53] cannot be done.

The difference in fracture strengths calculated from the experiments contradicts what was expected. The small samples showed a lower strength than the large samples. The mean fracture strength for size small was 29% lower than the large samples. The fracture strength of the medium samples was found to lie between the large and small samples. A reason for this contradiction may be the influence of edge cracks in the samples, generally influences the smaller samples to a greater extent than for the larger ones. The edges constitute a bigger percentage of the smaller samples than the larger ones.

The Youngs' modulus was calculated with Equation 2.15 from the Section 2.1.1. The Young's moduli were estimated based on the middle part of the force-displacements curve. The results are presented in Table 4.6

Table 4.6: Calculated Youngs' modulus from the experimental data. All values in MPa

	Large		Medium		Small	
	E_{upper}	E_{lower}	E_{upper}	E_{lower}	E_{upper}	E_{lower}
Mean	17 065	117 830	12 614	86 925	7 906	54 737
Max	19 110	131 960	13 072	90 083	9 887	68 454
Min	14 908	102 940	12 188	83 992	6 662	46 127

The uncertainty of the total stiffness of the laminated glass affects the calculated Youngs' Moduli in the same manner as for the σ_{cr}, as both equations are dependent on I. According to findings in literature, [33; 54], the expected Youngs' modulus for annealed glass is expected to be between 70 and 74 GPa. As seen in Table 4.6 the findings from the experiments are not in accordance with the expected value. This difference supports the belief that the actual inertia is different from the two proposed calculated inertias, however closer to the lower limit. An additional curiosity regarding the calculated Youngs' moduli is that the moduli for the small samples lie below the expected value, while for the large and medium samples the moduli are higher than anticipated. This inconsistency questions whether the moment of inertia can be the only cause for the experienced discrepancies. Another possible explanation for the discrepancy may be the validity of Euler-Bernoulli beam theory. For the tested laminated glass specimens, the assumption of linear stress distribution in the glass may not be valid. The dimensions of the small sample may be unfit for the assumptions made in the derivations in beam theory, i.e the ratio between height and length may be too high. In addition, the ratio between the height and the length of the specimens may be too high.

Statistical Treatment of Experimental Results

The fracture strengths were rounded up to the nearest 5 MPa for a statistical representation of the results. Figure 4.3 shows the distribution of fracture strengths for the large samples. $f(\sigma)$ is the probability. The spread in fracture strengths emphasises the stochastic nature of glass.

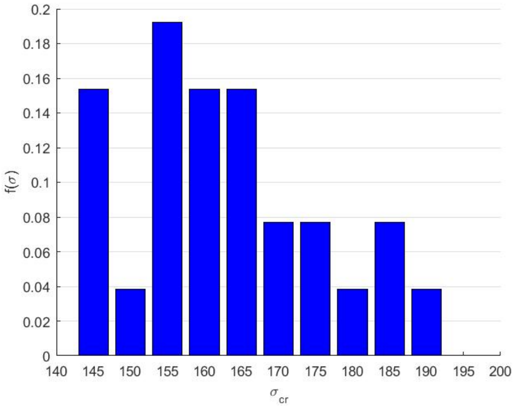

Figure 4.3: Bar plot of the large samples, $f(\sigma)$ is the probability

As seen in Figure 4.3 the results from the experiments vary significantly. Due to the high variance, a Weibull analysis was conducted to calculate the Weibull parameters m and σ_0, see Section 2.5.1 for the theoretical background. The procedure for the Weibull analysis is adapted from ASTM C1239 [55] and was applied separately for the different specimen sizes.

First, the fracture strength for each sample was calculated and then ranked in ascending order. The probability of failure in each test was then calculated with the following formula:

$$P_f(\sigma_i) = \frac{i - 0.5}{N} \tag{4.2}$$

where $P_f(\sigma)$ is the probability for the given failure stress σ_i and N is the number of the specimens in the test series. The Weibull parameters were found using linear regression on a scatter plot with $ln(\sigma_i)$ on the x-axis and $ln(ln(\frac{1}{1-P_f}))$ on the y-axis. For the small and medium samples, all 25 tests were used in the series while for the large samples the results from the first and second test were neglected. The first two tests of the large samples showed signs of an error in the fixture mounted to the load cell. As pointed out in the standard a minimum of 30 specimens is recommended for each test series to achieve a good approximation of the fracture strength. The lack of specimens in this experiment may therefore affect the accuracy of the results and increase the error. In the Weibull analysis, the σ_{cr} corresponding to the lower boundary moment of inertia were used, σ_{cr}^{lower}. As this is the lower boundary limit, the results from the Weibull analysis will be non-conservative. The results are shown in Table 4.7

Table 4.7: Table containing the results from the Weibull analysis, stresses in MPa

	Large	Medium	Small	Average
$\hat{m}$	15.48	14.03	10.82	13.44
$\hat{\sigma_0}$	157.43	131.11	111.49	133.34

As seen in the results both parameters vary with different sample sizes. The correlation between experiments and the calibrated values are acceptable while the discrepancies between the sample sizes are worth noting.

A graphic display of the regression done with the curve fitting tool for the large samples is presented in Figure 4.4. Similar figures for the small and medium samples are found in Figures B.1 and B.2 in Appendix B.

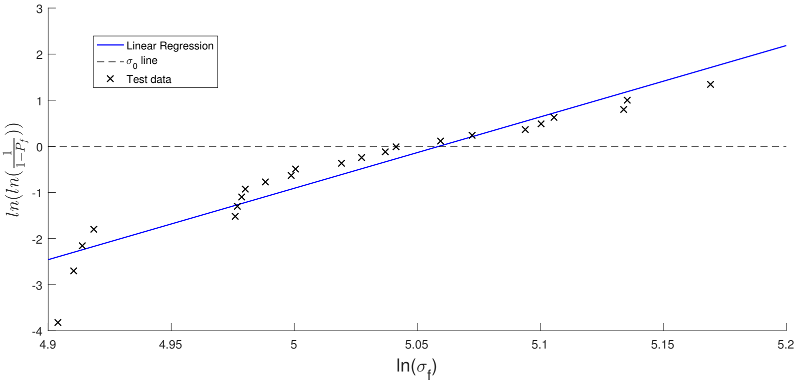

Figure 4.4: Linear regression done in accordance with ASTM C1239 [55], large samples

In addition to the linear regression, the fitted probability density and the cumulative cumulative distribution function was compared to the experimental results. The results for the large samples are presented in Figure 4.5 while the figures from the medium and small samples are found in the Appendix B.

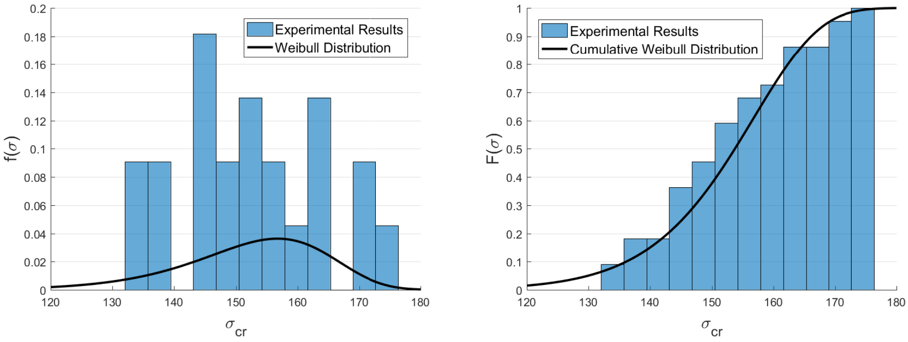

(a) Probability density function **(b)** Cumulative probability density function

Figure 4.5: Weibull distributions, large samples

As mentioned, the larger samples had a greater fracture strength than the smaller ones, and the results may be caused by the influence of edge treatment. To study the edge effect of the specimens, a second round of experiments were conducted with the same setup. The second series of tests consisted of 24 small samples, nine medium samples and ten large specimens. The force-displacement curves from the second round of experiments are presented in Figure 4.6. The edges of samples tested in the first round of experiments were roughly polished after they were cut out. The samples tested in the second round of experiments were not treated, and the edges were noticeably sharper. It was seen on the specimens after the experiments that the cracks had initiated on the edges of the specimen, which was the same as for the specimens with polished edges tested in the first round.

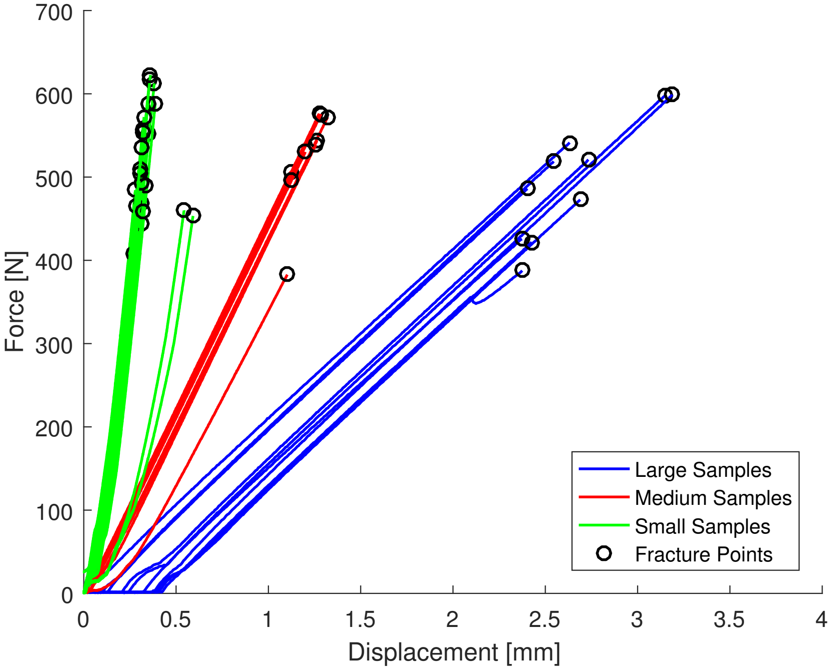

Figure 4.6: Force displacement curves from the second round of experiments

As seen in the force-displacement plot i Figure 4.6, the results from the second round did not differ significantly from the first experiment shown in Figure 4.2, and due to time limitations no further analysis of the results were conducted.

4.2 Blast testing

Blast tests on laminated and monolithic glass were conducted in the SIMLab shock tube, which is a good way to test glass panes in a controlled and safe environment. The shock tube generates blast waves similar to the ones created during an explosion, and the experiments are easy to repeat. The blast waves creates a uniform pressure on one side of the test specimen. In this section, the setup and the experimental shock tube results are presented. There will also be given a short introduction to the shock tube at SIMlab.

4.2.1 The SIMLab shock tube

The contents in this subsection is mainly adapted from [28], where the interested reader may find additional information on the topic. The SIMLab shock tube consists of the driver section, the firing section, the driven section and the dump tank. The driver is the section where the desired pressure is built up, and the firing section consists of two pressure chambers that are separated by membranes. When the pressure in the driver section reaches the total capacity of the membranes, they rupture. The sudden increase in the pressure, generates a shock wave propagating through the driven section up to the end. In the SIMLab shock tube, pressure sensors are installed along the driven section and right before the fixed test specimen. Outside of the tank, high-speed cameras are mounted to capture the behaviour of in the test specimen when subjected to the blast load. Figure 4.7 shows the setup of the SIMLab shock tube. The lasers depicted in the Figure were not used.

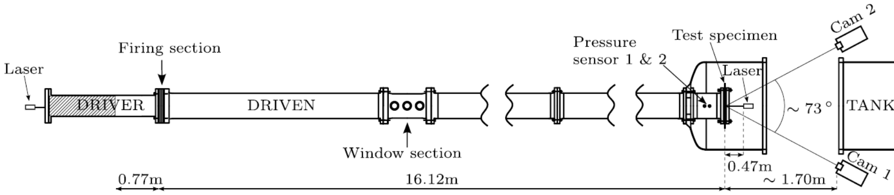

Figure 4.7: Setup of the shock tube at SIMLab NTNU, figure adapted from [28]

4.2.2 Setup

Glass panes with the dimensions of 400 mm × 400 mm were fastened and clamped at the end of the driver. To fasten the laminated glass plates, a steel frame with an interlayer of rubber was utilised. For the monolithic tests, a lighter aluminium frame was used. The frame was bolted to the driven end such that the glass pane was fastened with a rubber layer on each side. Due to the higher pressures in the laminated glass tests, the increased stiffness of the steel frame was desired to ensure the relative displacement of the frame to be as low as possible. To check the effect of the fastening torque, two different torques were used, 100Nm and 150Nm. As seen in Figure 4.8 there are 24 holes for bolts, but for all cases 12 bolts were used. The rubber strips prevented the metal touching the glass and bolt stoppers ensured that the glass was not fractured by the clamping torque.

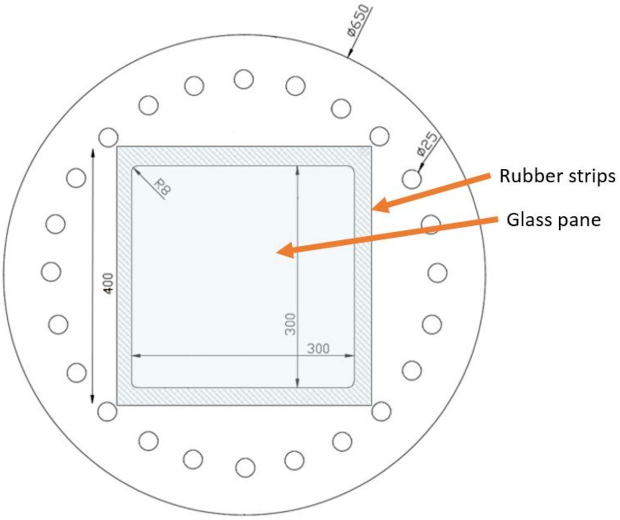

Figure 4.8: End of the driven section, where the test specimen is placed

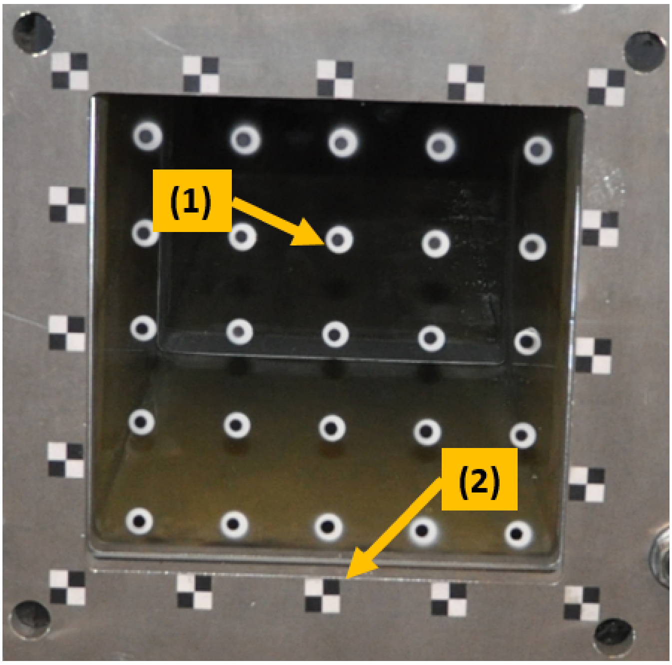

Figure 4.9: Point-tracking dots on the glass **(1)** and point-tracking stickers on the frame **(2)** for the DIC-analysis

For monitoring, two high-speed cameras were utilised. The camera type was Phantom v1610 with a recording rate of 24 000 frames per second. The cameras were installed to capture the response in the glass during the experiments and the images were used in a DIC-analysis of the glass. For the high-speed cameras to measure the displacement at different locations at the glass panes during the tests, 25 point-tracking dots were spread out on the glass. The dots were made with white painting as a first layer, and a black marker for smaller dots inside them. To measure the relative displacement of the frame, white and black stickers were glued to the frame. The glass and frame setup are showed in Figure 4.9. The 3D-DIC model was then calibrated with a 80 tall cylinder with a checkerboard pattern. The squares had the dimensions 6.527×6.527 mm. According to Aune et. al [28], this implies a maximum error in the DIC analysis of 0.07 mm compared the real plate displacement.

The pressure was measured in the sensors along the tube. From the two sensors closest to the test specimen, Friedlander fitting of the reflected pressure was found using a MATLAB script made by PhDc Karoline Osnes utilising the Friedlander equation presented in Section 2.2. The peak reflected pressure was estimated by extrapolating the Friedlander curve to the time of impact and the time of the positive phase as shown in Figure 2.4. The parameters needed to describe the pressure load in a numerical simulation, P_r, P_a, b and t_+ were found using curve fitting and iteration as described in Section 2.2. For the experiments where the monolithic glass fractured, a linear extrapolation curve was used instead. The peak reflected pressure is dependent on a surface to reflect on, and when the glass breaks, this surface disappears.

Test specimens

The blast experiments were conducted using 3.8 mm single layered glass pane for the float glass tests, and the laminated glass was made of one PVB-layer laminated between two 3.8 mm glass panes. All test specimens were measured using a micrometre at eight different locations around the edge to ensure reliable results. The measured mean values for the different tests are presented in Table 4.8 and Table 4.9. The overall mean value for the float glass panes was measured to 3.80mm and the laminated glass 9.12mm. This gave a laminated glass setup as seen in Figure 4.10. All glass panes were also thoroughly checked for flaws and imperfections before tested, and the specimens showed a sufficient quality all over.

Table 4.8: Measured mean value of the float glass specimens

Test	t [mm]
FG 01	3.82
FG 02	3.81
FG 03	3.79
FG 04	3.81
FG 05	3.80
FG 06	3.81

Table 4.9: Measured mean value of the laminated glass specimens

Test	t [mm]
LG 01	9.13
LG 02	9.13
LG 03	9.10
LG 04	9.12
LG 05	9.13
LG 06	9.12

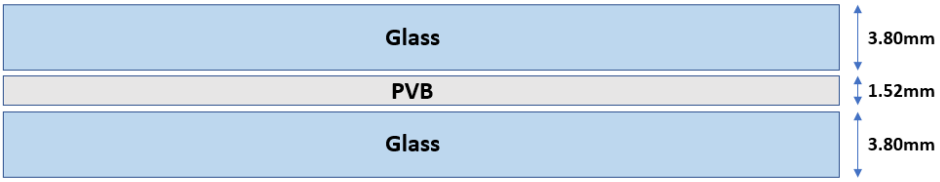

Figure 4.10: Cross section of the laminated glass panes tested

4.2.3 Results

In this section, the experimental results conducted on float glass and laminated glass will be presented and analysed. A summary of the key results of the tests are shown in Table C.1 in Appendix C.

Float Glass

The tests conducted on the monolithic float glass were conducted over two days. The first three glasses, denoted FG-01, FG-02 and FG-03, were tested on 10th of March 2017 with the temperature being $20.7°C$ and with a humidity of 25%, while the rest of the glass panes were tested 13th of March 2017 at $20.8°C$ and 31.3% humidity. The first three glasses were tested with the desired driving pressure of 1.5 bar. The fastening torque were 150Nm for all three glass panes. Based on previous experiments conducted in the shock tube, [11], the authors expected the glass panes to withstand the pressure in the tests, but all the glass panes failed. The resulting firing pressures, P_f and calculated reflected pressures, P_r are listed in Table 4.10 together with the deflection of the mid-point at fracture, ΔM. As seen in Figure 4.11 the initiation of the cracks were different in all three tests. The deflections were extracted from the DIC-analysis at the time where the first visual crack appeared in the images.

Table 4.10: Pressures recorded during the tests of FG-01 to FG-03.

Test	Pane	P_f [bar]	P_r [bar]	ΔM [mm]	Fracture initiaton
FG-01	01	1.526	0.637	3.594	Close to the middle
FG-02	02	1.563	0.660	5.519	At the edge
FG-03	03	1.285	0.516	5.132	At the edge

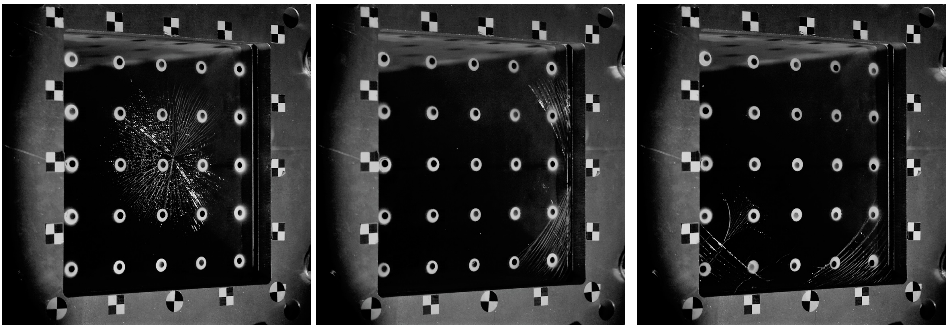
(a) FG 01 **(b)** FG 02 **(c)** FG 03

Figure 4.11: Crack initiation on the monolithic glass panes tested 10/3-17

As none of the panes stayed intact during the first series of blast experiments, Friedlander fits would not give accurate results. When the glass fractures, the shock wave does not have a surface to reflect on and this leads to an unrealistic P_r. For the cases where the glass fractured, the P_r was found by linear interpolation from the fracture pressure. The reflected pressures tabulated in Table 4.10 are found by linear interpolation. To enable modelling of the glass panes that fractured, a function describing the pressure load was derived. The pressure load was defined with the following expression:

$$P(t) = P_r - \frac{P_r - P_f}{t_f} \cdot t \tag{4.3}$$

where P_r is the reflected pressure, P_f is the fracture pressure and t_f is the time at fracture.

The midpoint deflection in the three glass panes was, as seen in Table 4.10, varying from 3.594 mm to 5.519 mm in the three experiments. The glass panes with the initial fracture on the edges fractured at a higher mid-point deflection than the pane with crack initiation in the middle. To evaluate the severeness of the fracture, the velocity of the fragments after impact was calculated. For the calculation to be possible, the DIC program needed to be able to track a subset on a fragment with both cameras after the shattering of the glass pane. For the glasses FG-01, FG-02 and FG-03 the subset in the middle remained more or less intact for the DIC analysis to track the fragments, and therefore this subset was used for the velocity calculations for all three panes. The resulting fragment velocities were estimated to be 23.441 m/s, 16.516 m/s and 12.688 m/s respectively. The velocities calculated were average velocities of the mid point subset, and not the maximum velocity.

Figure 4.12 and 4.13 shows the fracture propagation in test FG-03. $t = 0$ ms is defined as when the initial cracks appear in the pane.

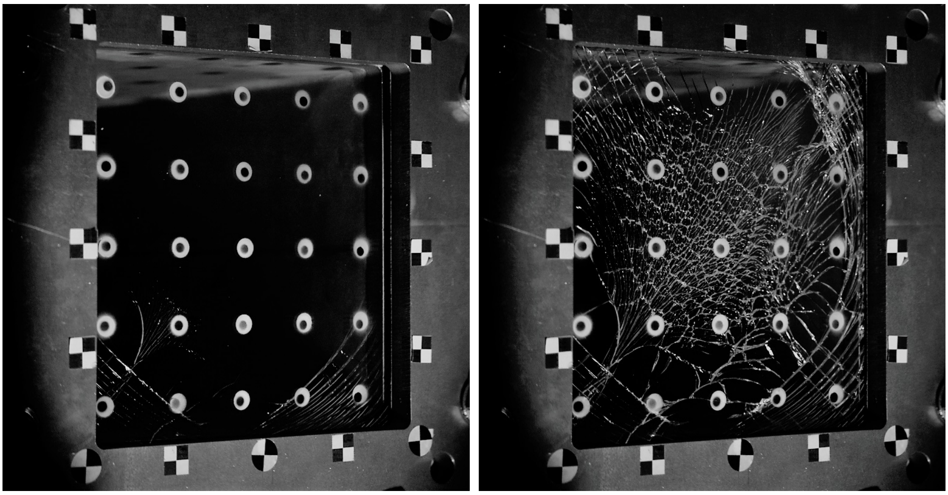

(a) t=0.00 ms

(b) t=0.16 ms

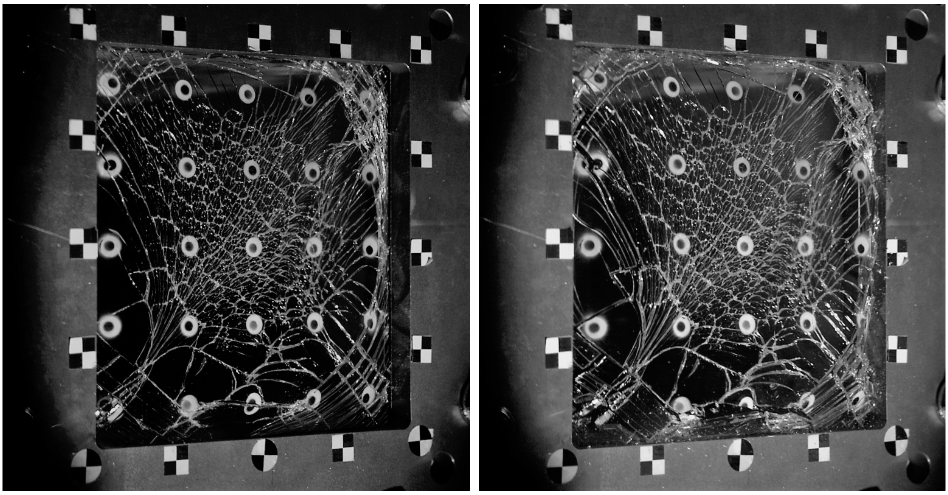

(c) t=2.29 ms

(d) t=3.91ms

Figure 4.12: The failure propagation of the glass pane FG 03

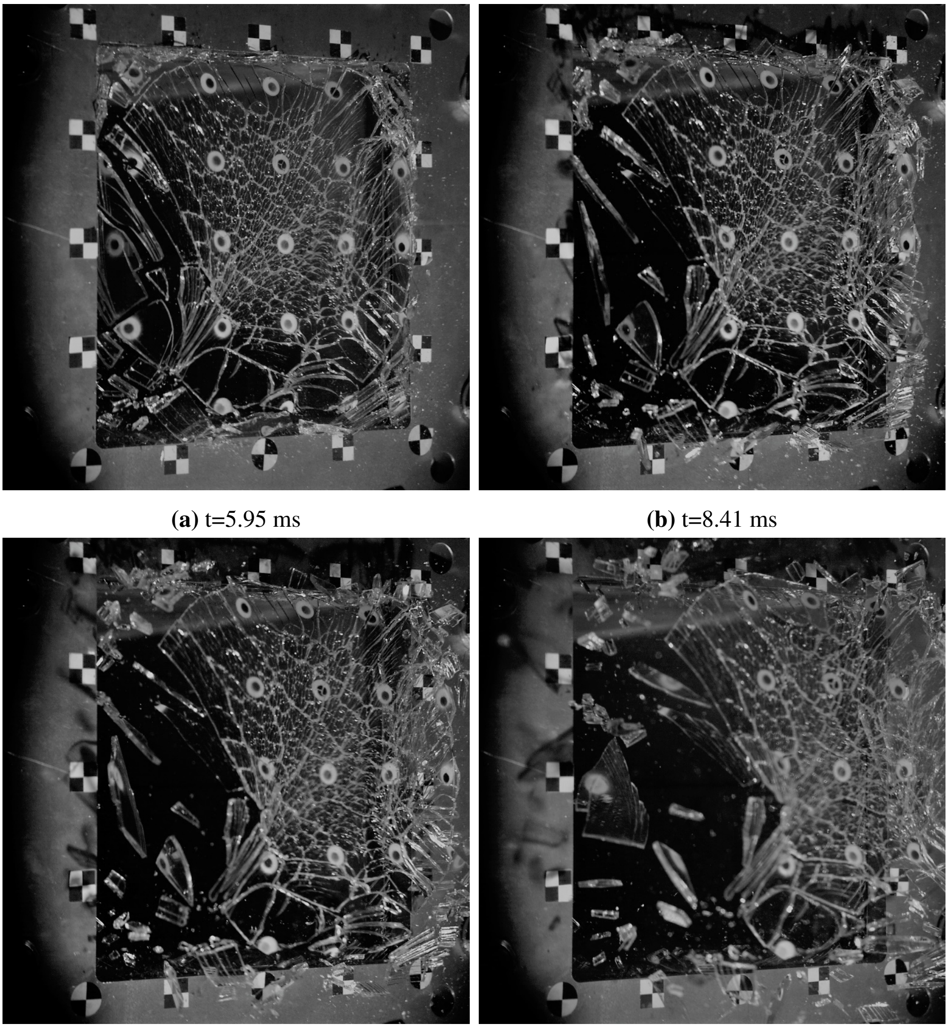

(a) t=5.95 ms (b) t=8.41 ms

(c) t=10.03 ms (d) t=13.67ms

Figure 4.13: The failure propagation of the glass pane FG 03

To evaluate the shape of the glasses at fracture initiation, a surface plot was made. Figure 4.14 shows the displacement of glass FG-01 and FG-02 in 3D at the time of fracture. The colour bar in both plots is set to the same limits for an easier comparison. As also stated in Table 4.10, the displacement of FG-01 is significantly lower than FG-02. This is due to the crack initiation in the middle of the glass pane in test FG-01 and the initiation in the edge in test FG-02. If the critical microcrack is located in the centre of the specimen, the fracture will happen at an earlier point than if the critical microcrack is in the edge due to stress concentrations in the middle.

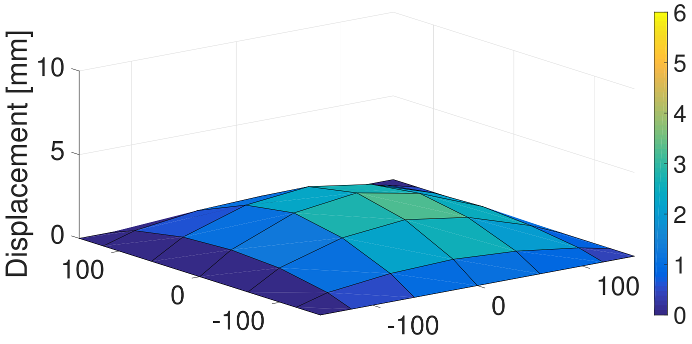

(**a**) FG-01

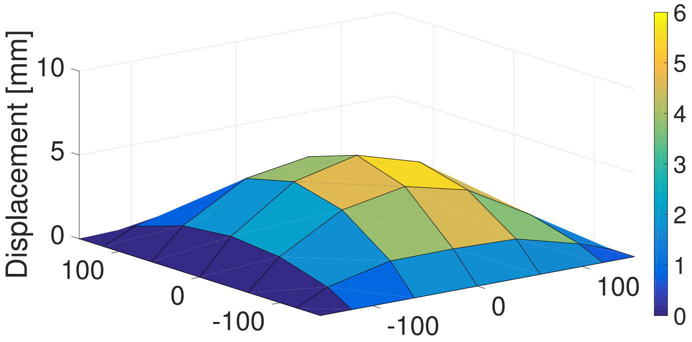

(**b**) FG-02

Figure 4.14: Glass displacement at the time of fracture for FG-01 and FG-02

Rest of the float glasses were tested 13th of March 2017. Four blast experiments were conducted on three panes, FG-04, FG-05 and FG-06. For the glass panes tested in this series, the fastening torque was reduced to 100 Nm. This was to check if the boundary conditions may have affected the experiments conducted in the previous series. The first test was run with the same desired driver pressure as for the first three experiments, 1.5 bar, and this caused the glass to fail. The fracture was initiated in at the edge of the glass. The second experiment, FG-05-1 was run with the same conditions as the previous, but this time the glass refrained from fracturing. Glass pane 05 was then tested again with an increased desired driver pressure, 2.1 bar, which resulted in a fracture with initiation in the lower edge. This test is denoted FG-05-2. Before the second test, the glass was checked for cracks, and none were found. Though no cracks were visible to the naked eye, micro cracks may have grown or formed in the glass pane during the first experiment. Thus the use of the same pane in several tests is not recommended. Experiment FG-06 was run with the desired driver pressure of 1.5 as for the first two tests and fractured at the edge of the pane. The reflected pressures recorded during the experiments conducted March 13th are presented with the maximum displacements in Table 4.11. In the case of FG-05-01, the

ΔM is the maximum midpoint deflection of the glass, since it did not fracture. In Figure 4.15, the crack initiation in the fractured glasses are shown.

Table 4.11: Pressures recorded during experiments FG-04 to FG-06

Test	Pane	$P_f[bar]$	P_r [bar]	ΔM $[mm]$	Fracture initiation
FG-04	04	1.599	0.655	5.676	At the edge
FG-05-1	05	1.569	0.625	5.446	No fracture
FG-05-2	05	2.057	0.734	5.966	At the edge
FG-06	06	1.322	0.530	4.644	At the edge

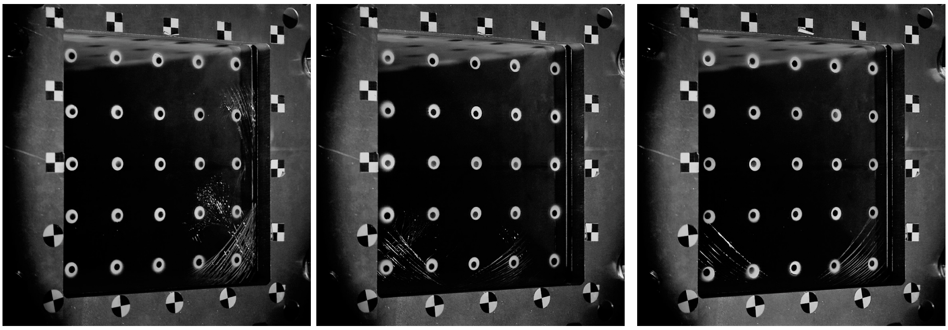

(a) FG-04 **(b)** FG-05-02 **(c)** FG-06

Figure 4.15: Crack initiation on the monolithic glasses tested 13/3-17

As for the first test series, the reflected pressures in the cases where the glass pane failed was found with linear interpolation from the fracture point. From the results, it may be seen that the variance in the mid-point deflection at fracture, or at maximum, is lower than in the first three experiments. The lowest maximum displacement was 4.644mm, and the largest was 5.966mm. The maximum and minimum reflected pressures, P_r, coincides with the extremes in displacement. Compared to the tests ran in the previous series, the deflections are in the same order of magnitude. This may signify that the fastening torque did not affect the results significantly. The bolt stoppers used in the clamping of the plate may decrease the effect of the fastening torque.

From thin plate theory, it is known that the highest effective stress in a thin plate subjected to uniform pressure is in the centre, and thus the fracture should most likely happen there. As seen in the results, this is not the case for these experiments. This may be due to the distribution of microcracks in the glass. As described in Section 2.4, microcracks are the reason for failure in brittle materials. The authors suspect that the a large microcrack in glass pane LG-01 was close to the centre and due to the stress concentration in the middle, the failure happened at a lower midpoint deflection than the other samples. Glass panes with large micro cracks in the centre of the pane will fail at a lower displacement than glass panes with large cracks in the perimeter when subjected to loading as in this experiment. By studying the image with the first crack from test FG-02, it may look like the crack is propagating from within where the glass is clamped. See Figure 4.16. Several of the glass panes investigated showed the same tendency. Of the float glass panes tested, three of the glass panes had the failing crack initiated in the middle of the lower boundary of the pane. This may be a coincidence and be due to large occurring microcracks in that area, or it may signify that the boundary conditions are not hundred percent uniform around the panes.

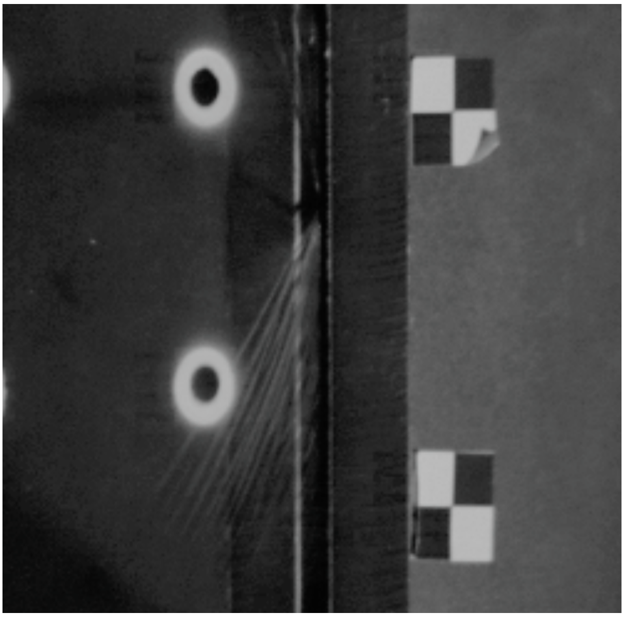

Figure 4.16: Crack propagation from within the clamped zone of glass FG-02

The fragment velocities were calculated for the tests in this series in the same manner as for the previous serie. The resulting velocities were 15.291m/s, 19.142m/s and 13.604m/s for tests FG-04, FG-05-2 and FG-06 respectively. The fragment velocity in test FG-05-02 was slightly higher than the other two, and the authors suspect this to be a result of the increased reflected pressure. This being said, the fragment velocity in FG-01 is higher than the velocity in FG-05-02 even though P_r is lower. The difference in the results are caused by the location of the fracture initiation. When the glass pane fractures at the edges the whole pane accelerates at approximately the same rate. When the fracture is initiated in the middle, the fragments accelerates at a higher rate than the rest of the glass pane resulting higher velocity. The fracture of glass panes FG-01 and FG-05-2 are shown in Figure 4.17. The difference in shape and fracture pattern may cause the different fragment velocities

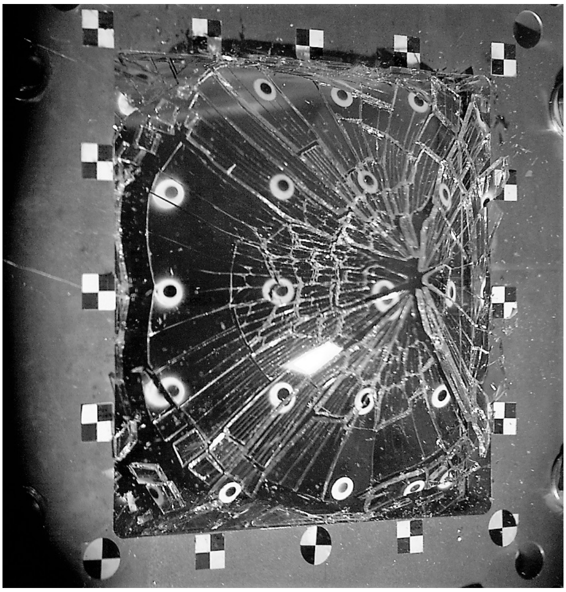

(a) FG-01

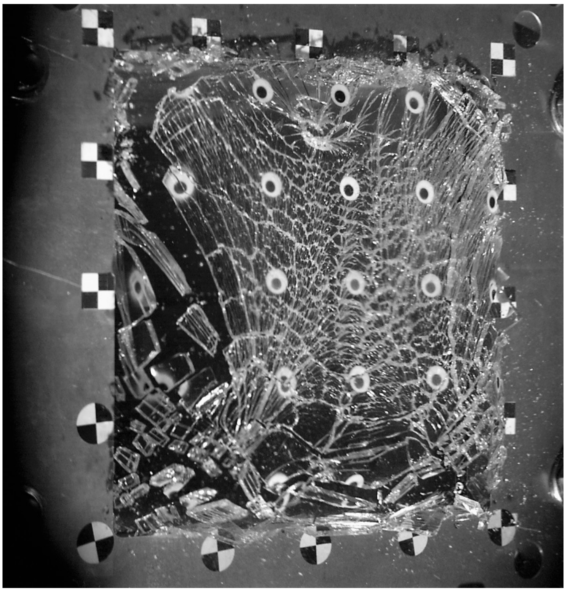

(b) FG-05-02

Figure 4.17: Failure comparison between FG-01 and FG-05-2

As a control of the boundary conditions, a DIC-analysis of the frame was performed for the test with the highest driver pressure, FG-05-02. By extracting the DIC data from the point-tracking stickers on the frame, a 3D plot of the frame at three different times was made, shown in Figure 4.18. The times of the plots are defined as the time before the blast hits the glass at $t = 0.0$ ms, the maximum displacement of the frame at $t = 4.5$ ms and an intermediary time at $t = 3.625$ ms. As seen in the figure the displacement is small, and the authors deemed them as negligible in comparison to the displacement of the panes. As earlier mentioned, the error in the 3D DIC analysis may be up to 0.07 mm, and thus the results have to be interpreted with caution. Figure 4.18 is therefore a more qualitative than a quantitative representation of the behaviour of the frame during the blast. The shape of the displaced frame matches the expected response. As seen in Figure 4.8 the distance from the bolts to the glass longer on the sides of the frame than in the corners. So a stiffer response in the corners was expected.

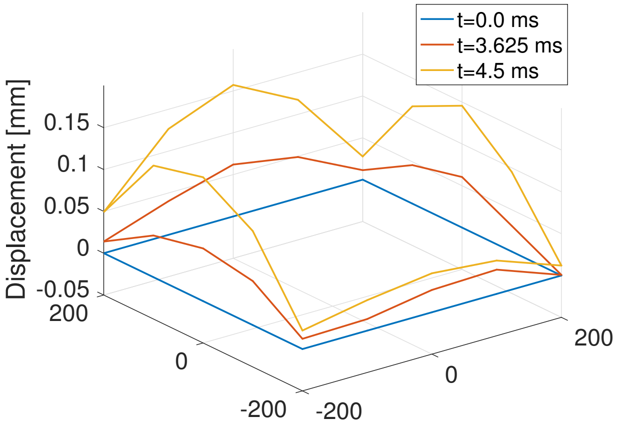

Figure 4.18: DIC analysis of the frame at three different times with use of FG-05-02

Laminated Glass

As for the monolithic glasses, the experiments conducted on the laminated glasses were spread over the same two days with the same conditions. The first day with experiments three tests were run on the same specimen, denoted LG-01. The laminated glass pane did not fracture during the two first experiments, but fractured during the third. The driving pressure was increased from experiment to experiment and this was done to gain an initial impression of the capacity of the laminated glass. The desired firing pressures for the different experiments were 6.7, 7.7 and 8.6 bar for the respective experiments. The Friedlander parameters were calculated with the MATLAB script used for the float glass panes and the deflections were found with DIC analysis. Unfortunately, the membranes in the driver failed prematurely in test LG-01-3 causing the blast to go off before the recording had started. As a result, there were no pressure recordings or images taken during this experiment. Between the tests, the pictures of the glass panes were examined to check for damage inflicted during the previous trials, but none were found. The pressure data along with the maximum midpoint deflection are listed in Table 4.12. As mentioned, the aluminum frame used in the clamping of the float glass panes was replaced with a steel frame. For the three tests run in this series the fastening torque was 150Nm.

Table 4.12: Pressure data from the tests LG-01-1 to LG-01-3

Test	Pane	$P_f [bar]$	P_r [bar]	ΔM $[mm]$	Fracture initiation
LG-01-1	01	6.317	1.697	3.695	No fracture
LG-01-2	01	7.669	2.014	4.793	No fracture
LG-01-3	01	8.142	No data	No data	No data [1]

The parameters of the Friedlander curve fit for the experiments conducted during the first series are tabulated in Table 4.13:

Table 4.13: Friedlander parameters for blasts experiments on laminated glass panes

Experiment	P_r [bar]	t_+ [ms]	b [-]
LG-01-1	1.6965	19.371	1.1803
LG-01-2	2.0144	20.833	1.3205
LG-01-3	No data	No data	No data

The laminated panes were able to withstand a greater pressure than the float glass, which also was expected. As a way to describe the response in the panes when subjected to the blast, the pressure recorded in the sensor closest to the specimen and displacements have been plotted together in Figure 4.19. At firing pressure 8.142 bar, both glass panes fractured, but due to the lack of data, the experiment could not be plotted.

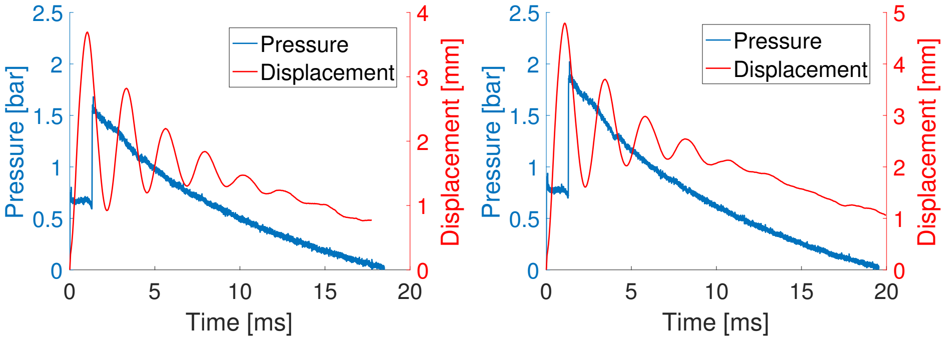

(a) LG-01-1 **(b)** LG-01-2

Figure 4.19: Correlation between pressure and displacement during blast tests

It may be seen in the Figure 4.19 that the displacement curves and the pressure data match the values presented in Table 4.12. The overall displacement of the midpoint is larger in test LG-01-2 than in LG-01-1 due to the higher loading pressure. $t = 0.0$ have

---

[1] Based on an examination of the pane after the experiment, the authors believes the fracture was initiated in the middle

been set to the time when the first impact of the blast wave hit the sensor closest to the glass, denoted P1-01.

The second test series was conducted 13th of March. During this day experiments LG-02-1, LG-03-1, LG-03-2, LG-03-3 and LG-04 were conducted. In series of tests, the fastening torque of the bolts were 100Nm, and the steel frame was used. The desired firing pressure for the first experiment this day, LG-02, was 6.7 bar, as for experiment LG-01-1. This time the glass pane fractured. For test LG-03-1 the same desired firing pressure was tried, but in this experiment, the glass did not fracture. Pane LG-03 was then examined for damage before it was tested again. Between test LG-03-1 and LG-03-2, the bolts fastening the frame were checked and the fastening torque had not changed and was still 100Nm. For test LG-03-2 the desired firing pressure was increased to 7.7 bar, but the glass did not fracture. In test LG-03-3 the desired firing pressure was increased to 8.6bar, and it resulted in the fracture of the pane. In experiment LG-04 the desired firing pressure was 8.6 bar. The reflected pressure and midpoint deflection at fracture, ΔM_{cr} is presented in Table 4.14.

Table 4.14: Pressure data recorded the experiments. (*) shows the maximum displacement of the glass without fracture.

Test	Pane	P_f [bar]	P_r [bar]	ΔM_{cr}[mm]	First fracture
LG-02	02	6.258	1.673	3.307	Close to the middle
LG-03-1	03	6.345	1.631	3.666*	No fracture
LG-03-2	03	7.593	1.989	4.541*	No fracture
LG-03-3	03	9.101	2.188	4.985	Close to the middle
LG-04	04	8.628	2.079	2.993	Close to the middle

The parameters of the Friedlander curve fit for the experiments conducted during the second series are tabulated in Table 4.15:

Table 4.15: Friedlander parameters for blasts experiments on laminated glass panes

Experiment	P_r [bar]	t_+ [ms]	b [-]
LG-02-1	1.6732	19.393	1.1495
LG-03-1	1.6317	19.188	1.0032
LG-03-2	1.9893	21.273	1.3997
LG-03-3	2.1876	24.000	1.6923
LG-04-1	2.0786	22.409	1.4579

As seen in Table 4.14 the displacement of the mid-point at fracture varies significantly. Additionally, both LG-03-01 and LG-03-02 have a larger mid-point deflection than LG-02 and LG-04, but without failure. These results emphasise the difficulties estimating the fracture strength when studying glass and laminated glass panes. When comparing to the regular float glass tests, the displacement at failure for the float glass panes was generally larger than for the laminated ones. This implies that the laminated glass panes are stiffer than the float glass panes. The initial fracture patterns for the panes that fractured are shown in Figure 4.20.

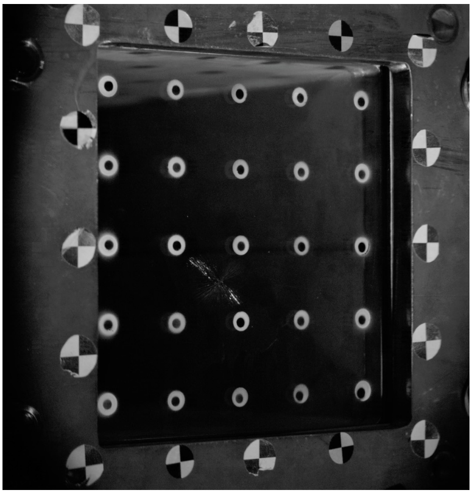

(a) LG-02

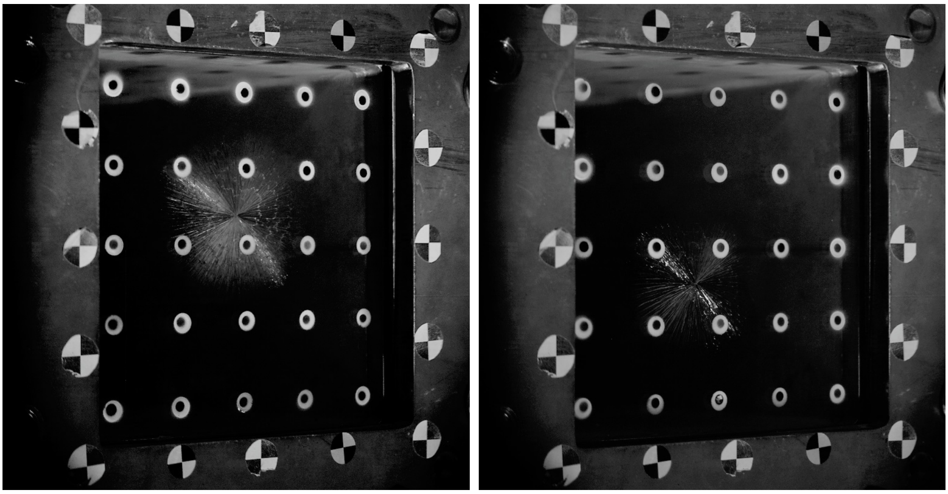

(b) LG-03-03

(c) LG-04

Figure 4.20: Crack initiation on the laminated glass panes tested 13/3-17

From the images of crack initiations, it may be seen that for the laminated glass panes the fracture occurred close to the middle in all three tests. This is in contrast to the float glass tests where the majority of the glass panes fractured close to the edge of the glass. With the number of experiments ran being this low it may be a coincidence, but worth mentioning. Another possible explanation for the difference in crack initiation may be the stress distributions in the different specimens. A reason for the cracks being centred in the middle may be that the laminated glass pane consists of two glass layers with a different distribution of microcracks. The probability of the critical microcrack being in the same place in both the glass panes is small, and therefore a fracture in the middle may be more likely as the stress concentration is at its maximum in this area. As for the glass panes tested in the previous series, a plot showing the correlation between pressure and displacement was made for these experiments. In Figure 4.21 the pressure and displacement graphs are presented with the fracture point for the glass panes that failed.

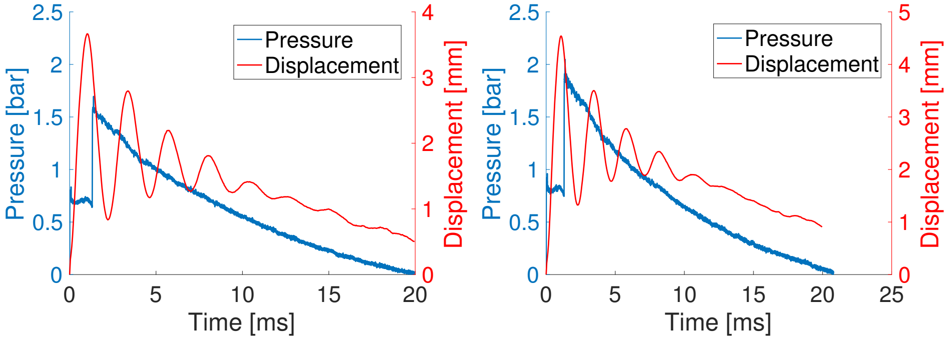

(a) LG-03-1

(b) LG-03-2

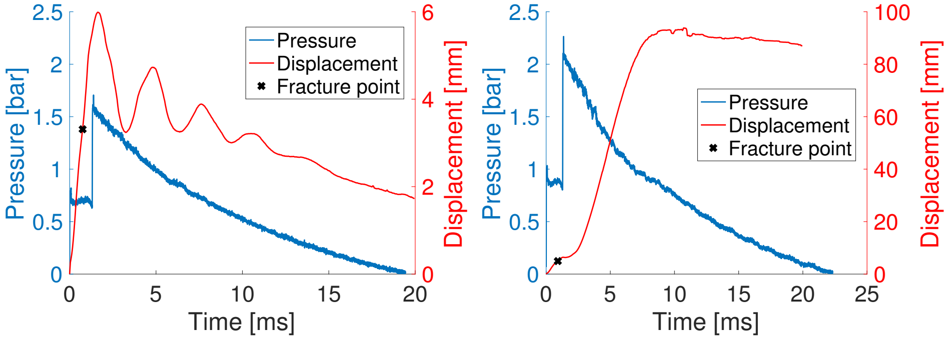

(c) LG-02

(d) LG-03-03

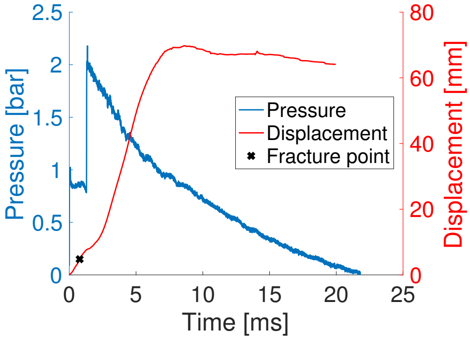

(e) LG-04

Figure 4.21: Correlation between pressure and displacement during blast tests 13/05-17

The pressure plotted in Figure 4.21 is the recorded pressure from sensor P1-01. The maximum displacements for the specimens that failed are much higher than for the ones that did not. An exception is LG-02 where one glass pane fractured, but with a displacement curve following the same pattern as the samples that withstood the blast. By looking at the images at maximum displacement, it is clear that glass LG-02 has significantly less damage than the specimens LG-03-03 and LG-04. When examined after the experiments it was seen that only one of the glass layers fractured. As seen in Figure 4.22 the size of the glass shards in the pane are much smaller for LG-03-03 and LG-04 than for LG-02. This may signify that the loading in LG-02 was close to the resistance of the laminated glass pane, while the loading in LG-03-03 and LG-04 was far over the limit of strength. The PVB did not rupture in any of the experiments conducted in wither of the series.

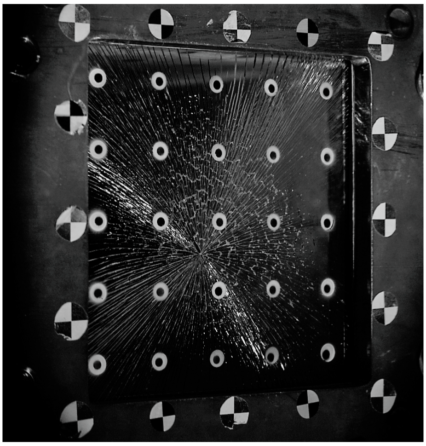

(a) LG-02

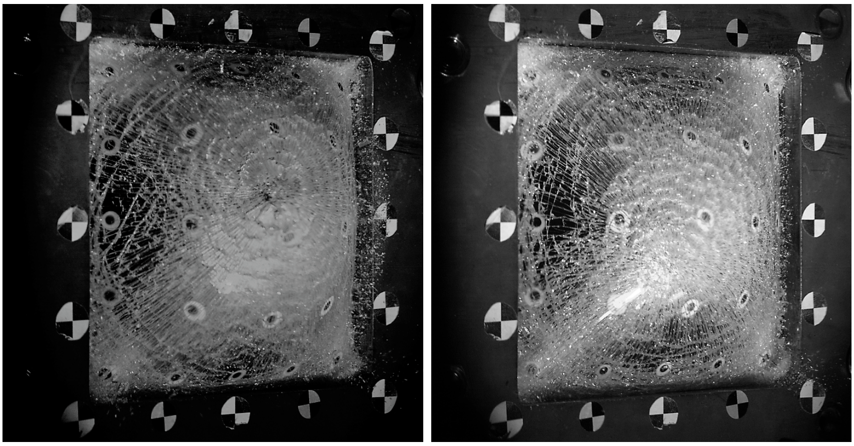

(b) LG-03-03

(c) LG-04

Figure 4.22: Damage in the glass at maximum recorded displacement

For LG-02 the glass had the same post fracture behaviour as the specimens that did not fail, oscillations in the midpoint displacement. The post-fracture behaviour of LG-03-03 and LG-04 had a bigger displacement during the experiment and a larger permanent deflection at the end of the test. For completely fractured panes as LG-03-03, a possible failure propagation during the blast is shown in Figure 4.23 and 4.24. In the case of these figures, $t = 0$ ms is defined as the time when the first crack appears in the glass pane.

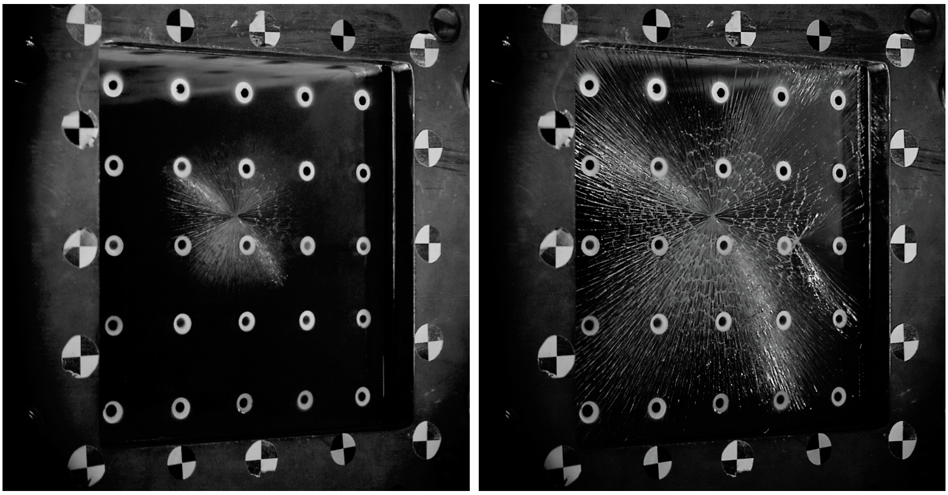

(a) t=0.00 ms **(b)** t=0.625 ms

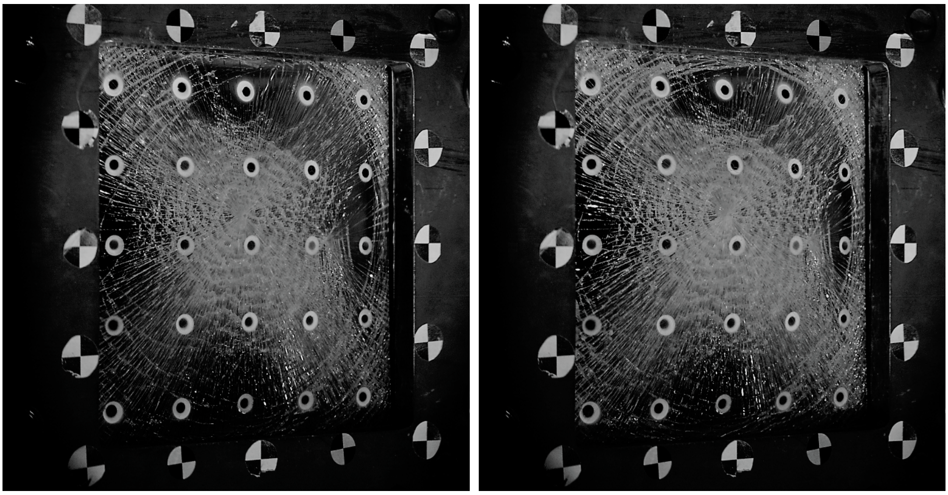

(c) t=1.708 ms **(d)** t=2.542ms

Figure 4.23: The failure propagation of the glass pane LG-03-3

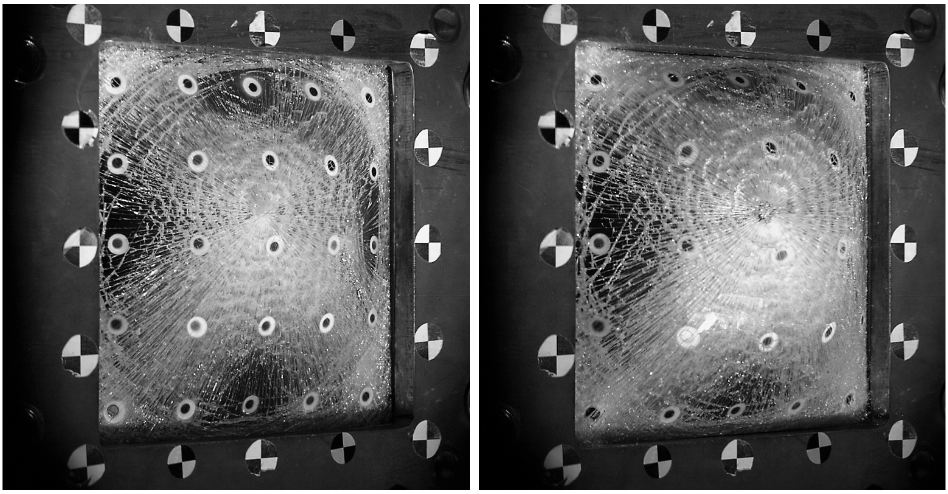

(a) t=3.458 ms **(b)** t=5.500 ms

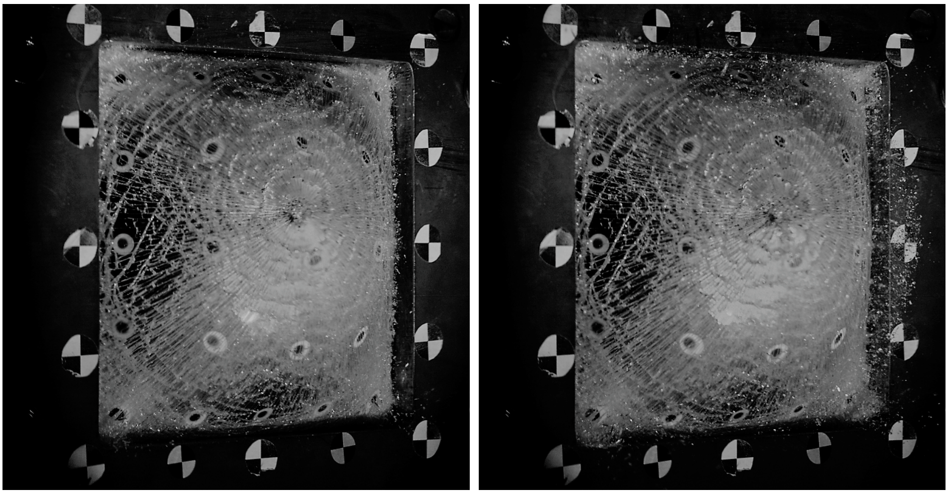

(c) t=6.500 ms **(d)** t=9.417 ms

Figure 4.24: The failure propagation of the glass pane LG-03-3

The effect of the PVB interlayer becomes clear when comparing the failure of a float glass pane with the failure of a laminated glass pane, i.e. Figures 4.13 and 4.24. In the failure propagation of the laminated glass pane the glass shards are small and still fastened to the PVB while in the float glass case, large glass shards accelerate after the blast and could potentially do damage to objects or people close to the blast. In Figure 4.24d it may be seen that glass dust is spreading from the glass pane, and compared to the shards from float glass blast response, this dust is several orders of magnitude smaller than the float glass fragments and is naturally less dangerous. On the images from the experiments conducted on laminated glass panes, no shards of glass were seen loosening from the PVB only ”powder” as seen in Figure 4.24d

As discussed in Section 3.1.2, PVB is a highly strain rate sensitive material. With that in mind, a study was conducted to estimate the strain rates in the PVB during the shock tube test. For the study, the experiment with the largest displacement and pressure was selected, in order to find the highest strain rates. The experiment selected was LG-03-3. To estimate the strain rates, a DIC analysis of the markers shown in Figure 4.25a was conducted to export the displacements in x-, y- and z-direction. Then, the relative displacements between point 3 and point 1, 2, 4 and 5 were calculated to find how the middle point moved compared to the surrounding points. With the relative displacements found, Pythagoras theorem in 3D was used to find the resulting engineering strain between points 1-3, 2-3, 4-3 and 5-3. The original distances, L_0, from the surrounding points to the midpoint were all 60 mm. The calculated engineering strain was then averaged to find an estimate of the strain in the area as a function of time. Due to big variations in strains between the different points, the authors chose to average the strains. By numerical differentiation, the strain rate was then calculated. In Figure 4.25b the results of the estimation is presented with the mid-point displacements and fracture point.

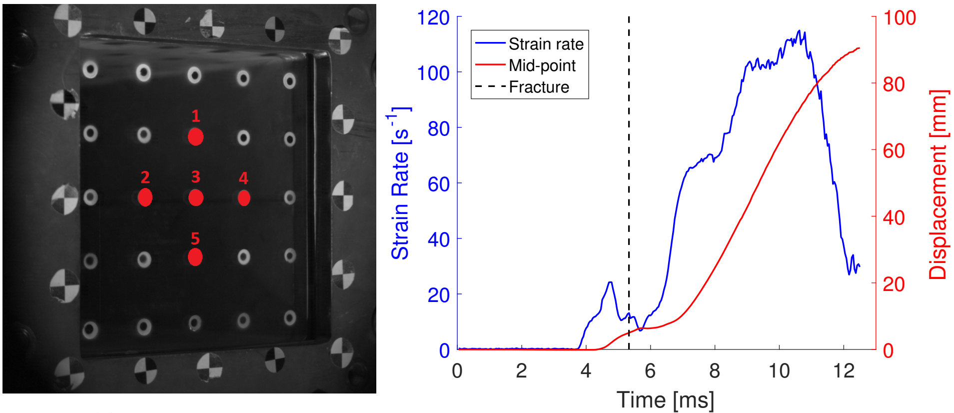

(a) Selected markers

(b) Strain rate and displacement

Figure 4.25: Selected markers and the results of the strain rate estimation

As the glass pane fractured and the displacement grew, the DIC program eCorr lost track of some of the subsets. The strain rate estimation was therefore stopped when the software lost track of one of the selected markers. This happened at approximately $t = 12.5ms$. It is emphasised that this is a rough estimate as the strains are calculated from a small number of discrete points.

As for the case of the float glass panes, a control of the boundary conditions was performed for the laminated glass blast tests. The frame used in the blast tests of laminated glass was made of steel which should imply less relative displacement in the frame compared to the frame made of aluminium. However, the increase in loading pressure was expected to increase the deflection. The experiment with the highest loading pressure, LG-03-3, was chosen because of the highest expected displacements. A DIC analysis of the point-tracking markers on the frame was conducted to obtain the corresponding displacements during the tests. Displacements at three different times were plotted in MATLAB, and the resulting 3D plot is presented in Figure 4.26. $t = 0$ ms is the time at impact, $t = 6.29$ ms the time with maximum displacement in the pane and $t = 5.04$ ms is an intermediary point

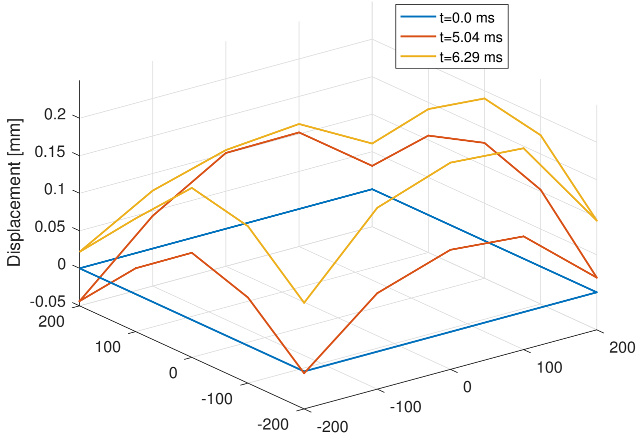

Figure 4.26: Frame displacement during LG-03-3

As for the boundary condition control conducted for the float glasses, the results have to be interpreted with caution due to the inaccuracy of the DIC measurements. As seen in the figure the displacement of one of the corners at $t = 5.04s$ is negative which makes no sense. This may be due to relative movement in the entire shock tube. Additionally, the maximum measured displacements are under $0.25mm$, which makes the displacement negligible when compared to the glass pane displacements. With a possible error up to $0.07mm$, the results may only be used as a qualitative representation of the behaviour of the frame.

A study was conducted to compare the displacements of the frame with different fastening torques. Neither of experiments LG-01-2 or LG-03-2 fractured during the tests and the reflected pressure in both the experiments were approximately 2 bar. The only difference between the experiments was the fastening torque. The displacements of the frames were plotted together for comparison, but the displacements were low. No clear pattern was seen and the results were thus excluded from the thesis.

Chapter 5

Numerical Modelling - Four point bending test

In this section, the numerical modelling of the four point bending test will be presented. The modelling will be limited to the large specimens.

5.1 Standard model

In the numerical modelling of the large specimen (300×60 mm), various numerical parameters were assumed from the start to achieve a standard model for a further parameter study. Symmetry was used in both x- and y-direction, as seen in Figure 5.1. Thus only a quarter of the beam was modelled. Both the glass and the PVB was modelled with 10×10 mm-mesh with one element over the thickness. To capture the bending effect properly, the 3rd order solid hexahedron element shown in Figure 2.14 was used in both the glass and the PVB. The adhesion of the PVB to the glass panes was done by using the *MERGE-function. Both the glass and the PVB were simplified and modelled as linear elastic materials with the use of three parameters; Young's modulus (E), Poisson ratio (ν) and density (ρ). The PVB was assumed linear elastic to reduce the complexity and since the PVB does not contribute notable to the strength before fracture takes place in the glass, in a quasi-static test. Since the experimental results for Young's modulus tabulated in Table 4.6 dispersed significantly due to a component test instead of a material test, E for glass was taken from the literature. The standard beam was modelled within the elastic area and without any fracture criteria. The total time was sat to $t = 0.1s$. The material parameters are listed in Table 5.1.

Table 5.1: Material parameters for PVB and Glass

	E [MPa]	ν	ρ [kg/m^3]
PVB	2.36 [56]	0.45 [56]	1100 [3]
Glass	70000 [24]	0.23 [24]	2500 [12]

Rigid pipe-sections were used to model the supports and loading cylinders. To obtain a smooth surface, the *SMOOTH_MESH-function was utilized. The density was sat to $\rho = 7800$ kg/m^3 [57] as it was made of stainless steel. The two supports was constrained from translation movement in all directions, while the loading cylinders only were able to move orthogonally to the laminated glass (z-direction). All cylinders were able to rotate freely, which was also the case in the experiment. A general contact formula was used, where all surfaces were allowed to be in contact. The load was applied by using the integrated smooth displacement function:

$$smooth\_d(d_{max}, t_0, t_1) \tag{5.1}$$

which gave a smooth displacement increasing from 0 at time t_0 to d_{max} at time t_1. Since the experimental specimens had a mid-span deflection within a range between 2.2-3.2 mm, the d_{max} was given a value of 3 mm, which assured a curve through the experimental data. A general representation of the numerical standard model is shown in Figure 5.1.

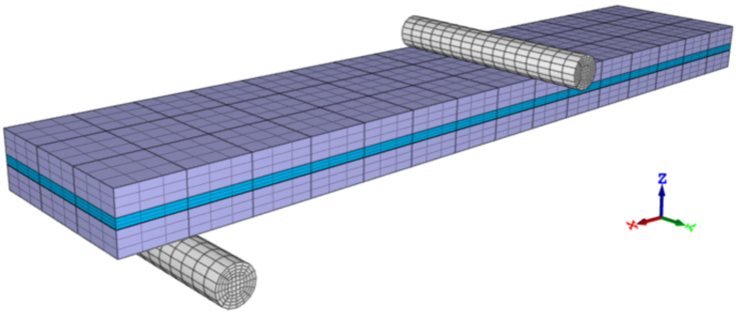

Figure 5.1: General setup of the numerical 4 point bending-model made in IMPETUS. Symmetry was used in both x- and y-direction.

After the standard model had been established, the simulation was conducted. In Figure 5.2 the resulting force-displacement curve plotted in MATLAB is presented. The experimental results are presented with the black scatter plot, which represents the fracture point for each test specimen. It can be seen that the results from the standard beam were found to be a bit softer than the experiments, but as a first simulation, the curve was found sufficient. Further parameter studies were conducted to find a better fit to the experiments later in this chapter. Another thing to notice is the shape of the curve. Some explicit noise appears in the results due to the short simulation time. This issue will be checked later in the chapter using an extended total time with a slower loading speed, which should give smaller dynamic oscillations. The kinetic energy was under 0.1% of the internal energy, so no inertial effects were added.

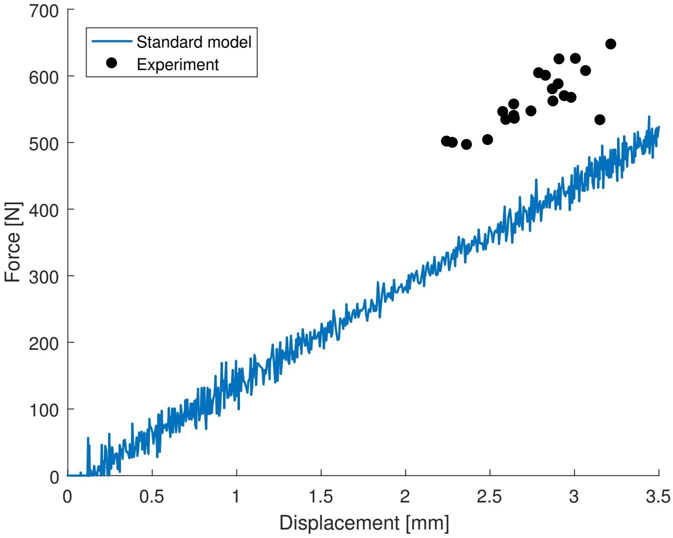

Figure 5.2: Resulting force-displacements curve for the standard model implemented in IMPETUS

5.2 Parameter study without fracture criteria

To attain a better standard model for further studies, a parameter study of the total time and Young's modulus was conducted without the use of fracture criteria in the glass. The standard model presented in Figure 5.2 was used as template in this study.

5.2.1 Total time

As mentioned in Section 2.7.1, explicit methods are not fitted for quasi-static simulations with long total times due to the maximum time step criterion. With the use of the standard model, the critical time step was found directly from IMPETUS to be approximate $\Delta t_c = 2 \times 10^{-7}$ s. From the four point bending experiment of the large samples, the loading speed was sat to $v = 8.6$ mm/min. For a cylinder displacement of 3 mm, the simulation would have required more than 104 million time steps. To avoid lengthy simulations, it is evident with time scaling on the cost of some dynamic oscillations. Four simulations with different total times were conducted. With resulting force-displacement curves in the same graph, the differences were not shown adequately, so the curves are separated into four different graphs presented in Figure 5.3. The corresponding time steps and running times are tabulated in Table 5.2.

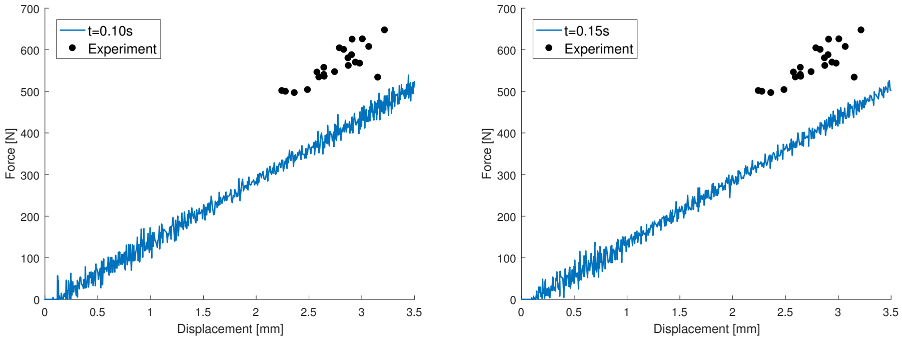

(a) t=0.10s **(b)** t=0.15s

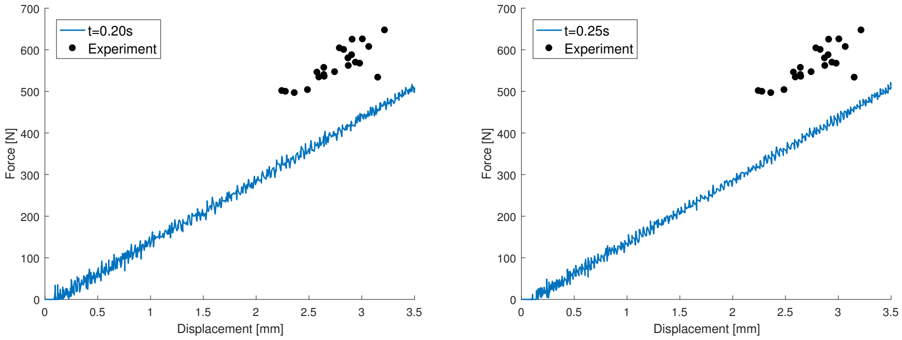

(c) t=0.20s **(d)** t=0.25s

Figure 5.3: Force-displacement curve for different total times

Table 5.2: Different total times with corresponding time steps and running times

Total time [s]	Time steps	Running time
0.10	496 610	41min 37s
0.15	744 914	55min 53s
0.20	993 218	1h 17min
0.25	1 241 522	1h 34min

The fluctuations are decreasing with the use of longer total times. For the simulations with $t = 0.10s$ and $t = 0.15s$, it is shown areas with visibly higher fluctuations at the beginning and the end compared to the middle area. The fluctuations are too large and inconsistently in these simulations. The simulations with $t = 0.20s$ and $t = 0.25s$ also have fluctuations, but they are smaller and more consistently stable in their behaviour. To reduce the computational cost and since both curves showed satisfactory results, $t = 0.20s$ is the preferred choice of time and is being used for further parameter studies. The kinetic energy is small in all simulations compare to the internal energy, and the slope is well represented inn all the simulations.

5.2.2 Young's modulus

As earlier mentioned in Section 3.1.1, float glass is shown to be insensitive to strain rate when it comes to Young's modulus. Also from the literature [19; 24; 12], the Young's modulus for glass is consistently being defined as $E_{glass} = 70$ GPa. Therefore, the E_{glass} was defined as constant in this thesis as well, being 70 GPa. The PVB, on the other hand has shown to be highly strain rate dependent, mentioned in Section 3.1.2, and was found to be a suitable parameter to being modified. E_{pvb}-values of 2.36, 5, 8 and 10 MPa were applied, and the resulting force-displacement curve together with the corresponding experimental fracture points from the large samples is shown in Figure 5.4.

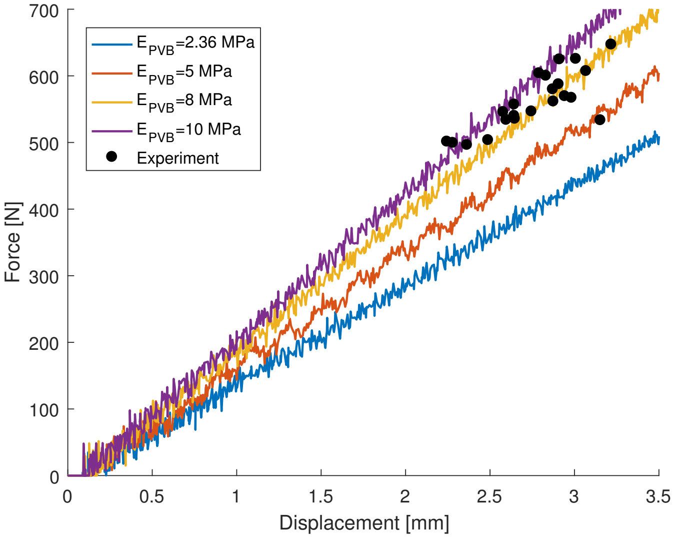

Figure 5.4: Force-Displacement curve for different Young's moduli applied in IMPETUS, large samples

The resulting graphs were as expected. With a larger Young's modulus, the model got a stiffer behaviour. The curve with the use of $E_{pvb} = 5$ MPa showed a different shape compare to the other curves with longer steps between the oscillation tops and with slightly bigger oscillations. The authors could not find the logic behind it considering that only the E-modulus was changed, but the elastic slope was clearly in good agreement with what was expected.

Looking at Figure 3.1, the initial stiffness of PVB is shown to lie around 10-12 MPa for the curve with $\dot{\varepsilon} = 0.2s^{-1}$. The strain rate in the four point bending experiment was below $\dot{\varepsilon} = 1.0 \cdot 10^{-4}s^{-1}$, discussed in Section 4.1.1. Since PVB has a softer behaviour at lower strain rate, the numerical results looked reasonable with the lowest value of 5 MPa and the highest value of 10 MPa. The best fit was in the author's opinion the model using $E_{pvb} = 8$ MPa, and this was also used for further parameter studies.

5.3 Parameter study with fracture criteria

In this section, a failure criterion was added to the model to see how different mesh sizes and different critical stresses contributes to the simulation output. It is noted that for larger thin plate models, symmetry should be used with caution while simulating brittle materials like glass due to cracks occurring randomly over the specimen. The authors considered the test specimen to be small enough and because no initial damage was added in the model, symmetry was found to be suitable. Shorter computational time was also taken into account when symmetry was chosen. The fracture criteria feature *PROP_DAMAGE_BRITTLE consisted of the critical stress (σ_c) and the critical stress factor for crack propagation (K_c), and are tabulated under in Table 5.3. Node splitting was used instead of element erosion as erode method.

Table 5.3: Fracture criteria for glass

σ_c [MPa]	K_c [MPa $\sqrt{mm}$]
47.47 [12]	23.72 [12] [1]

5.3.1 Mesh size

Elements over the specimen face

To examine the effect of the mesh size, four different element sizes were tried out over the specimen face in both the glass and PVB. Mesh sizes of 15×15, 10×10, 5×5 and 3×3mm were simulated and compared. Other parameters from the previous section were held constant. The resulting force-displacement curve is presented in Figure 5.5, while the corresponding Number of elements (NOE) and running times can be seen in Table 5.4.

Table 5.4: Different mesh sizes with corresponding time steps and running times

Mesh size [mm]	NOE	Running time
15×15	2620	1h 19min
10×10	2695	1h 36min
5×5	3100	5h 41min
3×3	4060	15h 20min

---

[1] Value converted from 0.75MPa$\sqrt{m}$

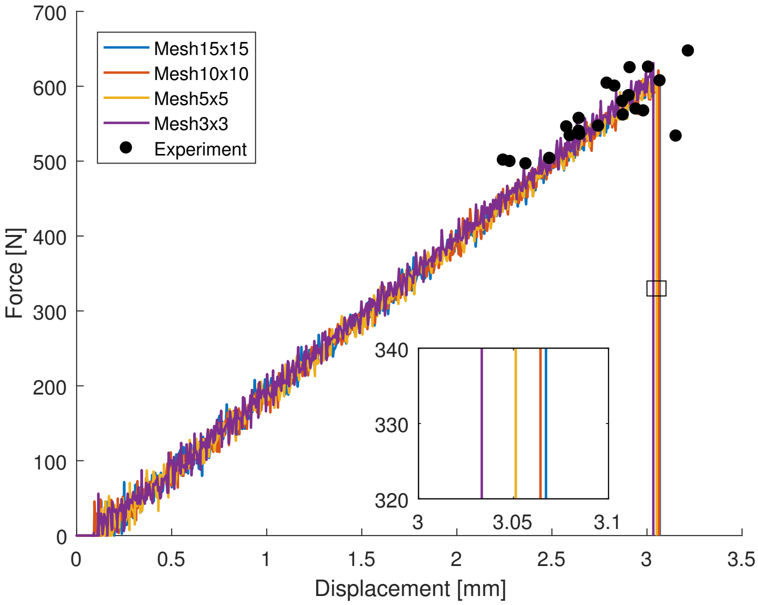

Figure 5.5: Force-displacement curve with different mesh sizes in both the glass and PVB

It may be seen from Figure 5.5 that neither the force-displacement curve or the fracture points are changing noteworthy. The fracture point varies within a displacement value of 0.035 mm between Mesh 15×15 and Mesh 3×3, which is considered negligible. It is however noted that the fracture strength shows the trend of being slightly larger for coarser meshes. This is presented in the zoomed-in-box in Figure 5.5. The initial fracture pattern seen from underneath the specimen is shown in Figure 5.6. It indicates that all the meshes have a fracture pattern mainly in the middle part of the specimen, which also was expected. All in all, the study indicates that the model is insensitive to mesh size in the elastic area, which may be caused by the 3$^{\text{rd}}$ order element choice. These elements are as earlier mentioned able to capture the bending well and may be more insensitive to mesh sizes. The running time with smaller elements increased significantly, shown in Table 5.4. With the coinciding results and the big difference in running times, the authors chose to use the 10×10-mesh for further studies.

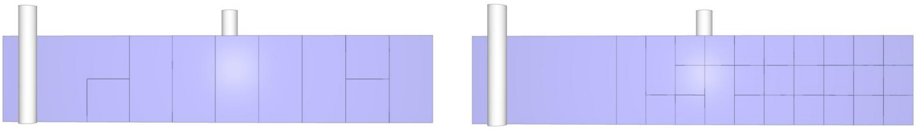

(a) 15×15 mm

(b) 10×10 mm

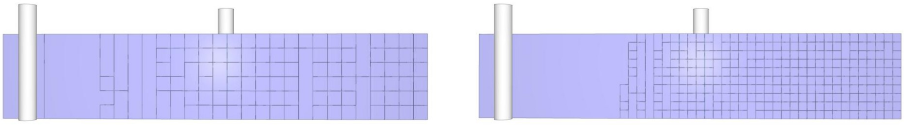

(c) 5×5 mm

(d) 3×3 mm

Figure 5.6: Initial fracture pattern seen from underneath the specimen for different mesh sizes

Elements through the glass thickness

Three different number of elements (1, 2 and 3 elements) were simulated through the thickness of each glass pane. The PVB layer was held constant with the use of one element through the thickness, and the standard mesh of 10 × 10 mm was used on the faces of all layers. Rest of the model used parameters as given earlier in this section. The resulting force-displacement curve is plotted in Figure 5.7. The corresponding running times are tabulated in Table 5.5.

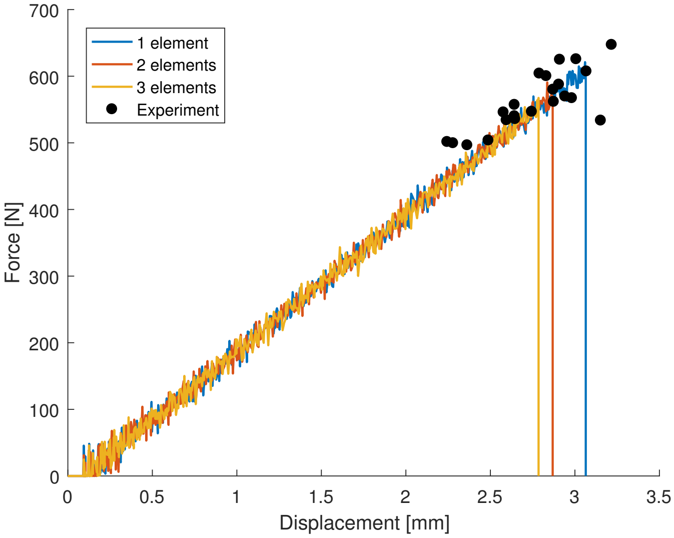

Figure 5.7: Force-displacement curve for a different number of elements applied through the thickness of each glass pane

Table 5.5: Elements through thickness of glass panes with corresponding running times

Elements through glass thickness	Running time
1 element	1h 36min
2 elements	6h 3min
3 elements	10h 14min

As in the mesh size study, the curves up to the first fracture point is shown to have the same shape, which gives a consistent bending stiffness for all three simulations. The point of fracture, on the other hand, occurred earlier with more elements through the thickness. It is believed to happen because the stress concentration gets bigger with a finer mesh, and will therefore reach the fracture criteria faster.

When a crack starts to propagate through a thin glass pane, it requires a small amount of energy for the crack to propagate through the whole thickness. With the use of more elements in the numerical model, the crack propagation may suddenly stop in the middle of the pane, see Figure 5.8, which is a nonphysical behaviour. The initial fracture pattern seen from underneath the specimen is shown in Figure 5.9. With use of more elements, less cracks occurs over the longitudinal direction, which also is case for in the experimental specimens shown in Figure A.3 in Appendix A. This being said, none of the fracture patterns shows any particular good compliance compare to the experiments. With a notable lower running time and from the authors opinion a more realistic setup, 1 element (3$^{\text{rd}}$ order) through the thickness was used for further studies.

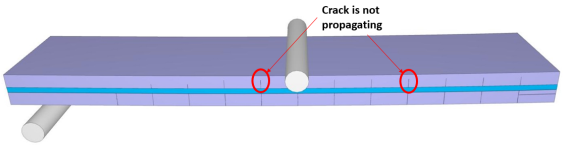

Figure 5.8: The cracks do not propagate throughout the upper glass pane when 3 elements are used in the glass thickness.

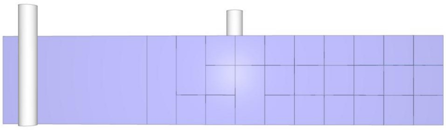

(a) 1 element

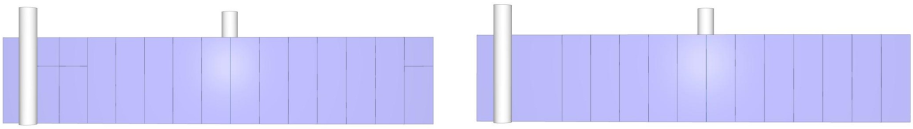

(b) 2 elements

(c) 3 elements

Figure 5.9: Initial fracture pattern seen from underneath the specimen for a different number of elements through the glass thickness

5.3.2 Critical stress

For this parameter study, five different critical stress values were used. From earlier results, the standard model with use of $\sigma_c = 47.47$ MPa showed to lay within the experimental results, but a little bit higher than the mean value. With this in mind, one higher and three lower σ_c-values were tried out, ranging from 30MPa to 50MPa. The critical crack propagation factor (K_c) was held constant as given in Table 5.3. The resulting force-displacement curve is shown in Figure 5.10.

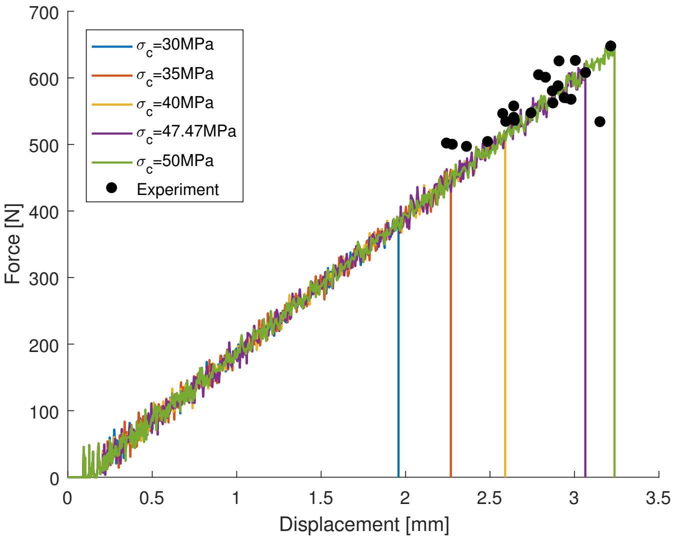

Figure 5.10: Force-displacement curve for a different number of critical stress-values

From the figure, the five simulations showed to be located on top of each other until each of them fractured, which naturally means that the critical stress does not influence the bending stiffness. The fracture strength, on the other hand, showed to be highly affected by the critical stress, which also was expected. The models have the same stress buildup, but fractures at different stress values. The running times were approximately the same for all simulations and did not show any systematically change with different σ_c-values.

The different simulations were able to represent the whole experimental set, from lowest value of 35MPa up to 50MPa. The model with use of 30MPa was the only test outside the experiments. The mean value and best fit seemed to be located around 43-44MPa.

5.4 Summary and Discussion

To summarise the numerical modelling of the four-point bending test, it is natural to compare the results of the simulations with the results of the experiment. With the use of elastic beam theory, no trustworthy material parameters were calculated from the experimental results. Material parameters were taken from the literature. The explicit code in IMPETUS was able to describe the behaviour of the glass up to cracking. As seen in Figure 5.2 showing the force-displacement curve for the standard beam, the graph did not intercept the scattered area representing failure in the experiment. Only elastic properties were given to the materials and a fracture criteria was given to the glass when mesh size and critical stress studies were conducted. As seen in the results, the curves are oscillating as a consequence of numerical noise. This is a direct effect of the essential time scaling. When neglecting the noise, the numerical results showed the expected linear relationship between the force and displacement.

As discussed in the results, the different parameters affected the graphs in different ways. The increase of total running time decreased the magnitude of the fluctuations, but at the price of higher computational cost. The Young's modulus of PVB affected the flexural strength as assumed, and the higher Young's modulus, the higher stiffness the specimen got. As seen in Figure 5.5 and 5.7, different mesh sizes in the over the specimen face did not affect either the flexural or fracture strength, while extra elements in the glass thickness decreased the fracture strength. The running time went significantly up with the use of both smaller and more numerous elements. The results from the critical stress parameter study were as expected; no changes in the stiffness or any noteworthy graphical appearance, just earlier fracture of the glass.

As a concluding remark, the IMPETUS code was in the author's opinion able to describe the elastic behaviour of the laminated glass adequately. It had some numerical noise but showed the expected linear response. In Section 2.7.3, it is stated that the explicit method is ideal for high-speed dynamic simulations while the implicit method is the preferred choice in quasi-static simulations. When large non-linearities are involved, explicit method is the best choice. For the four point bending simulation, an implicit method would have been the best option, but since IMPETUS Afea Solver only operates with an explicit method, this was not possible. This led to longer running times.

Chapter 6

Numerical Modelling - PVB tensile test

PVB and the properties of PVB plays an important role in laminated glass exposed to blast loading, and it is important to be able to model the material correctly. A ”reverse engineering” approach was used to calibrate a material model aimed to work at the different strain rates the PVB is subjected to during a blast experiment. The experimental data used for comparison was adapted from Hooper et. al [3]. In this chapter, a numerical model of a PVB tensile test will be presented.

6.1 Results from Hooper et.al

Hooper et. al performed tensile tests on dog-bone specimens cut from a sheet of PVB. The specimens had the dimensions according to *Type 2* as recommended in the ISO 37:2011 [58] with a thickness of 0.76 mm, see Figure 6.1. The tests were run at different loading rates to check how PVB reacted when stretched at various strain rates. The strain rates tested were $0.2s^{-1}$, $2s^{-1}$, $20s^{-1}$, $60s^{-1}$ and $400s^{-1}$.

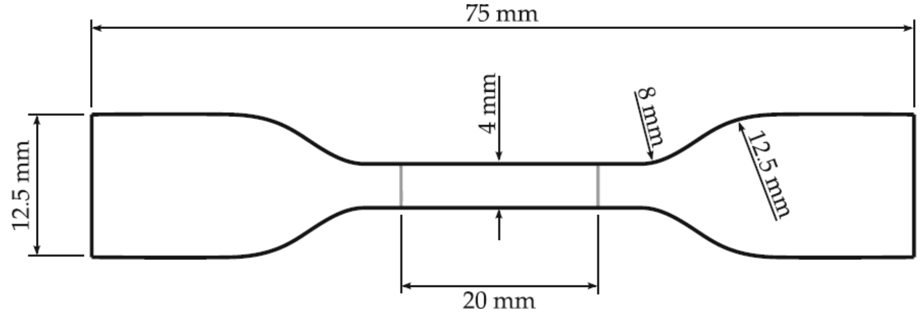

Figure 6.1: Dimensions of the dog-bone specimen tested in the PVB tensile tests by Hooper et. al [3]

To convert the engineering stress-strain-curve from Hooper's papir into numbers, the plot extract program "Web Plot Digitizer" was used. The picture of the stress-strain graph from Hopper's experiment was uploaded in the program, and four reference points were set so the software could define a coordinate system. Each curve was then established through 70-100 points. Web Plot Digitizer provided a text file with all the coordinates so they easily could be plotted in MATLAB. Both plots are shown in Figure 6.2.

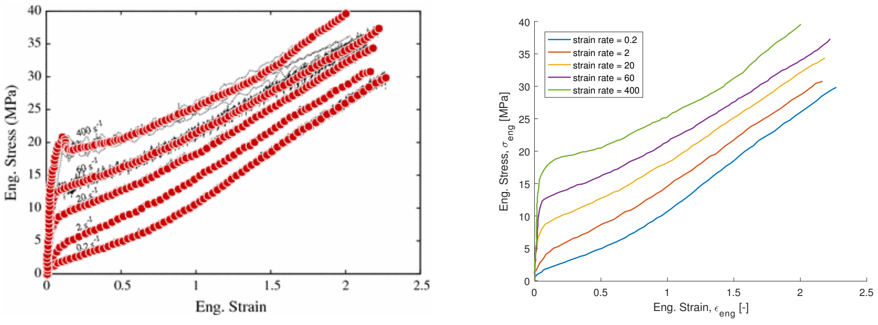

(a) **(b)**

Figure 6.2: a Procedure of the extraction of stress-strain data from Hooper et al. [3] in Web Plot Digitizer **b** Engineering stress-strain curve

When considering large strains as $\varepsilon > 2$, a non-negligible reduction in cross-sectional area is often introduced. This leads to higher stress concentration and needs to be taken into account. The true stress, σ_t, uses the current cross-section instead of the original cross-section. For rubbery materials where the Poisson ratio lies close to 0.5, which implies an incompressible material, the volume is constant for any change in the cross-sectional area. With this assumption, the relation:

$$\sigma_t = \sigma(1 + \varepsilon) \tag{6.1}$$

applies where ε is the engineering strain and σ is the engineering stress. The stretch ratio,

λ, is defined with use of the engineering strain by the relation:

$$\lambda = 1 + \varepsilon \tag{6.2}$$

Using these relations, a true stress-stretch ratio graph from Hooper's et. al was calculated using MATLAB. The resulting plot is shown in Figure 6.3.

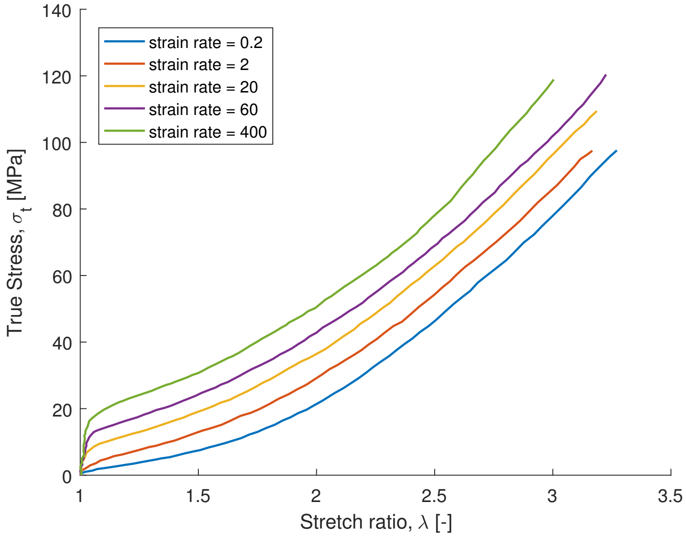

Figure 6.3: MATLab plot of the true stress vs. stretch ratio from Hooper et. al [3]

6.2 Model of specimen

To recreate the tests conducted by Hooper et. al [3] the specimen was modelled in IMPETUS. This was to ensure that the material models available in IMPETUS were properly calibrated before the numerical simulations of the blast tests. As pointed out initially this was the goal of the PVB stretch modelling.

A preliminary study was conducted to determine which geometry should be used in the numerical simulations. The computational most efficient way to simulate the tensile test would be to only model the $20 \times 4 \times 0.76$ mm gauge in the middle of the dog-bone sample instead of the whole specimen. To verify whether or not a simulation with only the gauge was applicable, the results from a model of the whole specimen was compared to the results from a model of only the gauge.

The dog-bone specimen was modelled with the dimensions as pictured in Figure 6.1. A mesh file was generated in ABAQUS and then imported to IMPETUS. In order to capture the deformations in the gauge properly, the mesh in this area was refined. Additionally, the polynomial order of the elements in the exposed zone was changed in the IMPETUS code to 3$^{\text{rd}}$ order. The meshed dog-bone is shown in Figure 6.4a.

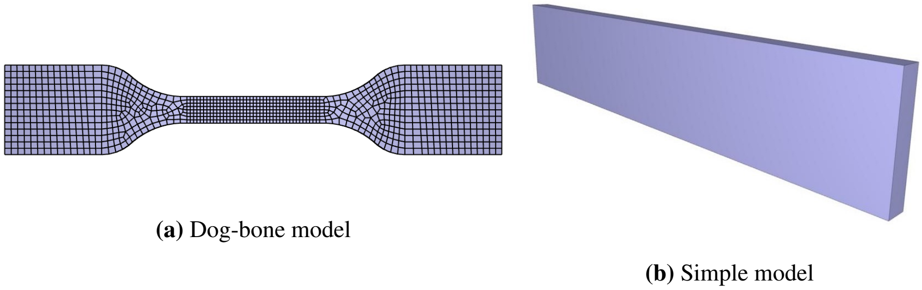
(a) Dog-bone model

(b) Simple model

Figure 6.4: Dog-bone and simple model used in the preliminary study of PVB tensile test

The dog-bone was loaded at one end with the *smooth_d-function used in Chapter 5, and was fixed at the other end. In the preliminary study, for simplicity, the PVB was set as linear elastic with material parameters as listed in Table 6.1

Table 6.1: PVB material data for the preliminary study

E [MPa]	ν	ρ [kg/m^3]
2.36 [56]	0.45 [56]	1100 [3]

The model with just the gauge was simplified to a minimum. The gauge was modelled with one 8-node hexahedron element with the dimensions described above. The boundary conditions were the same as for the dog-bone mode, as was also the material data tabulated in Table 6.1, the strain rate and the maximum displacement. The comparison, in the form of a stress-strain curve, was conducted with the maximum strain rate of 400 s^{-1}. The effects of the geometry and size of the specimen were assumed more significant at higher strain rates as the consequences of the stress wave propagation through the specimen was assumed to be larger than for the lower strain rates. As seen in Figure 6.5 the stress-strain curve are more or less the same for the two geometries. Based on this control, the authors continued with the simple model to save computational power.

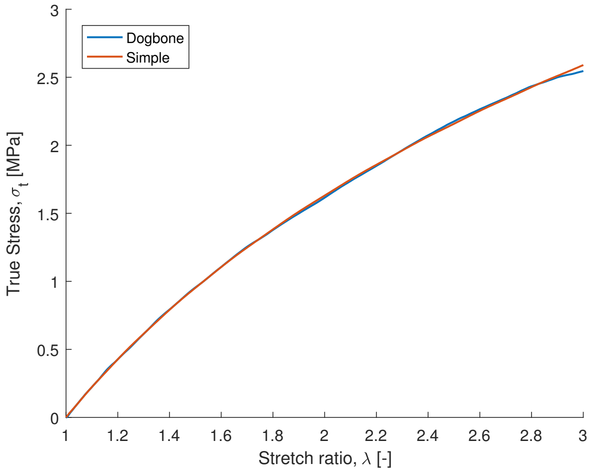

Figure 6.5: Stress strain comparison between the fully modeled dog-bone and the simplified model

6.3 Bergström-Boyce material model

To describe the behaviour found in the experiments done by Hooper et. al, shown in Figure 6.3, the Bergström-Boyce (BB) material model was calibrated. As mentioned in Section 3.2.3, BB is a constitutive model with two networks, one that gives the equilibrium response and the other contributing to the viscoelastic behaviour. For high strain rates, as tested by Hooper et. al, the viscoelastic contribution is significant and thus making the pure elastic model unable to capture stresses in the material accurately. By manipulating the material parameters in IMPETUS, the authors aimed to find parameters creating the same curves as shown in Figure 6.3. A trial and error approach was used to test how the different material parameters in the model affected the resulting true stress-stretch ratio plot.

The initial parameter study that was conducted using the BB-model with and without the viscous network, σ_B, to see how this network affected the true stress. The numerical simulations were run with an average strain rate of $400s^{-1}$ to get the highest viscous stress, and compared with the coherent experimental result from Hooper et al. The resulting true stress-stretch ratio curve from the initial parameter study is shown in Figure 6.6,.

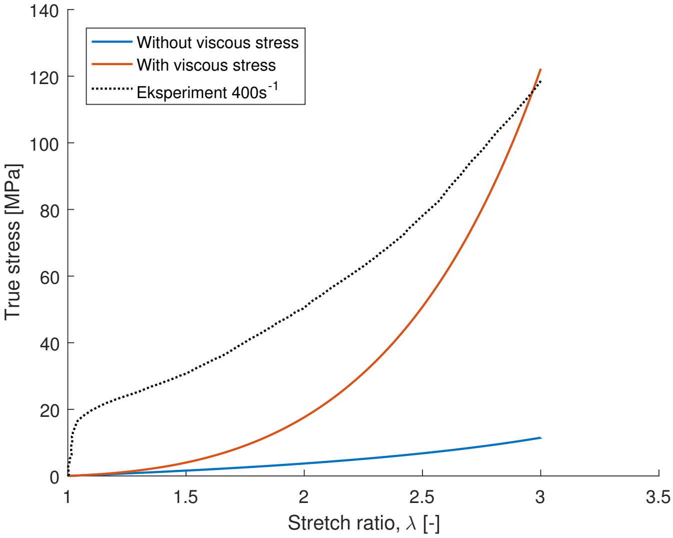

Figure 6.6: Comparison between Bergström-Boyce material model with and without the viscous stresses

As seen in the results, the viscous stresses are dominant in the simulation with a strain rate this high. As the material is stretched the viscous stress increases exponentially while the elastic stress, shown in blue, increases almost linearly. As the strains in a blast experiment are assumed to be high, up to $120s^{-1}$, the behaviour of PVB at high strains is of importance. The parameters used in the simulation run with the viscous part are listed in Table 6.2:

Table 6.2: Values used in the numerical simulations with the viscous stress network activated

ρ [kg/m^3]	K [MPa]	μ [-]	λ_L	a_0
1100	1000	1.0	2.72	0
a_1	η_{max}	$\dot{\gamma}_0$	ξ	B
0	1	1	0	0
σ_0	Q	C	m	c_{dec}
0	0	0	0	1
β	W_c	b_0	b_1	b_2
0	0	2.58	1	0.33

For the simulation run without the viscous stress, the parameters used were the ones affecting network A: ρ, K, μ and λ_L. The numerical values used in the parameters in network A were the same for both the numerical simulations, but the simulation with viscous stresses also included the parameters listed in Table 6.2. The parameters listed were used as the basic material model for a parameter study performed to find the best fit. Based on previous blast tests performed at SIMLab, the expected strain in the PVB during a blast test is between 10 s^{-1} - 120 s^{-1}, thus making the experiments performed by Hopper [3] at strain rate 60 s^{-1} the most relevant for this exercise.

It should be noted that the original BB-model [50] have a different setup compared to the model used in IMPETUS. The original model has a network A consisting of a hyperelastic spring, and a network B with a hyperelastic spring in series with a viscoelastic-flow element. The IMPETUS-model has the same network A, but misses this hyperelastic spring in network B. Both models are illustrated in Figure 6.7.

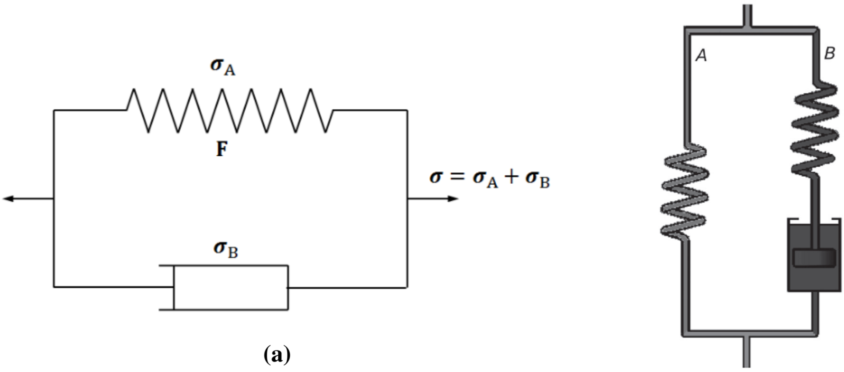

(a)

(b)

Figure 6.7: Model setup of Bergström-Boyce-model in (**a**) IMPETUS [42], and (**b**) Original setup from [50]

6.3.1 Best fit parameter study

There are 20 different parameters in the Bergström-Boyce material model available in IMPETUS, which makes the trial and error approach with the isolation of parameters a tedious task. The parameters initially tried were suggested by Professor Odd Sture Hopperstad, from the Department of Structural Engineering at NTNU, and from there a trial and error approach was used to tweak the parameters to fit with the results from Hoopers [3] experiments. By Hopperstads suggestion, the parameters regarding the Mullins damage were set to 0, see Section 3.2.3. The density was taken from [3], and the bulk modulus was adapted from [59]. The b_0 value was fitted with linear regression by Hooper. Additionally to the curve fit accuracy, the authors was interested to how the running time was affected by the different parameters. The model was to be used in the blast simulations, and a material model with an exceptionally long running time would not work when scaling to a whole laminated glass window. The maximum running time with a single 8-node element was 41 min, making it unfitted for a simulation with several thousands PVB elements. The final result of the parameter study had a running time of 2 min and seemed to be more applicable for the blast load. The best fit curve is shown in Figure 6.8.

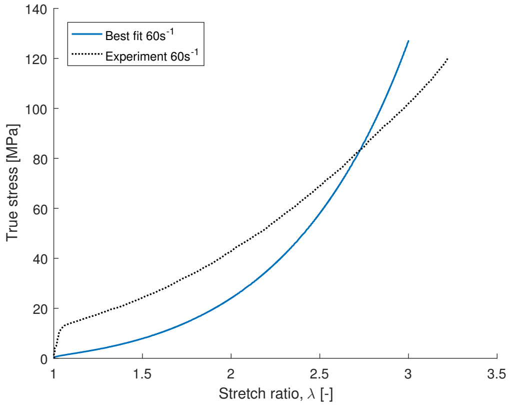

Figure 6.8: Best fit PVB material model with Bergström-Boyce

The nominal strain rate during the simulation was calculated to control if this curve lay the expected area. Seen in Figure 6.9, the strain rate was constant positioned just above 60 s^{-1}, which was a good result.

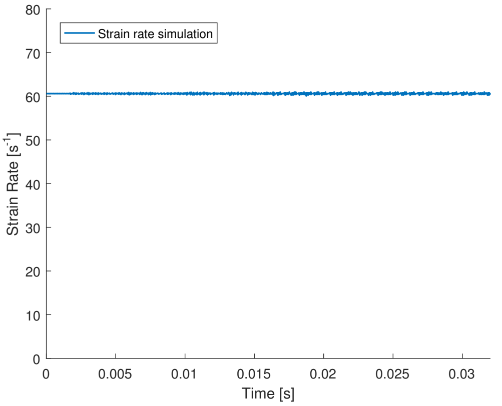

Figure 6.9: Best fit PVB material model with Bergström-Boyce

As seen in Figure 6.8 the best fit curve does not represent the experimental curve in a good way. Though the model has more or less the same stress at the end of the simulation, the curve does not have the same shape as the experimental results. The authors were not capable of tweaking the parameters to get the initial rise in stress. As pointed out there are 20 different parameters, and with the lack of sufficient experimental data, the authors failed to find a good fit with the reverse engineering approach. If the BB-model in IMPETUS was modelled as the original type, the curve fit might have been better.

6.4 Discussion

During the study of PVB for this thesis, it became clear that the PVB material properties is complex. PVB is a highly strain rate sensitive material with a great dependence of viscoelastic stresses. Additionally, to the authors' knowledge, no previous paper has been written on the topic of material modelling of PVB with the BB material model. This being said, papers have been written about the material properties of PVB but with other material models. The reason for using the BB-model and not one of the other more investigated models was because this was the only model which included viscous stress contributions in IMPETUS. The interested reader is referred to the papers discussed in Section 1.2 for other PVB material models.

The spread in approaches and material models may signify that there is no practice agreed upon when it comes to numerical modelling of PVB. Due to the time limitations of this thesis, the only material model explored was Bergström-Boyce and a linear elastic material model. As seen from the best fit curve, the model does not look applicable for modelling of PVB. Additional research and parameter studies might have yielded better results.

The authors experienced, during the parameter study, a strong codependency between the different material parameters in the BB material model. To the authors' knowledge, the effect of a change in one of the parameters was dependent on the values in one of the other. This resulted in a tedious process of deciphering how the different parameters affected the curve and the stress-stretch relationship. Based on the results and the experiences from this thesis, the authors would not recommend the same approach, but a direct calibration from experimental results. There are no guarantee that the parameters found in this parameter study are applicable to different loading situations or strains larger than the ones tested in this study.

As mentioned earlier in this chapter, the BB-model have a different setup in IMPETUS then how the model originally is modelled. The lack of the hyperelastic spring in series with the viscoelastic-flow element in network B, may be a crucial factor that could have affected the best fit for the PVB material model (Figure 6.8) in a positive way. For a strain rate of 60 s^{-1}, there is an initial rise in stress level in the experimental data from Hooper et. al [3]. This detail may have been captured with a modification of the material model in IMPETUS.

Another uncertainty of calibrating the PVB material based on a tensile test of "untouched" PVB may be that the PVB has a different behaviour before and after lamination. The authors were made aware of this issue from Professor Tore Børvik, from the Department of Structural Engineering at NTNU.

Chapter 7

Numerical Modelling - Blast Tests

The third and last numerical study of the blast experiment conducted in the SIMLab shock tube at NTNU. Both failing and non-failing single float glass panes and laminated glass panes were investigated. To capture the qualitative failure mechanism from the blast experiments was a main goal for the numerical simulations. For all simulations, IMPETUS was used as the numerical tool.

7.1 Float Glass

In Figure 7.1 shows the general setup of the numerical float glass model is illustrated. The float glass was modelled with one 3.8 mm float glass layer, and with a rubber sealant on each side to support it. In the experiments, the glass panes were fastened by an aluminium frame with 12 bolts tightening it up. In the IMPETUS model, the frame was neglected, and the outer part of the rubber sealant was instead fixed from translational movement in all directions. As discussed in Section 4.2.3, the frame displacement was small compared to the glass displacement, thus the assumption with with fixed edges. Both the rubber and the glass were simplified as elastic materials (*MAT_ELASTIC) with parameters given in Table 7.1. It is important to notice that rubbery materials usually have a different behaviour when exposed to high strain rates, like in a blast situation [48], but it was not conducted any test on the rubber for this thesis, so the material properties were given from PhDc Karoline Osnes as she had experience from previous simulations. The geometry of each rubber frame was made out of 4 rectangular components that were merged and had a thickness of 4 mm. The load was applied by a Friedlander pressure-curve discussed in Section 2.2, where the parameters were calculated in MATLAB for the different experiments. In the cases where a Friedlander fit would provide inaccurate results, linear interpolation was used, as discussed in Section 4.2.3.

Table 7.1: Elastic material parameters for rubber and glass

	ρ [kg/m^3]	E [MPa]	ν
Rubber[1]	1400	2	0.46
Glass	2500 [12]	70000 [24]	0.23 [24]

Table 7.2: Friedlander parameters for FG-05-1

P_r [bar]	t_+ [ms]	b
62.74E-2	11.818	7.265E-1

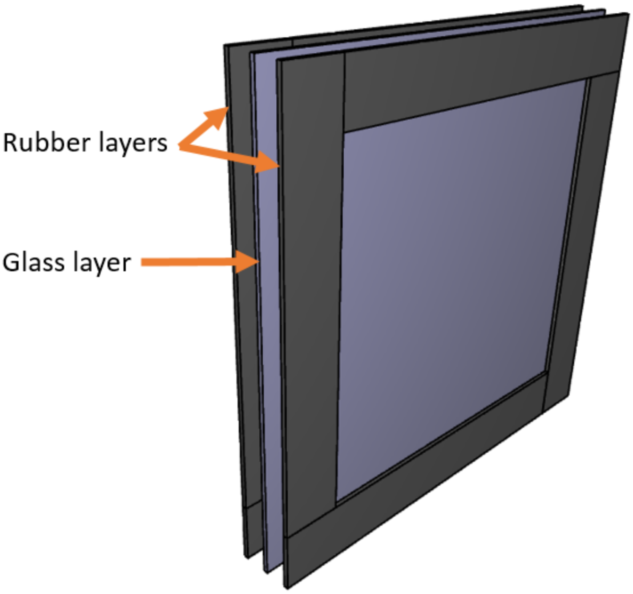

Figure 7.1: Model of the float glass experiment, modelled in IMPETUS

7.1.1 Elastic behaviour

Initially, the model was simulated without fracture criteria as a way to understand the boundary conditions. The model was given the material parameters presented in Table 7.1 and the load was modelled with a Friedlander curve with the parameters tabulated in Table 7.2. Both the glass and the rubber were modelled with 5×5mm hexahedron elements. The elements in the rubber was set to polynomial order 1 and the elements in the glass was set to polynomial order 3, see Figure 2.14. A parameter study was conducted to evaluate the effect of different Youngs' moduli in the rubber, and how the different values affected the

---

[1] Material parameters for rubber given from PhD Candidate Karoline Osnes

boundary conditions. The different Young's moduli used in the simulations were 1, 2, 3, 5 and 10 MPa. The results from the parameter study is shown in Figure 7.2. Experiment FG-05-1 was used as benchmark.

With E_{rubber} set to 2 MPa, the behaviour of the glass pane was too soft. With the increasing Youngs' modulus in the rubber, the response in the glass pane increased in stiffness and the displacements were reduced. The initial stiffness of rubbers subjected to loading and small strains, is as presented in 3.1.5 highly strain rate sensitive. Due to the high strain rate sensitivity, a Youngs' modulus of 5 MPa is plausible when the rubber is simplified with an elastic material model. Due to the best fit with the experimental results, E_{rubber} was set to 5 MPa. A standard model was defined to perform additional parameter studies, and the parameters chosen for the standard model is tabulated in Table 7.3.

Table 7.3: Parameters for the standard model

E_{rubber} [MPa]	Element type	Mesh size [mm]
5	Cubic hexahedron	5x5

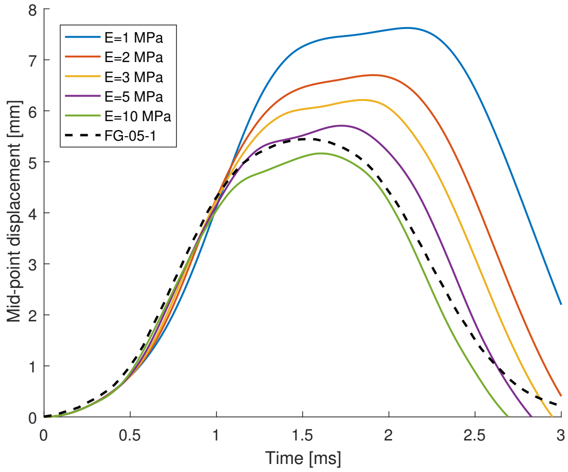

Figure 7.2: Response of different E-moduli for rubber. E = 5 MPa is set as the standard model

During the post processing of the simulations, the maximum strain of the rubber was found to be 0.035, which are sufficiently small for the elastic material model to be valid.

Polynomial element order

The polynomial element order was changed to see how the number of integration points in the elements affected the pre-failure elastic behaviour of the glass pane. An increase in the polynomial order of the elements was expected to decrease the stiffness of the glass pane as each element gets an increase in bending capability. As discussed in Section 2.8

hexahedron elements in IMPETUS may be linear, quadratic or cubic, and during this parameter study, the effect of the different orders was studied. From Figure 7.3 the resulting displacement-time curve is presented. Up to 1 ms, all simulations followed each other and the experimental test curve almost perfect. Reaching maximum displacement, the curves with polynomial order two and three showed similar behaviour, while order one had a different shape. As earlier mentioned, a first order element is not capable of describing bending adequately and may be the reason for the different contour. Even though the running time was increased, the authors wanted to use the most authentic model compare to experiment and decided to keep the 3rd order element for further studies.

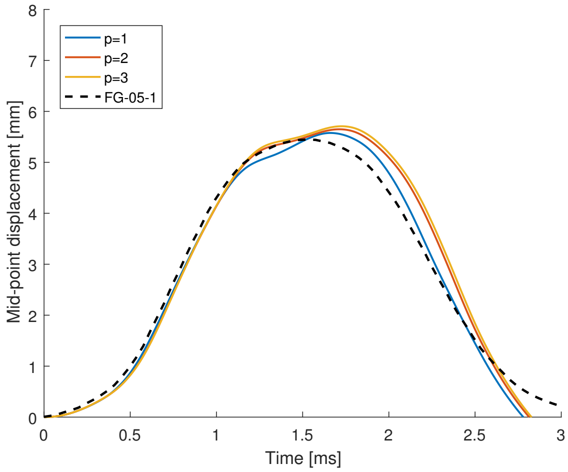

Figure 7.3: Effect of polynomial order of glass elements

7.1.2 Failure response

To enable fracture in the glass panes and simulation of the experiments that fractured, a fracture criterion was added to the glass material model. The same feature as in the modelling of four-point bending was used, *PROP_DAMAGE_BRITTLE. The parameters was the same as in 5.3, σ_c set to 47.47 MPa, K_c set to 23.72 MPa $\sqrt{mm}$ and node splitting was used at failure. A thorough parameter study was conducted, to see how different parameters affected the strength and failure pattern for the glass pane. Parameters investigated in this section are the element size, random initial damage in the glass and different type of elements. For each parameter study, the parameter in question was isolated and tested, while the remaining parameters were fixed.

As described in Section 2.4, the critical point for the initial crack is determined by the critical micro crack. In a blast situation, the maximum remote stress will be concentrated in the middle of the plate, which means that if a critical micro crack with maximum size occurs both in the middle and at the boundary of the glass, the result will be a crack initiation in the middle. Without any initial damage in the glass, the numerical model of the blast test will also have the initial crack close to the middle. Showed in Section 4.2.3, test FG-01 was the only float glass experiment that got the initial failure in the centre of the pane, so the numerical results will in this section be compared to this experiment. For the experiments that failed (ex. FG-01), the Friedlander curve does not describe the blast load in a satisfactory manner, as mentioned in Section 4.2.3. The blast load was thus modelled with a pressure-time curve given by Equation 4.3. The parameters used for the modelling of experiment FG-01 are tabulated in Table 7.4.

Table 7.4: Pressure curve parameters for FG-01

P_r [bar]	P_f [bar]	t_f [ms]
6.370E-1	5.433E-1	0.991

Element size

To see how the element size affected the strength and crack propagation, three different mesh sizes were simulated and compared. The simulations were run to $2ms$ to evaluate the crack propagation. The displacement curve was also compared to the experiment for additional control. Mesh sizes with corresponding NOE and running times are tabulated in Table 7.5.

Table 7.5: Different mesh sizes used in the parameter study

Element size [mm]	NOE	Running time
10 × 10	3000	5min 16s
5 × 5	7800	20min 51s
2 × 2	41400	3h 16min

The resulting graph from the study is presented in Figure 7.4. All of the numerical simulations displayed a larger initial mid-point displacement compared to the experiment, but after the point of fracture, the experimental model showed a faster-growing curve. As expected, all the numerical models had the same response before fracture as the elastic parameters were the same. After fracture, the models responded almost the same, but with some deviations. The model with the coarsest mesh of 10 × 10 mm resulted in the stiffest stiffest behaviour, while the 5 × 5 mm mesh gave the softest. This being said, all curves were more or less the same and showed a suitable curve fit around the experimental test

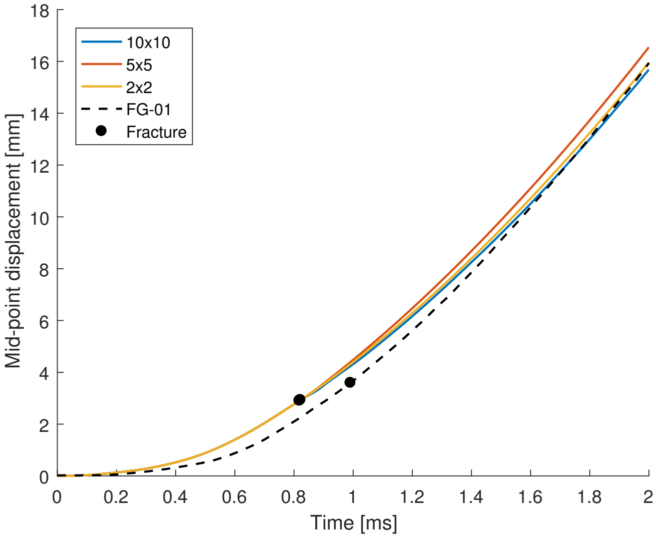

Figure 7.4: Parameter study of different mesh sizes compared to Test FG-01

In Figure 7.5, a visualization of the different crack propagations is shown. When compared, there are some significant qualitative differences between the results. The model with the coarsest mesh with 10×10 elements showed tendencies of crack propagation from the middle towards the corners. It does not capture the diagonal crack propagation from the centre to the corners. The model with mesh size 5×5 mm does capture the crack propagation towards the sides better, but are limited to only a few cracks compared to the experiment that had 20-30 to each side. It does not have any crack propagation towards the left top corner and does also miss the transverse cracks in the corners. The model with the finest mesh, 2×2 mm, has cracks towards all four corners. Although it does not have as many cracks as seen in the experiment, it shows a qualitatively good result. It also captures the transverse cracks in the corners. All meshes had the first crack propagation from the middle of the pane. In the case of this model with the loading modelled as described, the glass proved to be highly mesh sensitive when evaluating the crack propagation. The finer the mesh, the more realistic was the crack pattern. The mesh size did not affect the mid-point displacement significantly.

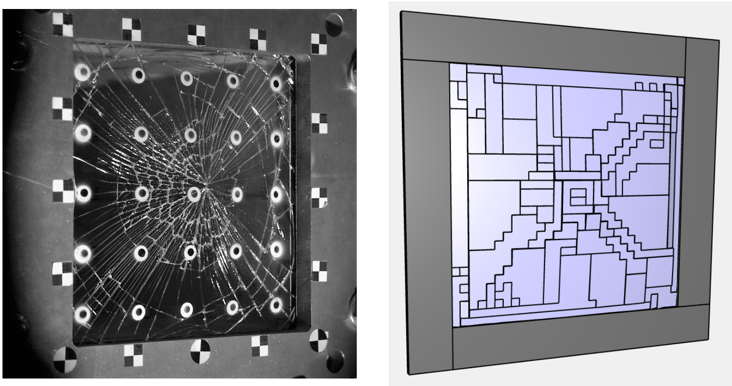

(a) Experiment FG-01

(b) 10×10

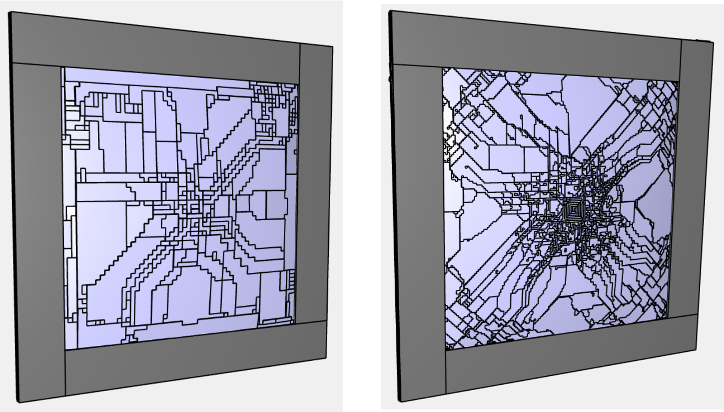

(c) 5×5

(d) 2×2

Figure 7.5: Crack propagation comparison between experiment FG-01 and the numerical model with use of hexahedron elements of different mesh sizes. $t = 2$ ms

Initial random surface damage

As earlier mentioned, the strength of glass plates is dependent on the size and location of the critical microcrack. In IMPETUS Afea Solver this brittle material property has been attempted included with the feature *INITIAL_DAMAGE_SURFACE_RANDOM. The feature contains some areas on the glass surface with initial non-zero damages. The distribution and magnitudes of the initial defects are distributed by a probability function with statistical parameters as input. For a more thorough description of the feature, see [42].

The *INITIAL_DAMAGE_SURFACE_RANDOM feature in IMPETUS requires Weibull parameters as input to describe the stochastic properties of the material. The Weibull parameters calculated in Section 4.1.2 was based on the component test conducted, and may thus not be valid in describing for the glass. Therefore, the Weibull parameters used in the study of this feature was adapted from Ilseng's masters thesis [22].

In the study of the feature, it was found to have no significant effect on either crack propagation or displacement curve for the tested inputs. The feature was thus not included in the remaining models for either the float or the laminated glass panes.

Element type

As presented in Section 2.8 there are several types of elements available in the solver. A sensitivity study was conducted to evaluate the impact of a change of element type. The element type tested was the pentahedron element. The pentahedron element was chosen to see how the strength and the crack propagation were affected by the increase of possible directions for the crack to develop. As illustrated in Figure 7.6 the crack may propagate in eight directions with the use of pentahedron elements, while it may only propagate in four different directions by utilizing the standard hexahedron elements. The authors suspected a more realistic recreation of the fracture pattern with the pentahedron element than with the standard hexahedron elements.

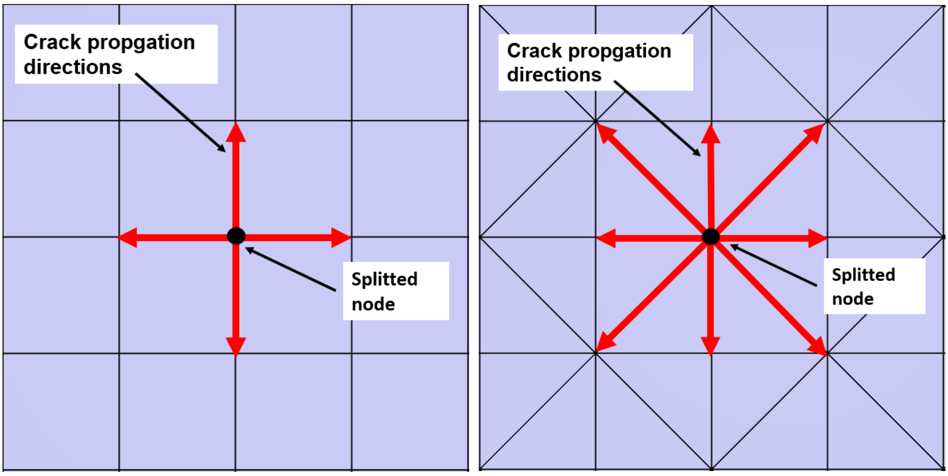

(a) Hexahedron elements **(b)** Pentahedron elements

Figure 7.6: Possible crack propagation directions with the different element types

The number of elements is doubled with the use of pentahedron elements as each hexahedron element is split into two pentahedron elements. Due to the increase of elements, the element size was increased in the sensitivity study. The elements tested had the sizes 20 × 20mm, 8 × 8mm and 4 × 4mm, where the lengths referred to are the shorter sides of the triangle. All the simulations run in the element type sensitivity study were run with one element in the thickness of the pane and polynomial order three. When analysing the results, the crack propagation and displacement function were analysed. The displacement functions from the different analyses are shown in Figure 7.7.

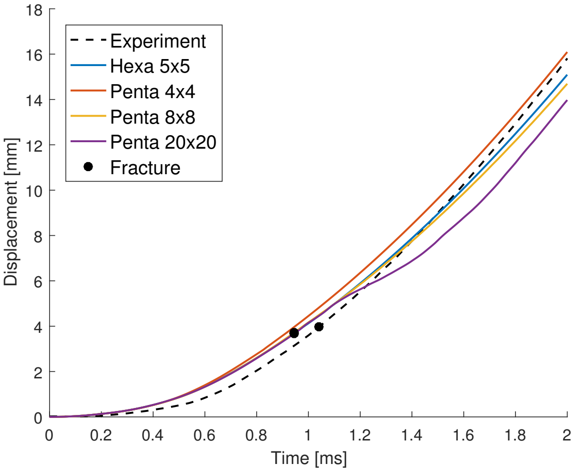

Figure 7.7: The effect of the pentahedron element with different element sizes

The element type accounts for minor changes in the displacement function where the shape of the curve and the magnitude of the displacements are the same. An exception is the analysis run with 20 × 20 mm elements, which are too big elements to capture the fracture of the glass properly. The NOE and the total running times were also affected by the change of element type. The running time and the NOE for each simulation is presented in Table 7.6

Table 7.6: Simulation data from the element type sensitivity study

Element type	Element size	NOE	Running time
Hexahedron	5 × 5mm	6408	20min 7sec
Pentahedron	4 × 4mm	20008	1h 25min
Pentahedron	8 × 8mm	5008	18min 33sec
Pentahedron	20 × 20mm	808	5min 27sec

The crack propagation in all of the simulations are shown in Figures D.1, D.2, D.3 and D.4 in Appendix D and a comparison between pentahedron and hexahedron elements is shown in Figure 7.8. It may be seen that the pentahedron elements can describe the cracks in the experiment in a better way. As in the mesh sensitivity study, smaller elements enables crack propagation in a more realistic manner than the larger elements. As seen in Appendix D, the model with 20 × 20 mm elements looks unrealistic, while the model with 4 × 4 mm elements describes the crack propagation with a better accuracy. As seen in Figure 7.7 the simulations with both hexahedron and pentahedron elements fracture at approximately the same time, and follows the same displacement function.

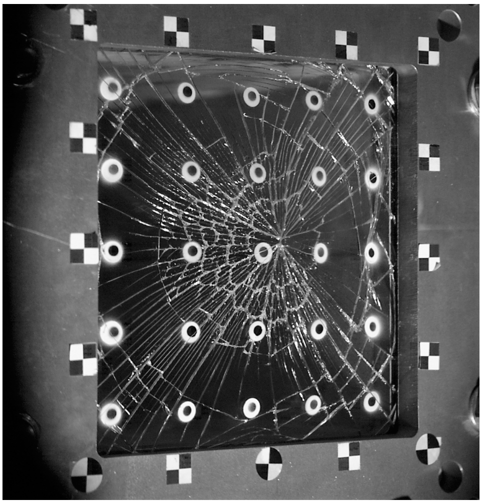

(a) Experiment

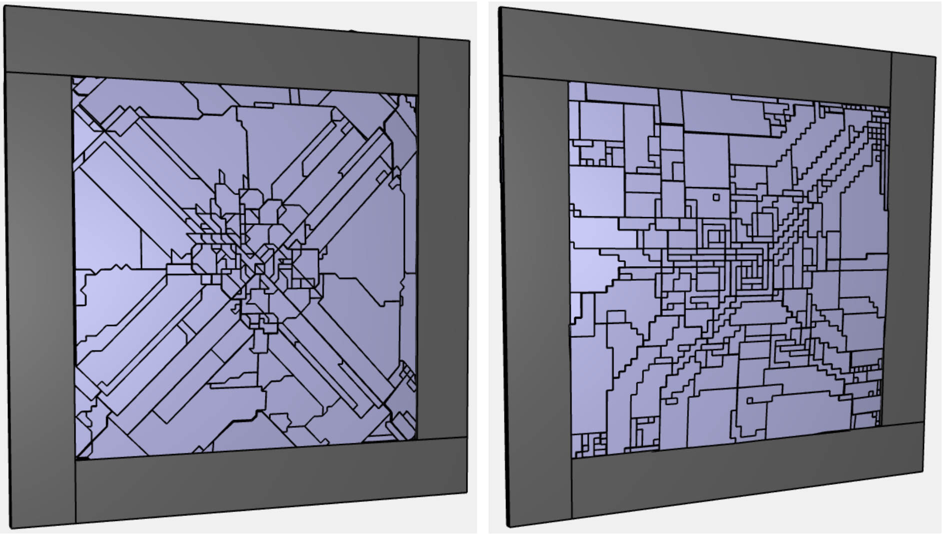

(b) Pentahedron elements 4×4mm

(c) Hexahedron elements 5×5mm

Figure 7.8: Crack propagation in simulations with different types of elements compared to FG-01

As a result of the mesh sensitivity and element type study, the pentahedron elements were found by the authors to give the best results when compared to experiment FG-01. It has to be emphasised that the blast simulations conducted on float glass have only been compared to one experiment. The other tests conducted during the work of this thesis gave different results, and as mentioned initially, FG-01 was chosen due to the initial failure in the middle of the glass. There are no guarantees that the same parameters and element types found best for FG-01 can recreate the corresponding behaviour of the other experiments conducted. Extra parameter studies may be necessary to fit the parameters to the remaining experiments.

Two simulations were run with longer total times to compare the fragmentation in the simulations with the fragmentation of the glass in the experiment. The standard glass pane, with fracture criteria and 5×5mm hexahedron elements and a model with 4×4mm pentahedron elements were run to a total time of 12ms. These are the same simulations as depicted in Figures 7.8b and 7.8c but with the increased simulation time. Another goal of the study was to calculate the fragment velocities after the complete failure of the glass and compare the results with the measured fragment velocities in experiment FG-01. As presented in section 4.2.3 the fragment velocity in experiment FG-01 was estimated to 23.441 m/s after failure of the pane. From the simulations, it was found that the fragment velocity in the simulation with 5×5 mm hexahedron elements was 24.62 m/s and the fragment velocity in the simulation with 4×4 mm pentahedron elements was 25.36 m/s. With the measurement errors and calculation inaccuracies taken into account, the results were deemed as good. The post-failure response in the glass in both simulations was studied and compared to the experiment at the same time after the blast. The results are shown in Figure 7.9 and 7.10.

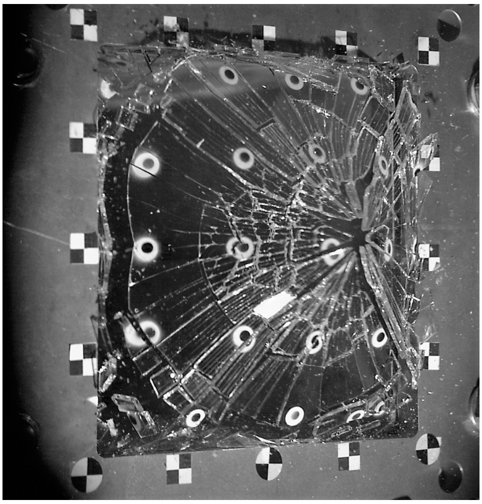

(a) Experiment

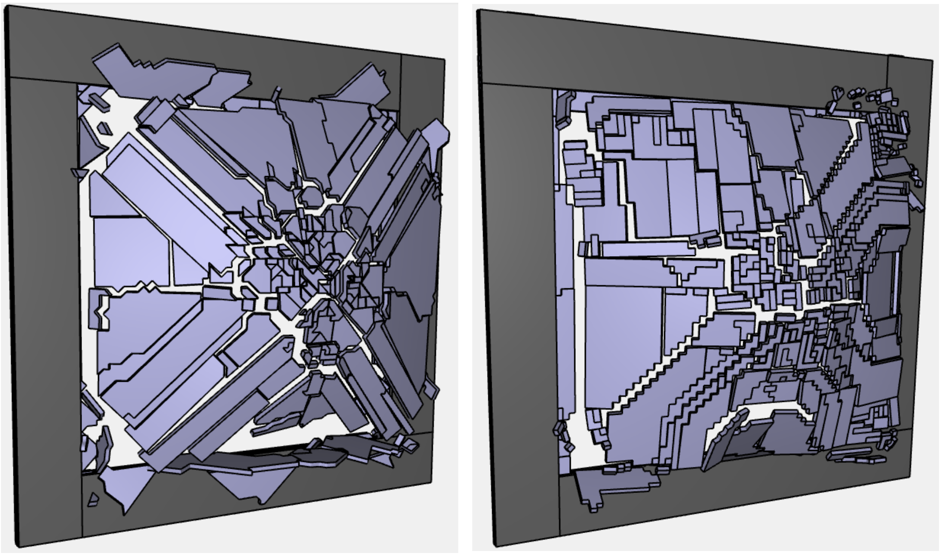

(b) Pentahedron elements 4×4mm

(c) Hexahedron elements 5×5mm

Figure 7.9: Comparison of the fragmentation of the glass 6.62 ms after the experiment and simulations at the same time

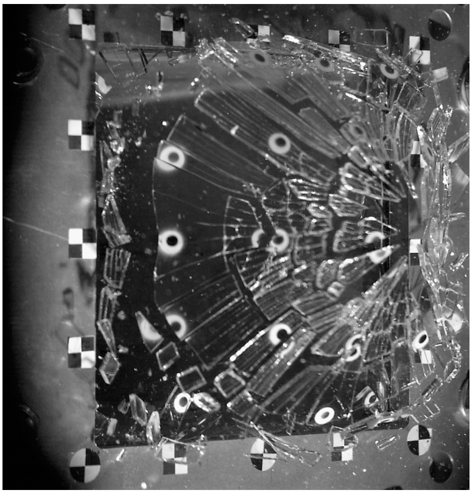

(a) Experiment

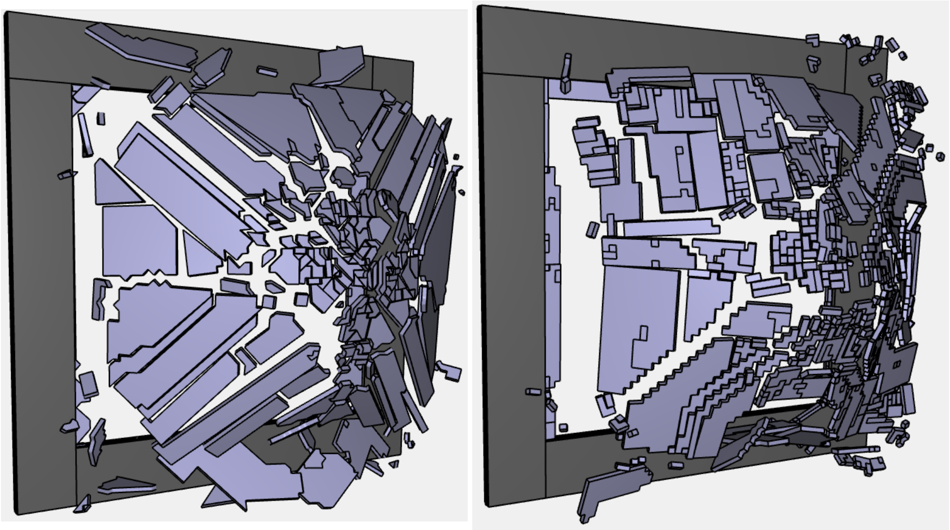

(b) Pentahedron elements 4×4mm

(c) Hexahedron elements 5×5mm

Figure 7.10: Comparison of the fragmentation of the experiment 9.84 ms after the blast and simulations at the same time

As seen in the Figures 7.9 and 7.10 the pentahedron elements gave a better representation of the crack propagation and acceleration of the glass fragments out of the frame than the hexahedron. With the hexahedron elements, the cracks have only four different ways to propagate, and this results in the serrated shape of the cracks seen in 7.10c. The serrated edges require more energy to propagate than the smooth edges. The glass panes tested had all smooth edges after failure, and thus the pentahedron elements were chosen as the most favourable choice.

7.1.3 Summary and discussion

In Section 7.1, simulations with modelled float glass have been run with two different blast loads as an attempt to recreate the behaviour recorded in the experiments presented in Section 4.2.3. The elastic response before fracture and the post-fracture response in the glass pane have been studied separately to investigate different aspects of float glass simulations. In the pre-fracure part, the aspects investigated were the boundary conditions, polynomial order of the glass elements and Young's modulus in the rubber. In the post-fracture investigation, the focus of the parameter study was element size, element type and fragmentation of the glass after breakage. The goal of the numerical modelling was to find parameters and ways of modelling to enable simulation of a glass pane subjected to a blast load.

In the elastic material modelling, the simulations were run with only elastic material properties to investigate the significance of the rubber boundary conditions and the polynomial order of the elements. This was helpful in deciding how the glass pane should be modelled to best coincide with the response recorded with DIC. The E-modulus of float glass was not changed in the parameter study as the value was assumed known. It was found that the Young' modulus for the rubber was of great importance concerning the boundary conditions and the stiffness of the window system. The polynomial order of the elements was of less significance in the elastic domain of the response but was considered to be more important when modelling with a fracture criterion. Thus the polynomial order of three was chosen.

The parameters found in the elastic material part were utilised in the simulations of the panes with fracture criteria included. Experiment FG-01 was the only glass pane with the initial fracture in the centre, which made it the favourable choice for comparison with the simulations. The effect of different element sizes was studied with attention on crack propagation and similarity with the images taken during the experiment. Pentahedron elements were found to be the most fitting element type due to the increased number of possible crack propagation directions. The element size was found to be of great importance to enable the crack propagation similar to the one found in the experiments. With the use of hexahedron elements, an unrealistic amount of energy was needed for the crack to propagate in the diagonal directions from the centre, and the crack shape ended up serrated. For design purposes, the fragmentation was studied, and the fragment velocity after breakage was calculated. The results were within good when compared to the fragment velocities calculated from the experiments. In the fragmentation study, the pentahedron elements showed the highest level of similarity when compared to the experiment images. The failure criterion used were the same as the ones utilised in the simulation of the four-point bending tests.

It is emphasised that the results from the numerical simulations conducted on the float glass panes have only been compared to a single experiment and there are no guarantees that the model can recreate the behaviour of other experiments. Based on the experiences at SIMLab at NTNU, glass panes fracture in different ways and at different loads and displacements due to the shape and location of micro-cracks in the glass. Uncertainties in the experimental setup do also affect the outcome. This impedes the validation of a single model when compared to different experiments.

7.2 Laminated Glass

As for modelling of the float glass experiments, a preliminary numerical study on the numerical model of the laminated glass was done. Laminated safety glass is more complex than modelling a single glass pane, and the experiences gained in the float glass section were used as a place to start. Additionally to the mesh sensitivity, boundary conditions, element type and initial surface damage, the PVB-glass connection and modelling are of great importance. As discussed in Section 3.1.4, the delamination properties of the laminated glass plays a significant role in energy absorption and post-fracture behaviour of laminated glass. From the simulations run on float glass, the boundary conditions, element size, element type and element polynomial order were chosen. The rubber was modelled using 5×5 mm cubic hexahedron elements, and the glass panes were modelled using 4×4 mm pentahedron elements. During the numerical modelling of the laminated glass pane, several parameters and features regarding the glass-PVB interaction in IMPETUS were studied. This interaction was the main focus of this section, as the glass parameters were studied in Section 7.1. The numerical model of the laminated glass window is shown in Figure 7.11. Spacing has been added between the layers for visual effects. The layers in the model are in contact with a numerical tolerance of 10^{-6}mm.

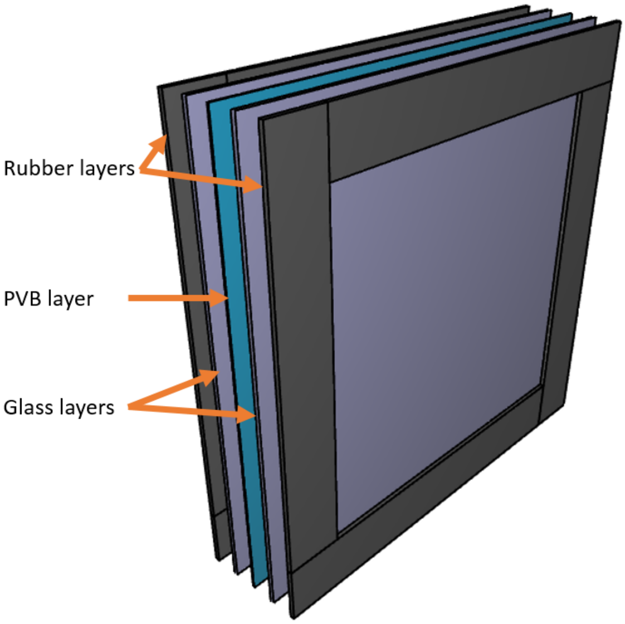

Figure 7.11: Numerical model of the laminated glass modelled in IMPETUS

7.2.1 Standard model

Initially, a standard model of the laminated glass was established based on the results of the float glass parameter study, the PVB tensile test (Chapter 6) and the experiences gathered when modelling the four-point bending test (Chapter 5). The thickness of the glass panes and the PVB-layer was calculated based on the measurements conducted prior to the blast tests and set to 3.8mm for the glass and 1.52mm for the PVB-layer. The dimensions of the glass and rubber were the same as for the float glass, 400×400 mm. The load was applied with a corresponding Friedlander fit calculated in Section 4.2.3 and tabulated in table 4.13. The DIC data and Friedlander parameters from LG-01-2 were chosen for comparison in the preliminary study because the pane did not fracture. In the preliminary study, the pre-fracture behaviour of the laminated glass pane was studied to verify the boundary conditions found when simulating float glass. In the standard model, the contact surfaces between the PVB and glass panes were merged using the standard *MERGE function in IMPETUS (with the PVB layer as slave part). The boundary conditions were the same as in the float glass simulations, i.e. the outer sides of the rubber were fixed. The materials were given elastic material properties only. By trial and error approach the parameters producing the best fit compared to test LG-01-2 was found. Some key parameters are tabulated in Table 7.7. The simulations were run with an end time of 2.5 ms, and the time-displacement curve for the standard model and test LG-01-2 is shown in Figure 7.12.

Table 7.7: The resulting standard model parameters found in the preliminary study

Material	E-modulus	ν	Density	Element type/size	P-order
Glass	70 000 MPa	0.23	2500 kg/m^3	Pentahedron 4×4 mm	3
PVB	8 MPa	0.45	1100 kg/m^3	Hexahedron 4×4 mm	3
Rubber	150 MPa	0.46	1400 kg/m^3	Hexahedron 10×10 mm	1

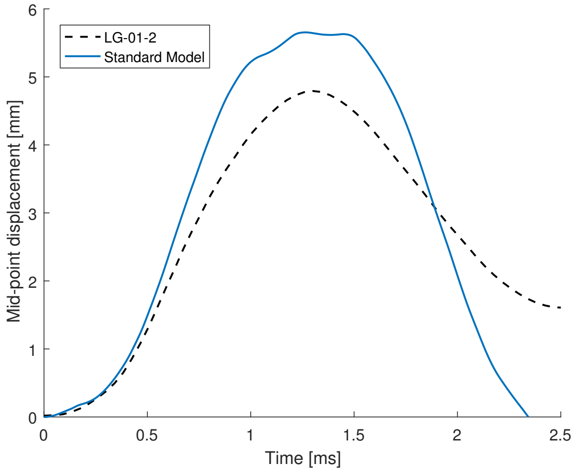

Figure 7.12: Comparison between experiment LG-01-2 and the simulation of the standard model

The Young's modulus of the rubber had to be changed significantly from the float glass tests to the laminated glass tests due to a too soft behaviour of the boundary conditions. In the post processing of the simulation of the standard model, the glass was observed moving too freely in the rubber clamping, changing the boundary conditions from clamped to almost simply supported. Simulations were run both with and without the *MERGE between rubber and glass. In the simulations run without the *MERGE criteria, the glass moved in the face plane relatively to the rubber, which was unrealistic. In the simulations run with the same Young's modulus for the rubber as in the float glass simulations, the mid-point displacement was recorded to be close to twice as big as in the experiment. When increasing the Young's modulus for the rubber, the authors noticed a reduction in mid-point displacement and thus a behaviour more alike the one recorded during the tests. As mentioned in Section 7.1, the behaviour of rubber at high strain rates is hard to predict, and the higher the strain rate, the stiffer is the behaviour [48]. The strain rate in the rubber during the laminated glass simulation was found to be as high as 200 s^{-1}. By studying the initial stiffness of the rubber at high strain rates in [48], it may be argued that Young's modulus of 150 MPa is within reason. Additionally to Young's modulus, the Poisson ratio was studied. A parameter study was run with ν varying from 0.4 to 4.9 without any significant change in the displacement curve. There were some slight variations but no clear tendency towards a stiffer or softer behaviour of the boundary conditions.

Models with the PVB modelled with the The Bergström-Boyce material model was created to study the effect of the PVB material model. Unfortunately, the The Bergström-Boyce model was too complex to be used in a blast simulation, and the simulation failed to start running. Therefore, the PVB was modelled only with elastic material properties.

As mentioned, experiment LG-01-2 was used for comparison when finding the elastic parameters and boundary conditions. With the parameters found for the standard model, rest of the laminated glass experiments were simulated for an additional comparison and verification of the laminated glass model. The simulations of the other panes had the same input as the standard model, but the Friedlander parameters were changed to the ones calculated for each experiment respectively. The Friedlander parameters used are tabulated in Table 4.13. The results from the simulations are plotted with the respective experiments in Figure 7.13

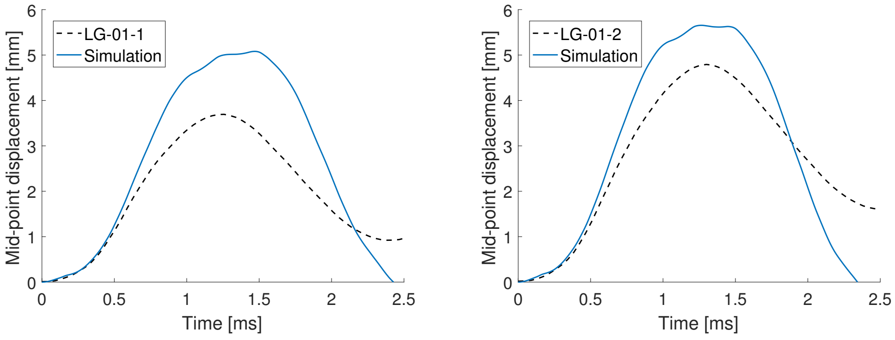

(a) LG-01-1 **(b)** LG-01-2

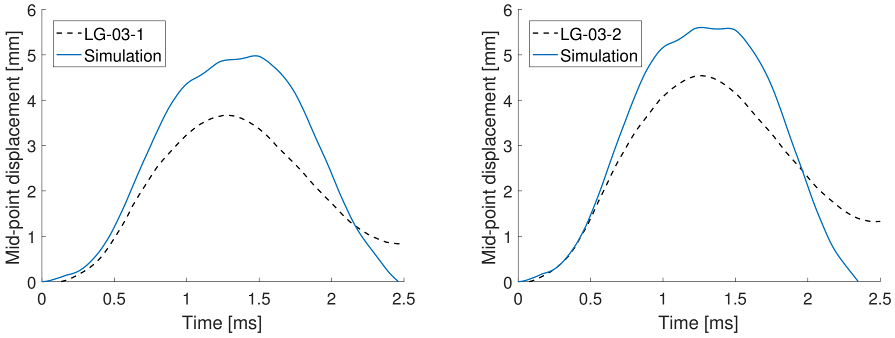

(c) LG-03-1 **(d)** LG-03-2

Figure 7.13: Comparison of the simulations and experiments when modelled with elastic material properties

As seen, all the simulations showed a lower stiffness and bigger mid-point displacement than the experiments. Additionally, the simulations with elastic material parameters failed to capture the permanent experimental mid-point displacement. All the experimental results showed a displacement larger than zero at t=2.5 ms while the simulations had a displacement equal to zero or in some cases below zero at this time. If the laminated glass panes tested had responded like a perfectly elastic material, the displacement after the blast should have been zero. The permanent deformation in the experiment may indicates that either the rubber is simplified too much or that the steel plate clamping the specimen has moved during the test.

7.2.2 Fracture criterion

A fracture criterion was added to the glass material model to enable the simulation of the glass panes that fractured. The fracture criterion was the same as used in the simulation of float glass, with σ_{max}=47.47 MPa, K_c=23.72 MPa$\sqrt{mm}$ and node splitting as erode method. To compare the simulations, a laminated glass that fractured during the experiment had to be chosen as benchmark, and LG-03-3 was chosen because this was the experiment with the highest recorded loading pressure. With the fracture of the glass, the authors expected the material parameters of the PVB interlayer to dominate the behaviour because the fractured glass would not contribute to any significant stiffness. Thus the PVB was the main focus in the preliminary simulations run with a fracture criteria in the glass. To capture the post-fracture behaviour of the PVB, the simulation time was increased to 10 ms. At 10 ms after the blast, the mid-point displacement in the experiment had stabilized around a value of 90 mm, thus making it a natural time to end the simulation. For comparison, the mid-point displacement and crack propagation during the blast were set as control parameters.

The first simulations were run with PVB as an elastic material with only Young's modulus, density and Poisson ratio as input parameters. A parameter study was done on Young's modulus to see how it affected the post-fracture behaviour. With its elastic material parameters, the PVB was expected to behave in a rubbery way with no permanent deformation. It was anticipated that the fractured glass would prevent the PVB to recover back to the initial state, but with elastic material parameters only, the effect was expected to be small. The different Young's moduli for PVB tested in the elastic material study was 8, 50 and 100 MPa. The mid-point deflection as a function of time for each simulation and the experiment is plotted in Figure 7.14

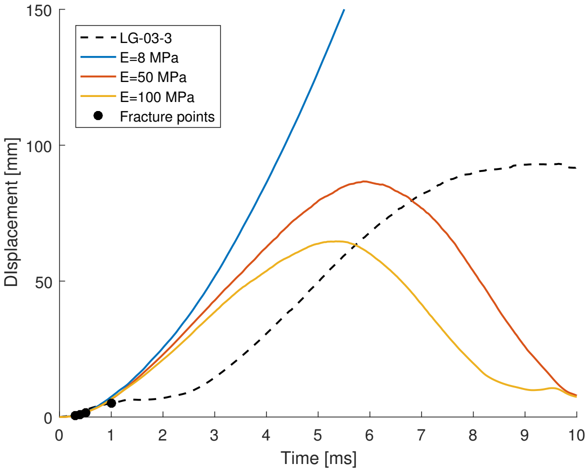

Figure 7.14: Effect of different Young's moduli in the PVB inter-layer

As seen in the Figure, the elastic material model was not able to capture the permanent displacement observed in the experiment. The fractured glass did not prevent the retraction of the PVB as expected from the experimental results. The displacement returned to zero after the blast, signifying that the PVB was allowed to respond perfectly elastic. The window tested in the experiment, on the other hand, ended up with a permanent displacement of approximately 90 mm after the blast. Since the PVB eventually would have shrunk back to its initial state without the glass, the permanent displacement recorded is believed to be caused by the retaining glass fragments holding the contraction back. The

PVB might use The simulation with E_{pvb}=8 MPa ended up with a max displacement of 360 mm, but the plot window was set as is for a better visual presentation. Based on the simulations with elastic PVB material properties, Young's modulus of 50 MPa was chosen for the PVB. The crack propagation in the simulation differed somehow from the images taken during the experiment. Figure 7.15 shows the crack propagating in the simulation compared to the experiment LG-03-3. As seen in the Figures, the crack in the simulation is initiated on the edges of the pane, while the initiation observed in the experiment was in the middle. The reason for the discrepancy is to the authors' knowledge unknown, and different measures were tried without success to achieve crack propagation from the centre. A possible reason may be the boundary conditions and the merging between the rubber and glass which may cause unrealistic internal stresses. At $t = 1.2$ms the crack propagation in the simulation resembles the experiment while at $t = 3.6$ms most of the glass nodes have been split and the glass fragments in the simulation have become small compared to the experiment. When comparing the crack propagation with the displacement curve, it may seem that the complete failure in the simulation happens at an earlier stage of the response than in the experiment and thus the mid-point deflection increases earlier in the simulation than in the experiment. This supports the belief that the elastic PVB material model is not able to describe the correct response.

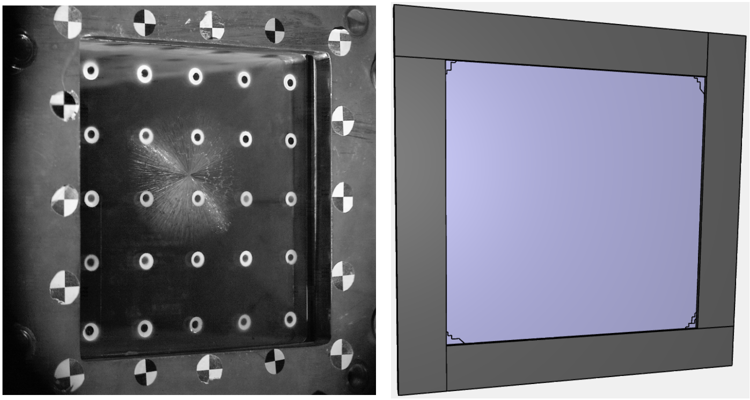

(a) t=0.0ms

(b) t=0.0ms

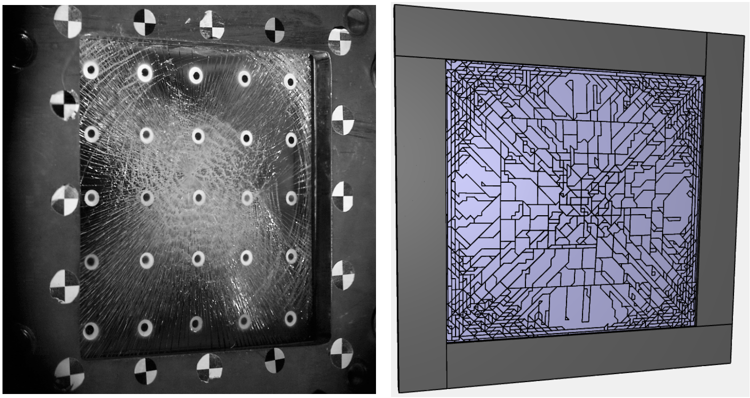

(c) t=1.2ms

(d) t=1.2ms

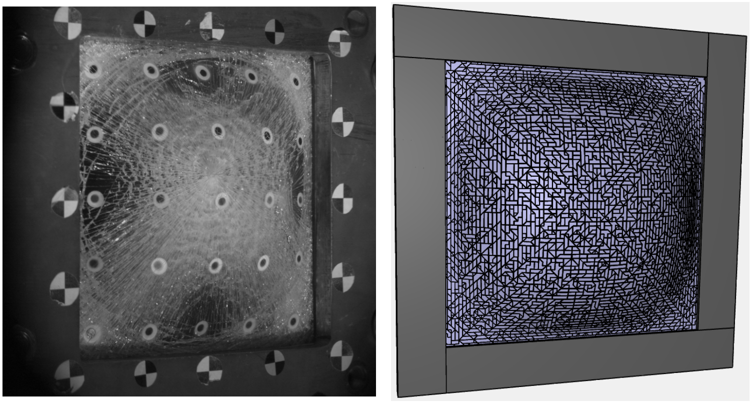

(e) t=3.6ms

(f) t=3.6ms

Figure 7.15: Crack propagation in the simulation compared to the crack propagation in experiment LG-03-3. t=0.0 is the time of the first visible crack

A study on the effect of the element type in the PVB was done to see how the element type affected the displacement curve, crack propagation and running time. The two elements tried in the study was the standard hexahedron 4×4mm and a 4×4mm pentahedron element. For the standard model, the PVB did not have a fracture criteria, and the element type was thus not expected to affect the crack propagation or displacement curve significantly. With the decrease in the number hexahedron elements, the running time was expected to increase. In contrast, the running time with pentahedron elements was shorter than with the hexahedron elements, and the crack propagation differed significantly with the use of hexahedron elements, as seen in Figure 7.16. The displacement curve was also affected by the change in PVB element type. The stiffness of the window system with hexahedron elements in the PVB was higher than when modelled with pentahedron elements. This may be due to the change in fracture pattern and the less energy consuming crack propagation during the blast.

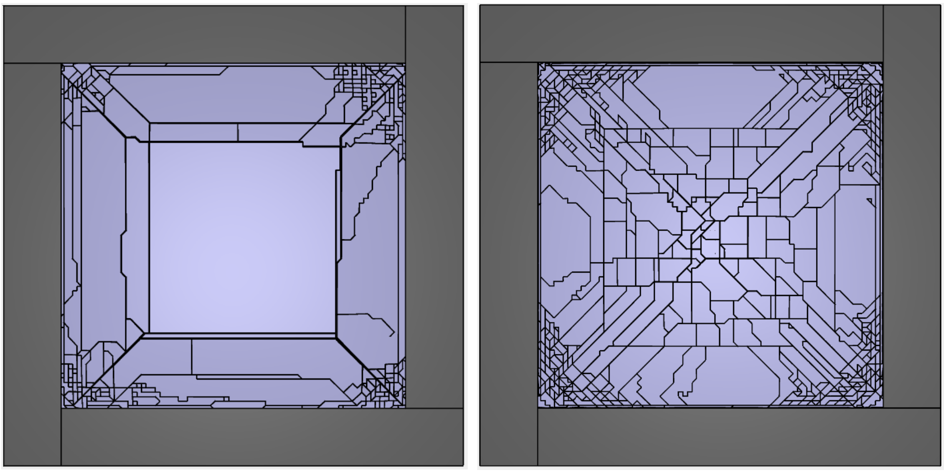

(a) Hexahedron 4×4 mm

(b) Pentahedron 4×4 mm

Figure 7.16: Comparison of the crack propagation with different element types in the PVB interlayer

Cohesive failure criteria

An attempt was made to include the properties of delamination to the model. This was done by including a failure criterion to the merging between the glass panes and the PVB. 4×4 mm pentahedron elements were used in both the glass and PVB. As presented in Section 3.2.4 this was recently implemented in IMPETUS with the command *MERGE_FAILURE_COHESIVE, see Section 3.2.4. During the deformation of the laminated glass windows in the blast experiments, the glass fractures and to some degree loosens from the PVB. This enables local strains in the PVB.

With the regular *MERGE function in IMPETUS, the PVB elements are merged with the glass elements, and the glass elements cannot loosen from the PVB layer. The *MERGE_FAILURE_COHESIVE feature allows the glass elements to loosen completely, or to some degree, from the PVB, which resembles the delamination seen in the experiments. With the Young's modulus for the PVB found in the previous section, simulations were run to compare the effect of the new feature. Three simulations were compared, the one without the additional feature from previous Section with use of E_{PVB}=50 MPa, shown in Figure 7.14, and two simulations with different parameters. The parameters tested in the first simulation were suggested by Lars Olovsson, a developer at IMPETUS Afea [42] (Test 1), and the second combination of parameters was calculated based on the equations in Section 2.4 and values found in a paper by Yankelevsky [12] (Test 2). The parameters tested are tabulated in Table 7.8. With the failure criteria included in the merging feature, the glass was expected to loosen from the PVB, and an increase in fragments was expected.

Table 7.8: Parameters used in the study of *MERGE_FAILURE_COHESIVE

Simulation	σ_{fail}	τ_{fail}	G_I	G_{II}	Δ_{ref}
Test 1	10 MPa	10 MPa	1 MPa mm	1 MPa mm	0
Test 2	10 MPa	10 MPa	0.00804 MPa mm	0.0 MPa mm	0

As expected, there was an increase in the fragmentation of the glass, see Figure 7.18. Some glass fragments loosened from the PVB during test 1, while nearly all the glass elements loosened in test 2. The displacement curves of the simulations also differed from identical simulations without the cohesive failure criteria activated. As seen in Figure 7.17 the glass pane had an increase in maximum displacement during the simulation. Additionally, the deflection at the end of the simulation was larger in the simulations with failure criteria than the simulations run without the feature. This may be due to loose or deformed glass elements preventing the PVB from completely retracting after the initial deformation. As seen in 7.17, the test run with the lowest failure criteria, test 2, experience the highest displacement. This may be caused by the number of elements loosening from the PVB. In Figure 7.18 the deformed windows at maximum displacement are shown for a comparison of the glass fragmentation. It can be seen that almost all the glass elements in the glass have loosened in test 2, while in test 1, most of the glass elements remain fastened to the PVB.

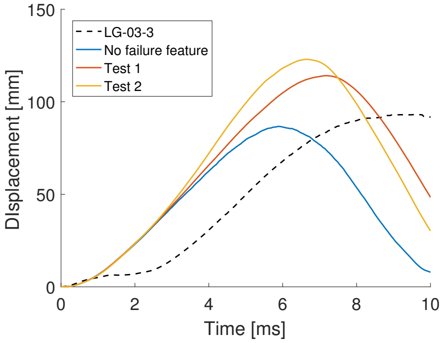

Figure 7.17: Effect of cohesive failure criterion on mid-point displacement curve

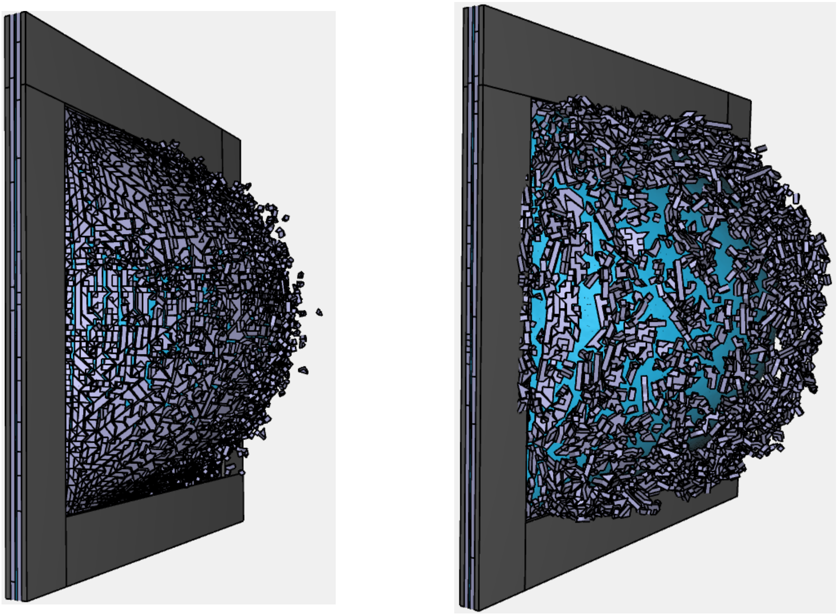

(a) Test 1 **(b)** Test 2

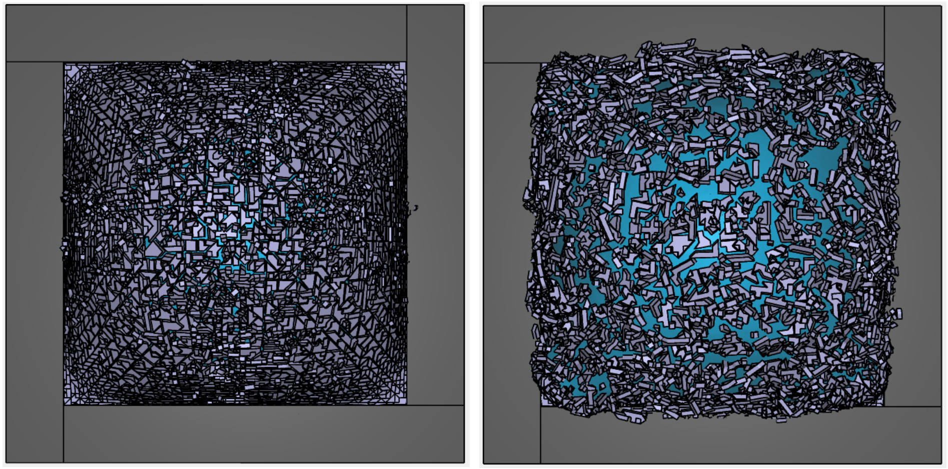

(c) Test 1 **(d)** Test 2

Figure 7.18: Fragmentation for Test 1 and 2 seen from two different angles at the time of maximum displacement

With the cohesive failure criterion included in the simulations and with the relatively small elements, the running time increased drastically. In the two last simulations, the running times were 27h 24min and 25h 23min respectively. Due to the time limitations of the study, the feature was not studied further.

By tracking the displacement of the elements that loosened from the PVB, an estimate of the fragment velocities was calculated based on the average velocity in ten fragments.The mean velocity was calculated from the time the elements loosened from the PVB to the end of the simulation. The calculated average fragment velocity was $17.172 m/s$ in simulation *test 1*. In the experiments, no fragment velocity was calculated because the glass fragments that loosened from the window was too small for the DIC to track. Thus no comparison is possible.

As done with the experimental results, the strain rate in the PVB was studied for comparison. *Test 1* from the study of cohesive failure was deemed as the best model at simulating the experiments. The PVB strain rate was thus studied for this simulation. An area with elements was selected in IMPETUS to compare with the selected subsets used in the calculation of strain rate in Section 4.2.3. The strain rate was calculated by numerically differentiating the average strain in a selected area of elements in the centre of the PVB. The selected area of elements is shown in Figure 7.19 next to the results in the form of a curve showing the effective strain rate as a function of time. An attempt was made to export the strain rates directly from IMPETUS, but due to an unknown error the results were unrealistically high and are thus excluded from the thesis.

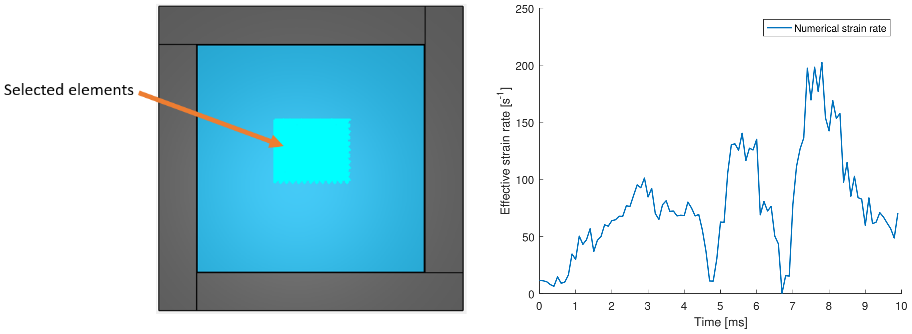

(a) Selected elements in the PVB

(b) Strain rates during the simulation

Figure 7.19: (a) The selected elements used in the comparison of strain rates and (b) the strain rate average in the selected elements during the simulation

The shape of the strain rate curve differs from the experimental strain rates estimated and shown in Figure 4.25b, but the order of magnitude of the strain rates coincide. The reason for the discrepancy in shape is to unknown, but may be due to inaccurate calculations in section 4.2.3, incorrect material modelling of the PVB or a combination of both.

The model used in *Test 1* was then used to simulate the other laminated glass panes that fractured in the experiments. The Friedlander parameters for the blast load was changed to match the respective experimental data, but the rest of the model remained unchanged. The experiments that were simulated additionally to LG-3-3, was LG-02-1 and LG-04-1. The results of the two simulations in the form of displacement curves are shown in Figure 7.20

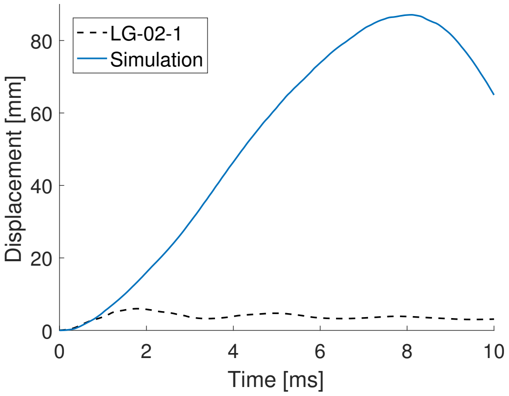

(a) Experiment LG-02

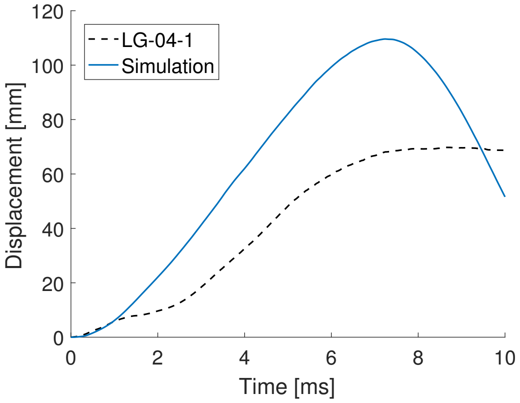

(b) Experiment LG-04

Figure 7.20: Comparisons between the recorded data from the experiments and the simulations with the same applied pressure load.

As seen, the difference between the simulation and experiment is significant for LG-02. In experiment LG-02 it was noted that only one of the two glass panes of the laminated glass fractured. This may be seen in Figure 4.22a. In the simulation of experiment LG-02 both the glasses fractured completely, and this is the main reason for the discrepancy. As seen in Figure 4.21c, the displacement curve for LG-02 resembles the curves for the specimens that did not fracture more than the ones that fractured. For the PVB to be activated, both the glass panes have to fracture. Figures 7.21, 7.22 and 7.23 shows the fracture of the windows at maximum displacement for both the simulations and the experiments. The script used to model the laminated glass windows subjected to blast load is attached in Appendix E.

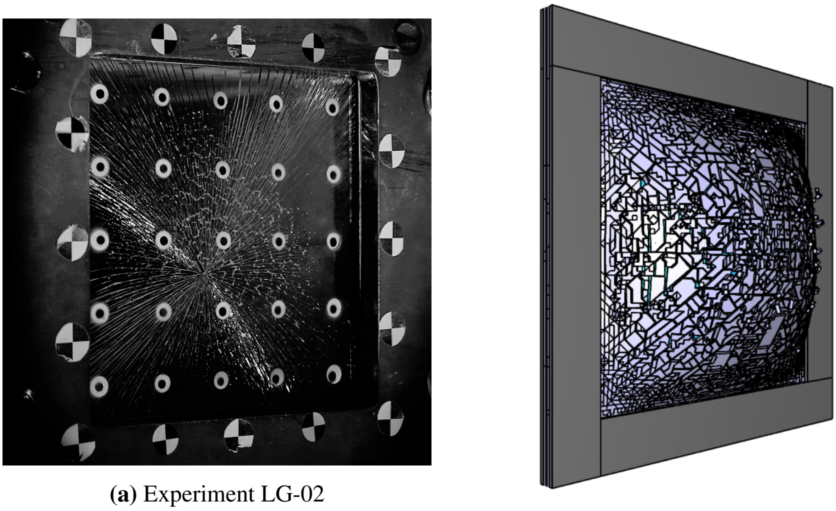

(a) Experiment LG-02

(b) Simulation

Figure 7.21: Fracture of the glass at maximum displacement in both the experiment and simulation

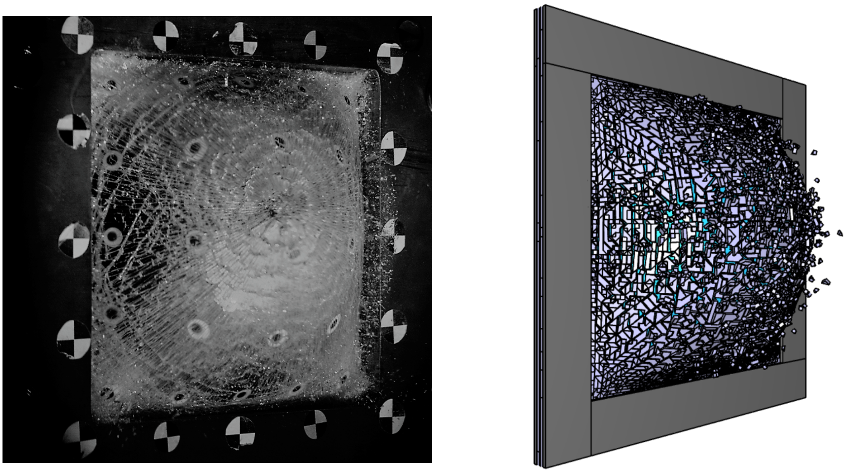

(a) Experiment LG-03-3

(b) Simulation

Figure 7.22: Fracture of the glass at maximum displacement in both the experiment and simulation

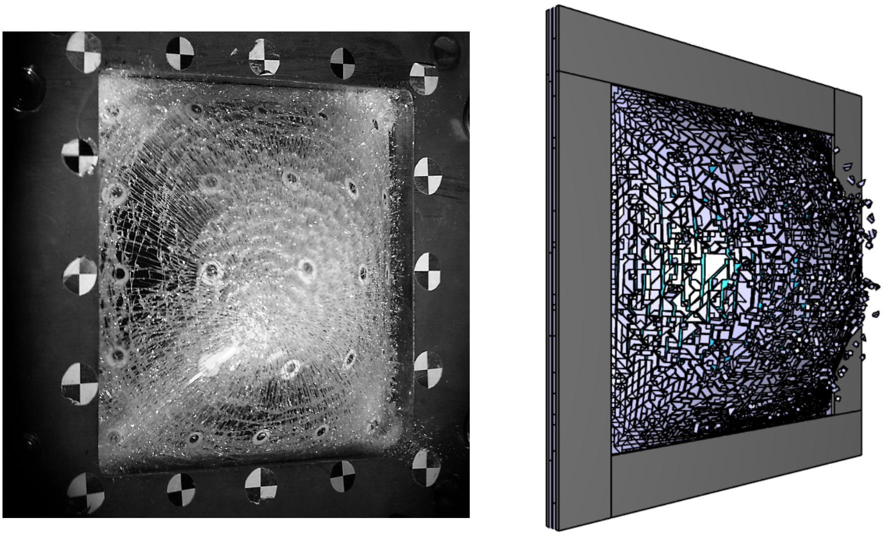

(a) Experiment LG-04

(b) Simulation

Figure 7.23: Fracture of the glass at maximum displacement in both the experiment and simulation

7.3 Summary and discussion

Laminated glass panes have been simulated in a blast load situation and compared to experiments conducted in the SIMLab shock tube facilities. The simulations were divided into two main studies, the response of the glass before fracture and the post-fracture response. In the study of the pre-fracture response, a parameter study was conducted to verify the boundary conditions and investigate the material properties of the PVB layer. The interaction between the PVB layer and the glass panes was also studied. In the post-fracture investigations, the focus of the parameter study was the response in the laminated glass after fracture. Special considerations were how the PVB behaved, and the crack propagation in the glass. The simulations were then compared to the experimental results.

In the pre-fracture modelling part, the boundary conditions was studied. Based on the findings in Section 7.1, the Youngs modulus of the rubber and the interaction between rubber and glass were assumed found. With the increased loading pressure and stiffness of the window, the rubber was found to respond softer than in the simulations run with float glass only. This emphasises the difficulties of modelling rubber at high strain rates. In the simulations with the low Young's modulus in the rubber, it was found that the laminated glass moved more than expected and thus changing the boundary conditions. The rubber was found too soft. As a countermeasure, the Young's modulus of the rubber was increased. This may have caused unrealistic stresses in the glass area close to the rubber and may be the reason for the glass failing in the edges. As argued in Section 7.2.1, the initial stiffness in rubbers at high strain rates and small strains vary significantly [48] and thus Young's modulus of 150 MPa may be valid for these purposes. It is emphasised that the rubber should be modelled with a more complex material model for more accurate results, but in this thesis, the rubber was not the main focus. In the elastic material part of the simulations the merging between the PVB and glass was done with the *MERGE function in IMPETUS, and as discussed the *MERGE between the rubber and glass was a necessity to prevent unrealistic relative displacement of the glass in the rubber.

Based on the findings in the pre-fracture simulations, simulations with higher loading pressure and increased total time were run. In these simulations, a fracture criterion was added to the glass material model. In this study, the specimen with the highest loading pressure was used for comparison, and the Friedlander parameters calculated in Section 4.2.3 were used as loading. Further out in the study, a failure criterion was added to the *MERGE feature between the PVB and glass to enable delamination of the glass and allow for small fragments to loosen from the interlayer during the blast. This gave good results, and the deformation and fragmentation showed some resemblance to the images captured during the experiment. As a result of long running times and the time limitations of the thesis, no further studies on different PVB material models were conducted. As seen in e.g Figure 7.17 the elastic material model is not able to capture the permanent deformation in the PVB. In the experiments the laminated glass windows deformed permanently due to fragmented glass preventing the PVB to retract.

It is emphasised that results from simulations have to be interpreted with caution. There may be assumptions and material parameters used in these simulations that are not valid. The numerical study of laminated glass panes presented in Section 7.2 points out and addresses some of the challenges of laminated glass modelling in IMPETUS, but a complete numerical model should include a more complex material model in the rubber and PVB. The glass should material model which includes a random distribution of micro cracks. The model created in this thesis may be limited to the type of glass panes used in the experiments with the same dimensions.

Chapter 8

Conclusion

During the work of this thesis, a number of experiments have been conducted to increase the understanding of the behaviour of monolithic and laminated glass subjected to quasi-static loading and blast loads. Afterwards, numerical models were created in IMPETUS Afea to simulate the experiments conducted. This section aims to present conclusions based on experiences and knowledge gathered during the work.

Four-point bending

From the results found in the four-point bending tests, it is clear that the stochastic material properties in glass affect the fracture strengths of the laminated glass component. A Weibull analysis was conducted on the results of the component tests, but glass material properties could not explicitly be defined. The influence of and interaction with the PVB impeded the use of Euler-Bernoulli beam theory for fracture strength calculations. The edge treatment of the glass is concluded to be of importance as it may explain the higher calculated fracture strength in the larger specimens than the small.

Blast experiments

No definite blast capacity was found for the float glass panes tested. Only one pane stayed intact during the experiment, and this pane was loaded with a higher pressure than panes that fractured. The boundary conditions were found to affect the results as the majority of the glass panes fractured in the same area at the lower edge. The frame used in the experiments may have caused the clamping of the glass panes to be uneven. The measured velocity of the glass fragments in combination with the fragment sizes shows the risk presented by regular float glass panes subjected to blast loading. Fragment velocities varying from 12.7m/s to 23.4m/s were calculated.

The laminated glass panes were able to withstand higher loading pressures without fracturing. The laminated glass panes that fractured, all fractured close to the middle of the pane. The PVB dominates the response in the composite post fracture and prevents glass fragments from accelerating freely. The fragments were several orders of magnitude smaller than the float glass fragments. The delamination of the glass contributes to energy absorbing properties, and the PVB did not fracture in any of the experiments. There were not conducted a sufficient amount of experiments to conclude on a critical loading pressure due to the spread in fracture pressures from pane to pane. One pane did not fracture at a peak reflected pressure of 2.014 bar while a different pane fractured at 1.673 bar. The variation in capacity is expected when working with glass, due to stochastic material properties.

Numerical modelling

The numerical simulations of the four-point bending experiments yielded good results in the form of force-displacement curves. The features in IMPETUS were able to describe the response both with and without a fracture criteria. The parameter studies showed a sensitivity to element size, total running time, and PVB Young's modulus. Oscillations were noted in the simulation due to the time scaling.

The PVB tensile test simulations were conducted to calibrate a material model for the PVB based on experimental results found in the literature. PVB was found to be a highly strain rate sensitive material with an initial stiffness varying with several orders of magnitude. The initial stiffness was increasing with the increase in strain rate. Bergström-Boyce material model was found to be the best material model available in IMPETUS, but due to a modification of the implemented model compared to the original, the model was not able to describe the material response at high strain rates. The running time required by the Bergström-Boyce material model impedes efficient research when used in more complex models. Blast load simulations run with the Bergström-Boyce material model in the PVB was too complex for IMPETUS and the simulations did not start running.

The node splitting technique implemented in IMPETUS in combination with the pentahedron element type showed great results in the float glass simulations. The simulation showed a similar crack propagation as seen in the images from the experiments. The model was also able to simulate the chosen experiment both in the elastic domain and after fracture. The crack propagation in the glass proved to be highly mesh sensitive in both element size and element type. The fragment velocity in the simulation was measured to 25.36 m/s. Due to fracture along the edges on the majority of the panes, the model was not tested with other loading pressures nor compared to other experiments than FG-01

The laminated glass simulations yielded qualitative results matching the experiments, while the quantitative data in the form of a displacement curve did not match. The crack propagation in the simulations resembled the propagation seen in the experiments when both the PVB and glass were modelled with pentahedron elements. The node splitting technique enabled fracture. The merging between PVB and glass and the cohesive failure criteria enabled the delamination of the glass, and thus the deformation of the PVB. Elastic material properties in the PVB were found to be insufficient to describe the deformation in the experiments, more complex material models are needed.

Concluding remarks

Laminated glass windows have been found to increase the blast resistance of windows. The reduction in fragment size and velocity reduce the risks of fatalities and injuries during a blast. The numerical tool IMPETUS has been used to model the blast with good qualitative results with the use of node splitting and pentahedron elements. Additional research is need to enable simulations of laminated glass panes subjected to blast load, due to several challenging aspects.

Chapter 9

Further work

Numerical modelling of laminated glass windows has been proven challenging in the work of this thesis. Especially is the understanding of the PVB and glass interaction hard to model correctly. A model may enable simulation of a chosen experiment, but will not necessarily be able to simulate a similar experiment with different loading parameters. This is due to the numerous factors that affect the strength of the material. In this section, some further work is suggested based on the experiences and knowledge gathered during the work on this thesis. The numerical problems are limited to IMPETUS Afea Solver, which is the tool utilised in the work

Experimental work

- Further studies of the strength and influence of the PVB-layer in laminated glass panes subjected to blast loading should be conducted. Both the PVB material strength, but also the adhesive strength between the glass and PVB should be given attention.

- Quasi-static test of laminated glass specimens using water pressure may give better understanding around the boundary conditions and how they affect the capacity.

- Quasi static experiments should be conducted on float glass in a manner that removes the uncertainties imposed by the edges. As discussed, the authors suspect the reason for the discrepancy between the fracture strengths in the different specimen sizes and the expected fracture strengths is due to the edges. A ring on ring test may provide better results.

Numerical work

- A thorough study to find a suitable material model for PVB. Further studies on the *MAT_BERGSTROM_BOYCE-model in IMPETUS may be an option if the model is updated with the additional elastic spring.

- The delamination phenomenon between glass and PVB is still challenging to simulate. The
  *MERGE_FAILURE_COHESIVE feature in IMPETUS gave good results, but further research is needed to calibrate the feature correctly.
- Numerical studies on randomly distributed micro-cracks in glass should be given attention. The *INITIAL_DAMAGE_SURFACE_RANDOM feature in IMPETUS did not provide good results, and needs further calibration. The flaw map method presented by Yankelevsky in his paper [12] should be studied further and should be implemented in IMPETUS.
- Simulations utilising discrete particles to simulate the blast load should be conducted and compared to loading with the Friedlander equation.

Bibliography

[1] N. 2012, “Rapport fra 22. juli-kommisjonen. report from terrorist attacks 22nd july 2011 i oslo, norway,” *www.regjeringen.no*, 2012.

[2] X. Zhang and H. Hao, “The response of glass window systems to blast loadings: An overview,” *International Journal of Protective Structures*, pp. 15–23, 2016.

[3] P. Hooper, B. Blackman, and J. Dear, “The mechanical behaviour of poly(vinyl butyral) at different strain magnitudes and strain rates,” *Journal of Materials Science*, vol. 47, no. 8, pp. 3564–3576, 2012.

[4] P. D. Linz, P. Hooper, H. Arora, D. Smith, L. Pascoe, D. Cormie, B. Blackman, and J. Dear, “Reaction forces of laminated glass windows subject to blast loads,” *Composite Structures*, vol. 131, pp. 193–206, 2015.

[5] T. L. Anderson, *Fracture Mechanics Fundamentals and Applications*. Taylor & Francis, 2005.

[6] M. Larcher, G. Solomos, F. Casadei, and N. Gebbeken, “Experimental and numerical investigations of laminated glass subjected to blast loading,” *International Journal of Impact Engineering*, vol. 39, no. 1, pp. 42–50, 2012.

[7] J. Wei and L. Dharani, “Fracture mechanics of laminated glass subjected to blast loading,” *Theoretical and Applied Fracture Mechanics*, vol. 44, no. 2, pp. 157–167, 2005.

[8] J. Wei and L. Dharani, “Response of laminated architectural glazing subjected to blast loading,” *International Journal of Impact Engineering*, vol. 32, no. 12, p. 20322047, 2006.

[9] G. M, P. B, and B. WC, “An improved mechanical material model for ballistic soda-lime glass,” *Journal of Materials Engineering and Performance*, vol. 18, p. 10121028, 2009.

[10] T. Holquist, G. Johnson, C. Lopatin, D. Grady, and E. Hertel, “High strain rate properties and constitutive modeling of glass,” *Proceedings of 15th international symposium on ballistics*, 1995.

[11] K. Brekken and P. Ingier, “Modelling of window glasses exposed to blast loading,” *Master thesis written at Norwegian University of Science and Technology (NTNU)*, 2016.

[12] D. Z. Yankelevsky, “Strength prediction of annealed glass plates a new model,” *Engineering Structures*, vol. 79, pp. 244–255, 2014.

[13] A. Duser, J. A., and B. S.J., “Analysis of glass/polyvinyl butyral laminates subjected to uniform pressure,” *Journal of Engineering Mechanics*, vol. 125, p. 435442, 1999.

[14] M. Williams, R. Landel, and J. Ferry, “The temperature dependence of relaxation mechanisms in amorphous polymers and other glass-forming liquids,” *Journal of the American Chemical Society*, vol. 77, p. 37013707, 1955.

[15] H. Hidallana-Gamage, D. Thambiratnam, and N. Perera, “Numerical modelling and analysis of the blast performance of laminated glass panels and the influence of material parameters,” *Engineering Failure Analysis*, vol. 45, pp. 65–84, 2014.

[16] M. Timmel, S. Kolling, P. Osterrieder, and P. D. Bois, “A finite element model for impact simulation with laminated glass,” *International Journal of Impact Engineering*, vol. 34, p. 14651478, 2007.

[17] S. D., A. F., O. A., K. H., and H. H, “Modelling of the failure behavior of windscreens and component tests,” *LS-DYNA Anwenderforum*, 2005.

[18] E. Dural, “Experimental and numerical treatment of delamination in laminated glass plate structures,” *Journal of Reinforced Plastics and Composites*, vol. 35, no. 1, pp. 56–70, 2016.

[19] P. D. Linz, P. A. Hooper, H. Arora, Y. Wang, D. Smith, B. R. Blackman, and J. P. Dear, “Delamination properties of laminated glass windows subject to blast loading,” *International Journal of Impact Engineering*, 2016.

[20] Z. Xihong, H. Hong, and M. Guowei, “Laboratory test and numerical simulation of laminated glass window vulnerability to debris impact,” *International Journal of Impact Engineering*, vol. 55, p. 4962, 2013.

[21] L. Olovsson, J. Limido, J.-L. Lacome, A. G. Hanssen, and J. Petit, “Modeling fragmentation with new high order finite element technology and node splitting,” *European Physical Journal Web of Conferences*, vol. 94, 2015.

[22] A. Ilseng, “Mechanical behavior of laminated glass exposed to blast loading,” *Master thesis written at Norwegian University of Science and Technology (NTNU)*, 2013.

[23] R. Hibbler, *Mechanics of Materials*. CENGAGE Learning, 2013.

[24] J. Pelfrene, J. Kuntsche, S. V. Dam, W. V. Paepegem, and J. Schneider, “Critical assessment of the post-breakage performance of blast loaded laminated glazing: Experiments and simulations,” *International Journal of Impact Engineering*, vol. 88, pp. 61–71, 2016.

[25] H. Norville, King, W. Kim, L. Jason, and Norville, “Behaviour and strength of laminated glass,” *Journal of Engineering Mechanics*, vol. 124, no. 1, pp. 46–53, 2015.

[26] F. Irgens, “Formelsamling; mekanikk,” *Formulas in solid mechanincs*, 2010.

[27] V. Aune, T. Borvik, and M. Langseth, *Impact Mechanics: An Introduction to Blast Mechanics*. Lecture Notes in TKT4128 at NTNU, 2016.

[28] V. Aune, E. Fagerholt, M. Langseth, and T. Borvik, “A shock tube facility to generate blast loading on structures,” *International Journal of Protective Structures*, vol. 7, no. 3, pp. 340–366, 2016.

[29] C. Inglis, “Stresses in a plate due to the presence of cracks and sharp corners.,” *Transactions of the Institute of Naval Architects*, no. 55, pp. 219–241, 1913.

[30] A. Griffith, “The phenomena of rupture and flow in solids,” *Philosophical Transactions*, vol. A, no. 221, pp. 163–198, 1920.

[31] G. Irwin, “Onset of fast fracture propagation in high strength steel and aluminum alloys,” *Sagamore Research Conference Proceedings*, no. 2, pp. 289–305, 1956.

[32] ASTM International, “Standard test methods for determination of fracture toughness of advanced ceramics at ambient temperature,” *ASTM International*, 2016.

[33] J. B. Watchman, *Mechanical Properties of Ceramics*. Wiley, 2009.

[34] F. Zok, “On weakest link theory and weibull statistics,” *Journal of the Americal Ceramic Society*, vol. 100, p. 12651268, 2017.

[35] W. Weibull, *A statistical theory of the strength of materials*. Ingenirsvetenskapsakademiens handlingar, 1939.

[36] E. Fagerholt, “Digital image correlation,” *Lecture note SIMLab*, 2016.

[37] D. N. McCormick and D. J. Lord, “Digtal image correlation,” *materialstoday*, vol. 13, no. 12, pp. 52–54, 2010.

[38] R. Walpole, R. Myers, S. Myers, and K. Ye, *Probability and Statistics for Engineers and Scientists*. Pearson Education, 2012.

[39] K. Mathisen, “Non linear finite element analysis,” *Lecture Notes in TKT4197 at NTNU*, 2016.

[40] Cook, Malkus, Plesha, and Witt, *Concepts and Applications of Finite Element Analysis*. John Wiley and sons INC., 2002.

[41] "What is gpu-accelerated computing?." `http://www.nvidia.com/object/what-is-gpu-computing.html`. Accessed: 2017-03-08.

[42] "User guide and commands, impetus afea solver, version 3.0 beta." `http://manual.impetus-afea.com/pdf/solver/v3.0b/manual.pdf`. Accessed: 2017-03-22.

[43] X. Zhang, H. Hao, and G. Ma, "Dynamic material model of annealed soda-lime glass," *International Journal of Impact Engineering*, vol. 77, pp. 108–119, 2015.

[44] P. Linz, W. Y., H. P. A., H. Arora, S. D., L. Pascoe, C. D., B. B. R. K., and D. J. P., "Determining material response for polyvinyl butyral (pvb) in blast loading situations," *Experimental mechanics*, vol. 56, p. 15011517, 2016.

[45] A. Froli and L. Lani, "Adhesion, creep and relaxation properties of pvb in laminated safety glass," *Glass performance days, Tampere (Finland)*, 2011.

[46] U. Keller and H. Mortelmans, "Adhesion in laminated safety glass - what makes it work?," *Glass Processing Days, 13-16 '99*, 1999.

[47] L. Treloar, *The Physics of Rubber Elasticity*. OUP Oxford, 1975.

[48] C. M. Roland, "Mechanical behaviour of rubber at high strain rates," *Rubber Chemistry and Technology*, vol. 79, no. 3, pp. 429–459, 2006.

[49] C. Salisbury, "On the deformation mechanics of hyperelastic porous materials," *Doctor Dissertation University of Waterloo*, 2011.

[50] J. Bergström, *Mechanics of Solid Polymers*. Plastic Design Library, 2015.

[51] L. Olovsson, "Blast loaded laminated window glass," *IMPETUS presentation*, 2017.

[52] ASTM International, "Standard test method for flexural strength of advanced ceramics at ambient temperature," *ASTM International*, 2013.

[53] P. Hooper, R. Sukhram, and J. D. B.R.K Blackman, "On the blast resistance of laminated glass," *International Journal of Solids and Structures*, vol. 49, no. 6, pp. 899–918, 2012.

[54] J. Menk, *Strength and Fracture of Glass and Ceramics*. Glass Science and Technology, 1992.

[55] ASTM international, "Standard practice for reporting uniaxial strength data and estimating weibull distribution parameters for advanced ceramics," *ASTM International*, pp. 1–18, 2013.

[56] C. Fors, "Mechanical properties of interlayers in laminated glass: Experimental and numerical evaluation," *Master thesis written at Lund University*, 2014.

[57] "Metals and alloys - densities." `http://www.engineeringtoolbox.com/metal-alloys-densities-d_50.html`. Accessed: 2017-06-03.

[58] I. O. for Standardization (ISO), "Rubber, vulcanized or thermoplastic - determination of tensile stress-strain properties," *International Standard*, vol. 1, 2011.

[59] D. Tabor, "The bulk modulus of rubber," *Polymer*, vol. 35, no. 13, pp. 2759–2763, 1994.

Appendix A

Four point bending samples

Figure A.1: Small four point bending test samples ($100 \times 20mm$)

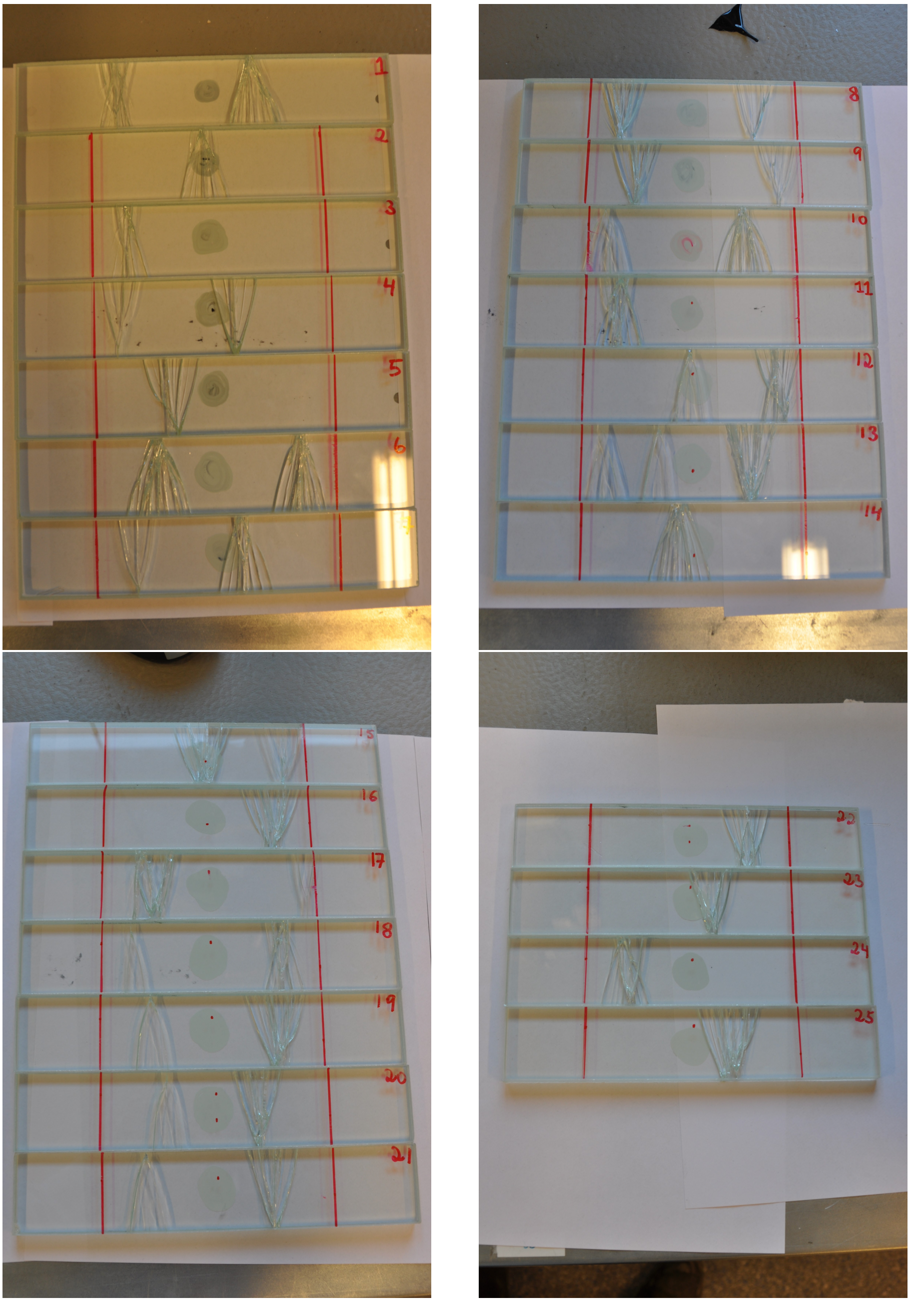

Figure A.2: Medium four point bending test samples ($200 \times 40mm$)

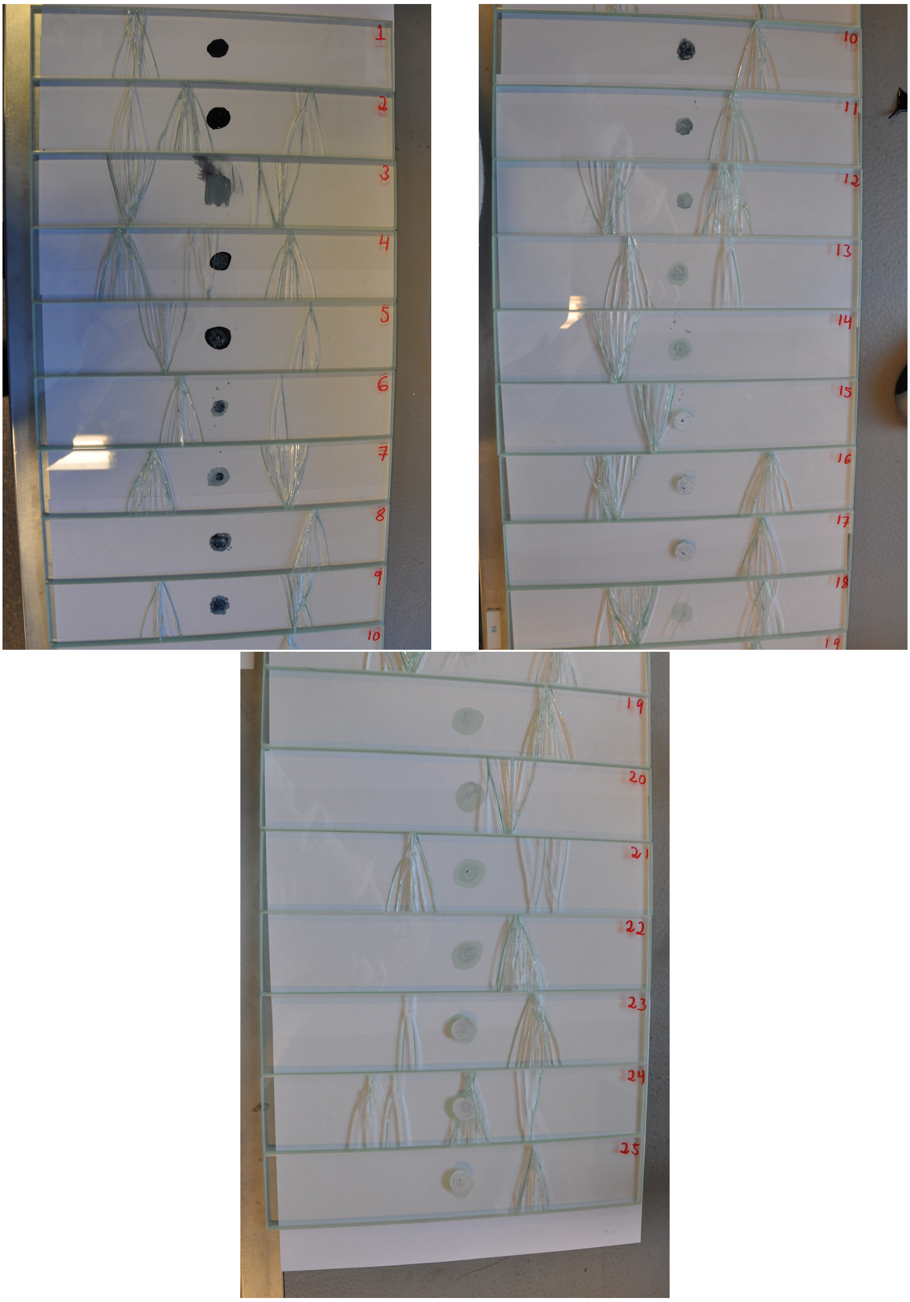

Figure A.3: Large four point bending test samples ($300 \times 60mm$)

Table A.1: Measured dimensions of the small samples. The height was averaged based on three measurements spread over the length of the specimens

Test	Width $[mm]$	Height $[mm]$	Test	Width $[mm]$	Height $[mm]$
1	19.67	9.130	14	19.70	9.110
2	19.60	9.178	15	19.63	9.116
3	19.64	9.115	16	19.92	9.101
4	19.66	9.105	17	19.70	9.182
5	19.63	9.103	18	19.96	9.146
6	19.62	9.098	19	19.66	9.110
7	19.63	9.180	20	19.62	9.172
8	19.63	9.137	21	19.61	9.126
9	19.68	9.172	22	19.90	9.152
10	19.62	9.183	23	19.95	9.157
11	19.68	9.180	24	19.63	9.146
12	19.61	9.099	25	19.64	9.106
13	19.91	9.180			

Table A.2: Measured dimensions of the medium samples. The height was averaged based on three measurements spread over the length of the specimens

Test	Width $[mm]$	Height $[mm]$	Test	Width $[mm]$	Height $[mm]$
1	39.67	9.176	14	39.53	9.146
2	39.55	9.172	15	39.62	9.137
3	39.52	9.070	16	39.52	9.165
4	39.54	9.160	17	39.51	9.098
5	39.56	9.168	18	39.44	9.111
6	39.55	9.126	19	39.61	9.139
7	39.46	9.077	20	39.51	9.157
8	39.67	9.137	21	39.50	9.154
9	39.40	9.098	22	39.44	9.094
10	39.56	9.058	23	39.53	9.139
11	39.39	9.086	24	39.45	9.106
12	39.48	9.097	25	39.47	9.089
13	39.53	9.153			

Table A.3: Measured dimensions of the large samples. The height was averaged based on three measurements spread over the length of the specimens

Test	Width $[mm]$	Height $[mm]$	Test	Width $[mm]$	Height $[mm]$
1	59.42	9.093	14	59.55	9.157
2	59.44	9.131	15	59.54	9.160
3	59.41	9.144	16	59.61	9.155
4	59.48	9.130	17	59.46	9.102
5	59.54	9.095	18	59.65	9.170
6	59.63	9.159	19	59.41	9.133
7	59.50	9.087	20	59.48	9.073
8	59.46	9.150	21	59.54	9.167
9	59.46	9.117	22	59.51	9.099
10	59.66	9.135	23	59.62	9.153
11	59.14	9.162	24	59.44	9.172
12	59.53	9.087	25	59.51	9.167
13	59.63	9.087			

Appendix B

Weibull analyses

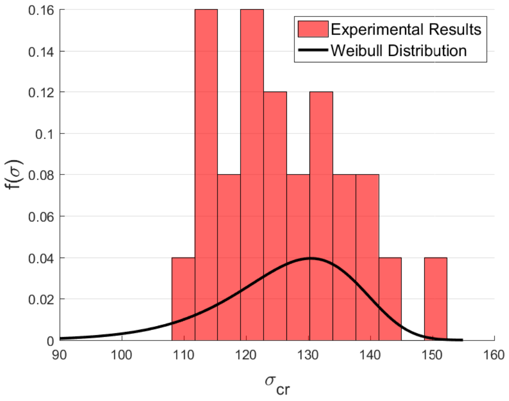

(a) Weibull distribution

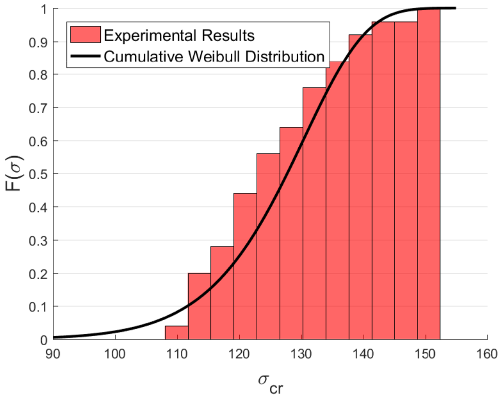

(b) Cumulative Weibull distribution

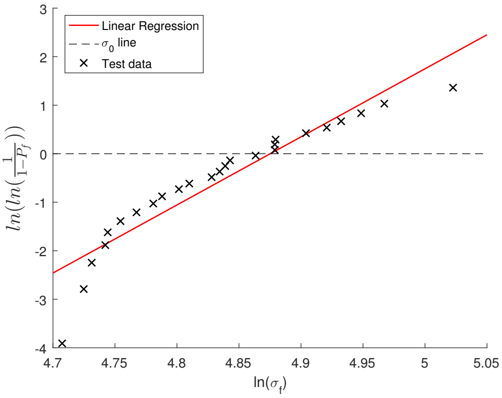

(c) Weibull analysis

Figure B.1: Results from the Weibull analyses conducted on the small samples

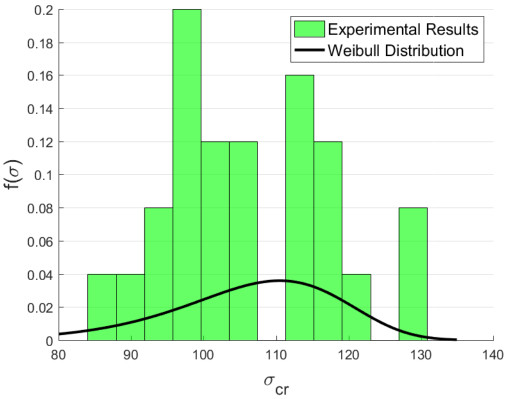

(a) Weibull distribution

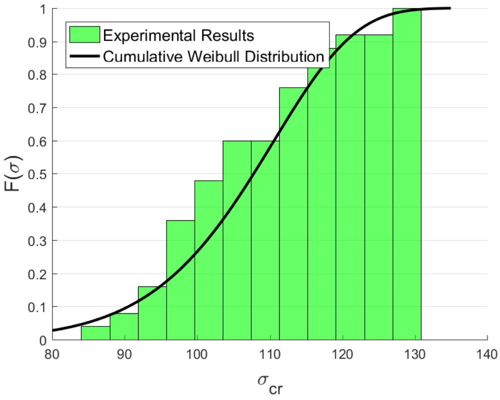

(b) Cumulative Weibull distribution

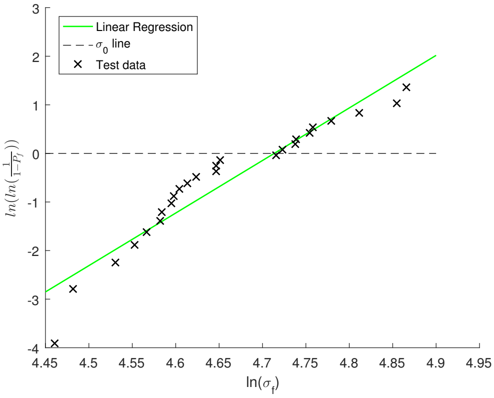

(c) Weibull analysis

Figure B.2: Results from the Weibull analyses conducted on the medium samples

Appendix C

Blast tests summary

Table C.1: Summary of blast tests

Test	Pane	Bolt torque [Nm]	Pf [bar]	Pr [bar]	Δ [mm]	Failure[1]
FG-01	01	150	1.526	0.636	3.594	Middle
FG-02	02	150	1.563	0.660	5.519	Edge
FG-03	03	150	1.285	0.516	5.132	Edge
FG-04	04	100	1.599	0.655	5.676	Edge
FG-05-1	05	100	1.569	0.625	5.446	**X**
FG-05-2	05	100	2.057	0.734	5.966	Edge
FG-06	06	100	1.322	0.530	4.644	Edge
LG-01-1	01	150	6.317	1.697	3.695	**X**
LG-01-2	01	150	7.669	2.014	4.793	**X**
LG-01-3	01	150	8.142	No data	No data	No data
LG-02	02	100	6.258	1.673	3.307	Middle
LG-03-1	03	100	6.345	1.613	3.666	**X**
LG-03-2	03	100	7.593	1.989	4.541	**X**
LG-03-3	03	100	9.101	2.188	4.985	Middle
LG-04	04	100	8.628	2.079	2.993	Middle

---

[1] **X** indicates ”No fracture”

Appendix D

Crack propagation

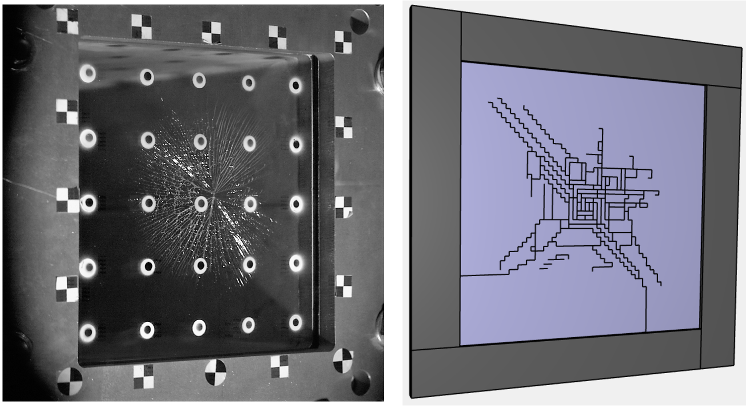

(a) t=0.0ms **(b)** t=0.0ms

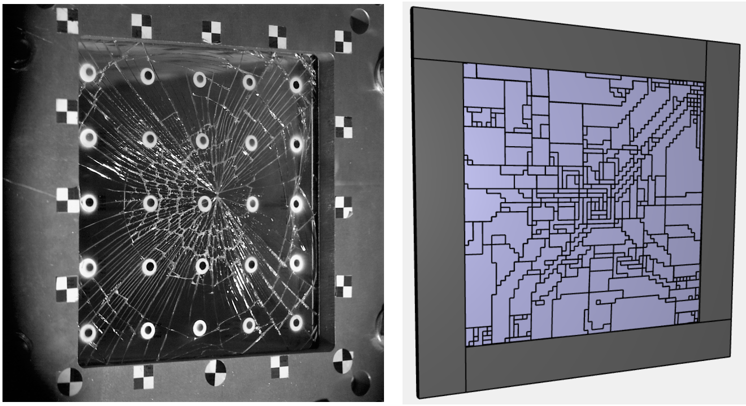

(c) t=0.52ms **(d)** t=0.52ms

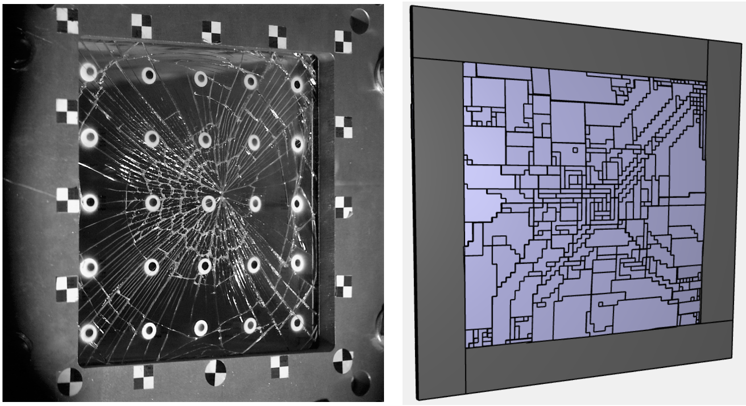

(e) t=1.04ms **(f)** t=1.04ms

Figure D.1: Crack propagation comparison between experiment and hexahedron elements with size $5 \times 5\text{mm}$

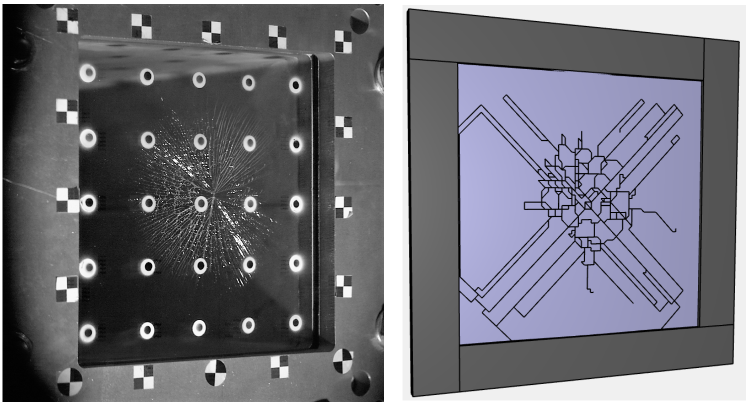

(a) t=0.0ms **(b)** t=0.0ms

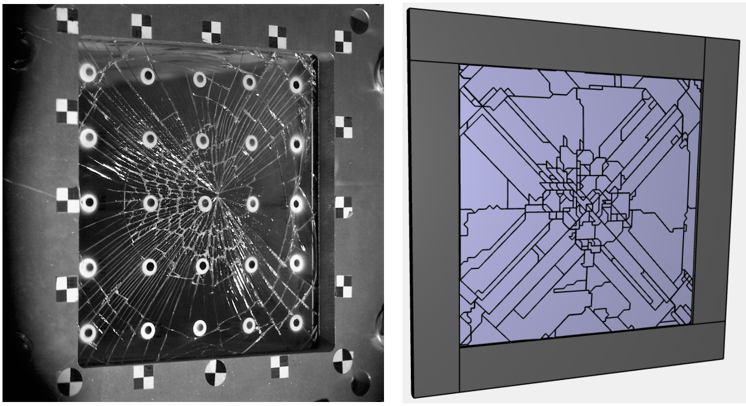

(c) t=0.58ms **(d)** t=0.58ms

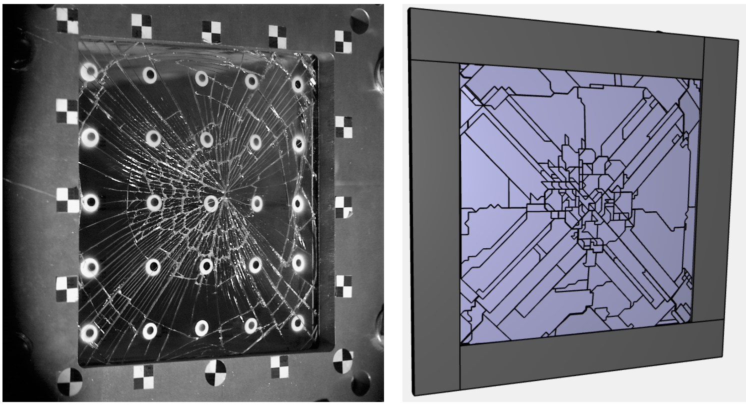

(e) t=1.136ms **(f)** t=1.36ms

Figure D.2: Crack propagation comparison between experiment and pentahedron elements with size 4×4mm

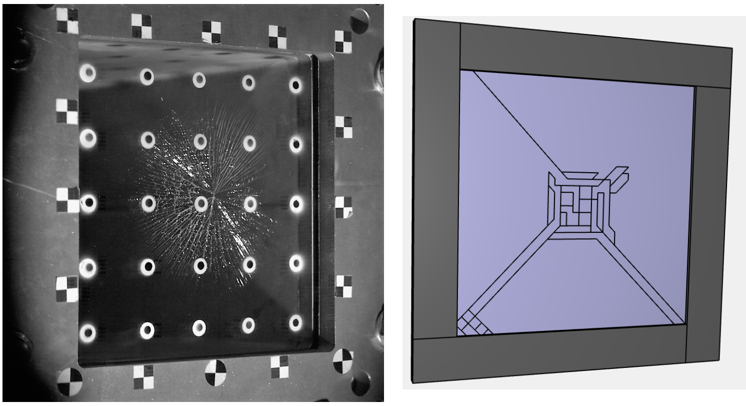

(a) t=0.0ms

(b) t=0.0ms

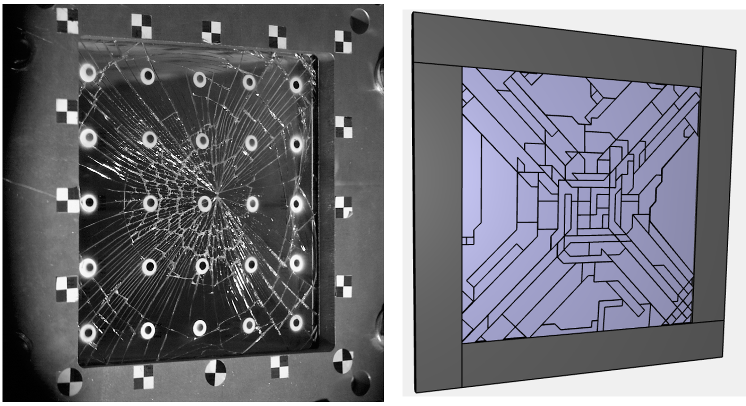

(c) t=0.52ms

(d) t=0.52ms

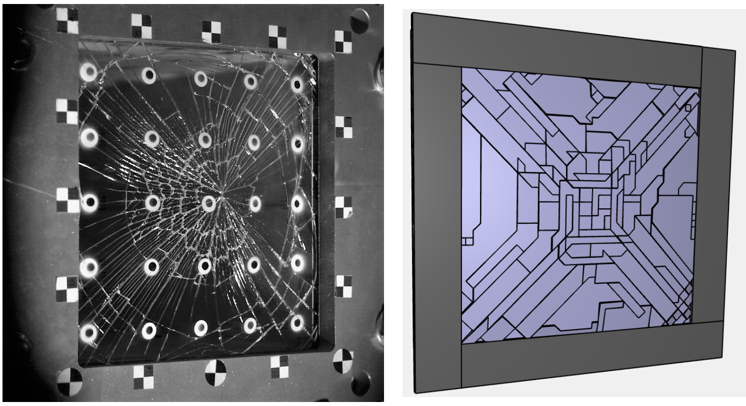

(e) t=1.105ms

(f) t=1.105ms

Figure D.3: Crack propagation comparison between experiment and pentahedron elements with size 8×8mm

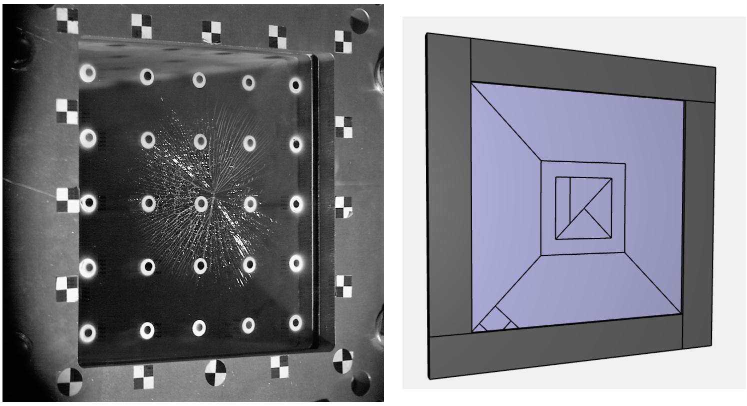

(a) t=0.0ms

(b) t=0.0ms

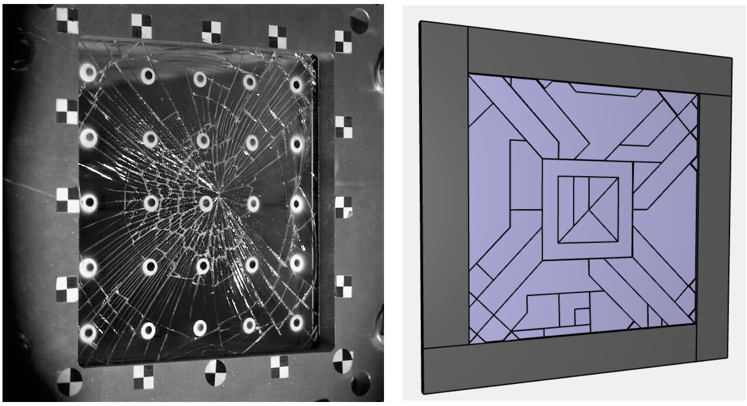

(c) t=0.69ms

(d) t=0.69ms

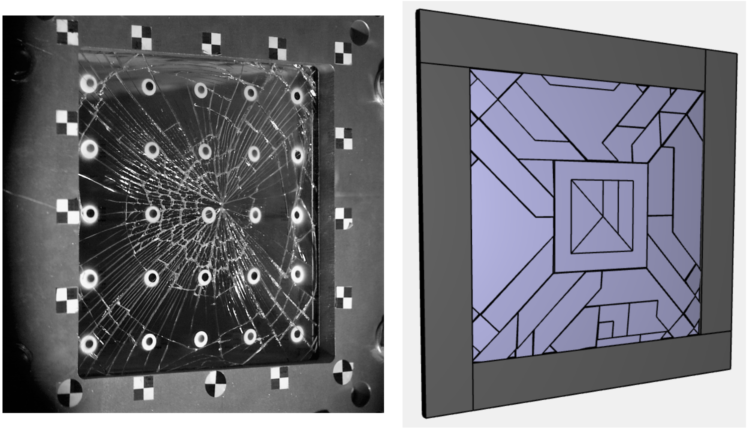

(e) t=1.104ms

(f) t=1.104ms

Figure D.4: Crack propagation comparison between experiment and pentahedron elements with size 20×20mm where t=0.0 is set to first fracture

Appendix E

IMPETUS script - Laminated glass blast simulation

```
#------------------------------------------------------------------------
# BLAST LOADED 400 x 400 LAMINATED GLASS PLATE - LG-03-3
#------------------------------------------------------------------------
*UNIT_SYSTEM
MMTONS
#-----------------------------------------------------------
*PARAMETER
#-----------------------------------------------------------
Pr         = 0.21876;
td         = 24.000E-3;
b          = 1.6923;
#-----------------------------------------------------------
sig_max    = 47.47;
Kic        = 23.72;
#------------------------------------------------------------
th         = 3.80;
th_r       = 4;
th_pvb     = 1.52;
#------------------------------------------------------------
el_g_x     = 5;
el_g_y     = 35;
el_g_z     = 1;
#-----------------------------------------------------------
tol        = 0.0000001;
tend       = 0.01;
num_imp    = 100;
num_ascii  = 1000;
```

```
#-----------------------------------------------------------------
*TIME
[%tend]
#-----------------------------------------------------------------
# GLASS COMPONENTS
#-----------------------------------------------------------------
*INCLUDE
mesh_4x4mm.k
1, 1, 1
0, 0, 0, 0, 0, -1.89999998
*INCLUDE
mesh_4x4mm.k
1, 1, 1, 1000000, 1000000, 1
0, 0, 0, 0, 0, -1.89999998-%th_pvb-3.8-%tol
*CHANGE_P-ORDER
P, 1, 3
P, 2, 3
*MERGE
P,3,P,1,[2*%tol],1212
P,3,P,2,[2*%tol],1212
*MERGE_FAILURE_COHESIVE
1212,10,10,1,1,0,1
#-----------------------------------------------------------------
# PVB COMPONENT
#-----------------------------------------------------------------
*INCLUDE
mesh_4x4mm.k
1, 1, 0.4, 2000000, 2000000, 2
0, 0, 0, 0, 0,-3.8-[%th_pvb]/2-%tol
*CHANGE_P-ORDER
P, 3, 3
#-----------------------------------------------------------------
# RUBBER FRONT SIDE
#-----------------------------------------------------------------
*COMPONENT_BOX
90, 4, [%el_g_x], [%el_g_y], [%el_g_z]
-200, 200, [%tol], -150, -150, [%th_r+%tol]
*COMPONENT_BOX
91, 5, [%el_g_y], [%el_g_x], [%el_g_z]
-150, 200, [%tol], 200, 150, [%th_r+%tol]
*COMPONENT_BOX
92, 6, [%el_g_x], [%el_g_y], [%el_g_z]
150, 150, [%tol], 200, -200, [%th_r+%tol]
*COMPONENT_BOX
93, 7, [%el_g_y], [%el_g_x], [%el_g_z]
```

```
-200, -200, [%tol], 150, -150, [%th_r+%tol]
*MERGE_DUPLICATED_NODES
P, 4, P, 5, [%tol*2]
*MERGE_DUPLICATED_NODES
P, 5, P, 6, [%tol*2]
*MERGE_DUPLICATED_NODES
P, 6, P, 7, [%tol*2]
*MERGE_DUPLICATED_NODES
P, 7, P, 4, [%tol*2]
*SET_PART
"Rubber 1"
4567
4, 5, 6, 7
*MERGE
PS,4567,P,1,[2*%tol]
#----------------------------------------------------------------
# RUBBER BACK SIDE
#----------------------------------------------------------------
*COMPONENT_BOX
94, 8, [%el_g_x], [%el_g_y], [%el_g_z]
-200,200,[-%th-%th-%th_pvb-%tol-%tol],-150,-150,
[-%th-%tol-%th_r-%th-%th_pvb-%tol]
*COMPONENT_BOX
95, 9, [%el_g_y], [%el_g_x], [%el_g_z]
-150,200,[-%th-%tol-%th-%th_pvb-%tol],200,150,
[-%th-%tol-%th_r-%th-%th_pvb-%tol]
*COMPONENT_BOX
96, 10, [%el_g_x], [%el_g_y], [%el_g_z]
150,150,[-%th-%tol-%th-%th_pvb-%tol],200,-200,
[-%th-%tol-%th_r-%th-%th_pvb-%tol]
*COMPONENT_BOX
97, 11, [%el_g_y], [%el_g_x], [%el_g_z]
-200,-200,[-%th-%tol-%th-%th_pvb-%tol],150,-150,
[-%th-%tol-%th_r-%th-%th_pvb-%tol]
*MERGE_DUPLICATED_NODES
P, 8, P, 9, [%tol*2]
*MERGE_DUPLICATED_NODES
P, 9, P, 10, [%tol*2]
*MERGE_DUPLICATED_NODES
P, 10, P, 11, [%tol*2]
*MERGE_DUPLICATED_NODES
P, 11, P, 8, [%tol*2]
*SET_PART
"Rubber 2"
891011
```

```
8, 9, 10, 11
*MERGE
PS,891011,P,2,[2*%tol]
#----------------------------------------------------------
# GEOMETRIES: BCs & LOAD SURFACE
#-----------------------------------------------------------
*GEOMETRY_SEED_COORDINATE
”Backside rubber”
10
-175, -175, [-%th-%th_r-%th_pvb-%th-%tol-%tol]
*GEOMETRY_SEED_COORDINATE
”Impactside rubber”
11
-175, -175, [%th_r]
*GEOMETRY_SEED_COORDINATE
”Glass front side”
12
0, 0, 0
#-----------------------------------------------------------
# LOAD
#-----------------------------------------------------------
*LOAD_PRESSURE
G, 12, 111, 1, 0, [%td]
*FUNCTION
”Friedlander Curve [MPa]”
111
([%Pr])*exp((-%b*t)/%td)*(1-(t/%td))
#-----------------------------------------------------------
# PARTS
#-----------------------------------------------------------
*PART
”Glass plate 1”
1, 1
”Glass plate 2”
2, 1
”PVB”
3, 3
”Rubber - pt1”
4, 2
”Rubber - pt2”
5, 2
”Rubber - pt3”
6, 2
”Rubber - pt4”
7, 2
```

```
”Rubber - pt5”
8, 2
”Rubber - pt6”
9, 2
”Rubber - pt7”
10, 2
”Rubber - pt8”
11, 2
#------------------------------------------------------------
# DEFINE CONTACT
#------------------------------------------------------------
*CONTACT
”General contact”
696969
ALL, 0, ALL, 0, 1.9
#------------------------------------------------------
# MATERIALS
#------------------------------------------------------
*MAT_ELASTIC
”Glass”
1, 2500E-12, 70E3, 0.23,99
*MAT_ELASTIC
”Rubber”
2, 1400E-12, 150, 0.46
*MAT_ELASTIC
”PVB”
3, 1100E-12, 50, 0.45
#------------------------------------------------------
*PROP_DAMAGE_BRITTLE
99, 3
[%sig_max], [%Kic]
#------------------------------------------------------
# BOUNDARY CONDITIONS
#------------------------------------------------------
*BC_MOTION
”Motion”
100
G, 10, XYZ
*BC_MOTION
”Motion”
101
G, 11, XYZ
#------------------------------------------------------
# OUTPUT FROM MIDPOINT
#------------------------------------------------------
```

```
*OUTPUT_SENSOR
"Sensor M1"
1009, 1, 0, 0, -[%th]
#---------------------------------------------------------
# GENERAL OUTPUT
#---------------------------------------------------------
*OUTPUT
[%tend/%num_imp], [%tend/%num_ascii]
*END
```